2018

APPLICATION OF SEISMIC RADIAL ANISOTROPY FOR NEAR-SURFACE FRACTURES IDENTIFICATION

Jer-Yu Jeng
Michigan Technological University, jjeng@mtu.edu

APPLICATION OF SEISMIC RADIAL ANISOTROPY FOR NEAR-SURFACE FRACTURES IDENTIFICATION

By

Jer-Yu Jeng

A THESIS

Submitted in partial fulfillment of the requirements for the degree of

MASTER OF SCIENCE

In Geophysics

MICHIGAN TECHNOLOGICAL UNIVERSITY

2018

This thesis has been approved in partial fulfillment of the requirements for the Degree of MASTER OF SCIENCE in Geophysics.

Department of Geological and Mining Engineering and Sciences

Thesis Co-Advisor:	*Dr. Roohollah Askari*
Thesis Co-Advisor:	*Dr. Snehamoy Chatterjee*
Committee Member:	*Dr. Wayne D. Pennington*
Department Chair:	*Dr. John S. Gierke.*

Table of Contents

List of figures

List of tables

Abstract

Fractures significantly control the groundwater flow and solute transport in geological settings of low-permeable rocks. Fractures also affect seismic wave propagation. For instance, they can create a directional dependence of seismic velocity with respect to their orientations, known as seismic anisotropy. Seismic radial anisotropy as used here is the difference between the velocity of a vertically polarized S-wave (S_V) and one polarized horizontally (S_H). In this thesis, seismic radial anisotropy was used to evaluate its usefulness for correlating with near-surface fractures. The seismic radial anisotropy models were obtained at two sites from dispersion analyses of the Rayleigh waves, with vertical polarization, and Love waves, with horizontal polarization, using the Multichannel Analysis of Surface Waves (MASW) method. The seismic radial anisotropies at these two sites in different geological settings (one metamorphic-igneous bedrock and the other sedimentary), shows a strong correlation of seismic radial anisotropy with near surface fractures, and hence, can be used to characterize near-surface fractures.

1 Introduction

Understanding fluid flow in geologic environments has been an important topic in hydrology and environmental geology. Fluid flow studies for the understanding of subsurface hydrology have been applied to natural systems for the purposes of improving public well-being and optimal design of infrastructures. Fractures or fractured rocks have a huge impact on fluid flow and solute transport. Subsurface fracture networks affect the hydraulic properties like hydraulic conductivity, especially in low permeable crystalline rocks (Adler and Thovert 1999, Faybishenko et al. 2000, Haneberg et al. 1999, Wood and Norrell 1996, Heath 1983). Identifying subsurface fracture system are critical when modeling fluid flow, solute transport, and site selection for groundwater pumping wells in aquifers (Castaing et al. 2002, Elmo and Stead 2010, Merrien-Soukatchoff et al. 2012). In the petroleum industry, subsurface fracture systems are the most efficient avenue for hydrocarbon migration (Aydin 2000). Studies also show that by characterizing natural fracture system, the hydraulic-fracturing process can be optimized (Gale et al. 2007). In the past few decades, with the increasing interest in more complex and unconventional reservoirs, fracture characterization has drawn a significant attention in the oil and gas industry (Laubach et al. 2000). Overall, identifying subsurface fracture is an important topic and can be beneficial in hydrology, environmental geology, and the petroleum industry.

Due to the complexities of natural fracture systems, fracture characterization is a challenging task. There are several geophysical methods widely used for subsurface

fracture characterization, such as ground penetrating radar (GPR) (Olsson et al. 1992, Dorn et al. 2012), very low frequency (VLF) (Ganerød et al. 2006, Reynolds 2011, Paterson and Ronka 1971) and seismic methods, including refraction and reflection seismic methods, Vertical seismic profile (VSP) (Reynolds 2011, Ganerød et al. 2006, Lynn et al. 1995) and well-log data (Hornby et al. 2003).

Olsson et al. (1992) and Dorn et al. (2012) used Ground-Penetrating Radar (GPR) to identify fractures. Compared to other geophysical methods, GPR provides higher resolution and has higher reliability. GPR has the advantage to map potential permeable fractures and fracture zones away from boreholes, even with widths in the range of millimeters (Dorn et al. 2012, Olsson et al. 1992). However, the pitfall of the GPR method is the limited depth of investigation. Usually, the depth of penetration is up to around 50 feet (ft) (15.24 meter (m)), but it can be just a few centimeters in some materials with high conductivity (Daniels 2004). Due to this limitation, GPR is not practical if a fractured bedrock is located in the deeper subsurface.

Very Low Frequency (VLF) electromagnetic surveying is a rapid and cheap tool to detect water-bearing fractures by mapping electric conductivity (Ganerød et al. 2006, Reynolds 2011, Olsson et al. 1992). The limitation of VLF is its dependency on the coverage of the distant transmitter in the survey area. The transmitter is often one that is used for military communications; therefore, it has its geographical limitation. In addition, VLF can only identify fractures zones but provide no further detailed information.

Seismic methods have also been used to study fractures. The seismic wave velocity in fracture zones can be directional. In other words, seismic wave velocity might vary depending on the orientations of the fractures. Seismic anisotropy is used to describe this direction dependence of the seismic wave velocity (Thomsen 1986). Seismic P-wave anisotropy has been used to characterize fractures in oil and gas reservoirs via some methodologies such as Amplitude-Variation with Offset and Azimuth (AVOA) (Hall and Kendall 2003), Velocity Versus Azimuth (VVAZ) (Crampin et al. 1980) and well-log data (Hornby et al. 2003); these methods take advantage of the difference in velocity depending on the direction of the P-wave propagation. There are also studies of S-wave anisotropy based on the polarization of the S-wave in an anisotropic medium where S-wave splits into two polarized shear waves (Vecsey et al. 2008, Aki and Richards 1980), and studies that make use of the variation of the S-wave velocity with azimuth (Azimuthal anisotropy) (Gupta et al. 2016, Li 1997, DeVault et al. 2002, Mueller 1991, Lynn and Thomsen 1990, Martin and Davis 1987).

Some studies assume an isotropic subsurface model is a simplified approximation; however, in many geological settings, rocks exhibit anisotropy. From generalized Hooke's law, in isotropic media, the stiffness matrix has two independent elements, but for anisotropic media, it has twenty-one independent elements. Transverse isotropy (TI) assumes symmetry condition to the anisotropic material, and hence the independent components of the stiffness matrix reduce to five. For many anisotropic media, transverse isotropy (TI) is a simplified way for general applications. There are three types of transverse isotropy, Vertical Transverse Isotropy (VTI), Horizontal Transverse Isotropy

(HTI) and Tilted Transverse Isotropy (TTI). VTI models are used to describe anisotropy in horizontal layers, such as shale or fractures parallel to the surface. Most of the hydrocarbon reservoirs showed VTI characteristics. HTI models are associated with those fractures that are vertical due to the dominance of regional stress. TTI models are usually applied to the dipped formation.

VTI is commonly observed in sedimentary basins; it can describe the vertical and lateral velocity variations, and it is widely used in many geophysical applications (Thomsen 1986, Xie and Liu 2015, Tsvankin and Grechka 2006, Gei et al. 2011). In groundwater flow modeling, shallow fracture zones usually provide great lateral continuity (Singhal and Gupta 2010). Those fractures, which are often parallel to the bedding planes, have shown to exert a strong influence on groundwater flow studies at both local and regional scales. In general, the parallel fractures provide a better pathway for flow compared to the fractures perpendicular to the bedding planes (Singhal and Gupta 2010, Swanson et al. 2006, Swanson 2007, Michalski and Britton 1997). Therefore, the VTI model seems to be suitable to study near-surface fractures for hydrological studies.

Due to the suitability of VTI for the study of surface fractures, the difference between the vertically polarized S-wave velocity (V_{SV}) and the horizontally polarized S-wave velocity (V_{SH}) is used in this thesis Surface waves are chosen for the approach used here. Rayleigh wave velocity is mainly affected by the velocity of S_V waves (V_{SV}), whereas Love wave velocity is mainly affected by the velocity of S_H waves (V_{SH}). Seismic radial anisotropy can be quantified by the radial anisotropy parameter ξ

$$\xi = (V_{SH} - V_{SV}) / V_S \qquad (1)$$

Where V_s is the isotropic component and can be represented by the Voigt average (Dziewonski and Anderson 1981, Tomar et al. 2017) :

$$V_s = \sqrt{(2V_{SV}^2 + V_{SH}^2)/3} \qquad (2)$$

Seismic radial anisotropy has long been a research topic in the crust and upper mantle (Anderson 1961, Ekström and Dziewonski 1998, Nakanishi and Anderson 1983, Schlue and Knopoff 1977). For the near surface application, Safani et al. (2005) identified the radial anisotropy below the near surface. Dal Moro and Ferigo (2011) showed that shear-wave anisotropy for shallow layers could be detected. Tomar et al. (2017) obtained a significant negative radial anisotropy in the shallow zone caused by vertical cracks. Gao et al. (2017) used radial anisotropy to detected groundwater flow. Overall, seismic radial anisotropy has drawn more attention in the near-surface application. Therefore, the aim of this research is to show that seismic radial anisotropy can be one of the promising attributes to identify subsurface fractures.

2 Geology

In this research, a total of six seismic lines were processed and interpreted, collected from two different sites near five different wells. One of the sites is located at Forestry Service East (FSE) well field near Mirror Lake, New Hampshire, in which two seismic lines close to two logged wells are acquired. The other site is located the in Hannahville Indian Community, Michigan, which included four seismic lines near three different logged wells.

2.1 Mirror Lake, New Hampshire

Unconsolidated glacial deposits cover the surface of the Mirror Lake, New Hampshire, area, that typically ranging from 0 to 15 m thick, but in some areas are up to 50 m thick (Johnson and Dunstan 1998, Ellefsen et al. 2002). The bedrock near the FSE well field is pelitic schist of sillimanite-grade metamorphism (Lyons et al. 1997) which was assigned to lower and upper parts of the Rangeley Formation, from the Silurian period (423-428 Ma) (Ellefsen et al. 2002, Johnson and Dunstan 1998). Granitoids, pegmatites, and diabase later intruded it. The Concord Granite was intruded in the Late Devonian (370-365 Ma) (Armstrong and Boudette 1984) and included fingers and dikes, which are both parallel and crosscut the foliation of the schist. The bedrock and these granite intrusions were subsequently intruded by pegmatite in the Late Devonian (Ellefsen et al. 2002). During the Middle Jurassic through Early Cretaceous age (190-95 Ma), pegmatites and aplites intruded into the metasedimentary rock and granitoids (Olson 1942, McHone 1984, Ellefsen et al. 2002). Based on observations in the wells nearby, fracture apertures

vary from 0.005 mm to 26.6 mm, but 90 percent of the apertures is less than 3 mm. Fracture length ranges from 1.0 m to 24 m. From the well-log report of the 15 index boreholes in this study field, 73 percent of the fractures were found in granitoids and 23 percent in schist (Johnson and Dunstan 1998).

2.2 Hannahville Indian Community, Michigan

The Hannahville Indian community is mostly located in Menominee County, Michigan, approximately 13 miles west of Escanaba, Michigan. The near surface geology is mainly composed of five aquifer units in sedimentary units. The surface layer is Quaternary glacial deposits that are mainly fine-grained including mixtures of clay, silt, sand, and gravel. According to Vanlier (1963), the thickness of the glacial deposit is around 0 - 200 ft (0 - 60.96 m). Underneath the glacier deposit is Middle Ordovician Upper limestone bedrock unit that is composed of Trenton and Black River Limestone formation. This formation consists of limestone, dolomite, and shale, its thickness is usually around 0 - 300 ft (0 - 91.44 m). The next layer that is Middle limestones and sandstones aquifer unit belong to early Ordovician Prairie du Chien group containing limestone, dolomite, sandstone, along with sandy and shaley dolomite. The Prairie du Chien group is an important water-bearing unit in this area. Beneath this formation, the next group is defined as Lower sandstone aquifer, which is mainly Cambrian Franconia Sandstone and Dresbach Sandstone. This layer, which is also water-bearing, contains pink, gray and white sandstones whose thickness is around 50 - 200 ft (15.24 - 60.96 m). The base is Precambrian rocks, consisting of varieties of crystalline, metamorphic and sedimentary

rocks like granite, schist, marble and iron formation; this Precambrian Rock aquifer group is mainly contained dark gray-green schist. Based on the geophysical logs, Bayless et al. (2013) classified the lithostratigraphic of the sub-glacial sedimentary units based on the physical and mineral properties into four units including shale and carbonate rock unit, upper carbonate rock unit, carbonate rock and glauconitic sandstone unit, and lower carbonate rock unit. The fractures identified by Bayless et al. (2013) are mostly located in the upper 50 ft (15.24 m) of the carbonate rock and glauconitic sandstone unit, which is around 160 - 300 ft (48.77 - 91.44 m) below the surface in this area. There is no preferred dipping direction of the fractures, most of them are less than 20 degrees. Only a few of high angle fractures (dips more than 60 degrees) are identified in that report.

3 Multichannel Analysis of Surface Waves

Understanding the elastic properties of subsurface materials is important to engineering and environmental studies. The shear modulus or rigidity of the near surface is a crucial parameter, which can be calculated from the S-wave velocity and density. Multichannel Analysis of Surface Waves (MASW) is a widely used in the near-surface studies to estimate V_{SV} and V_{SH} from the Rayleigh and Love waves, respectively (Xia et al. 2012, Xia et al. 1999). MASW has a lower frequency range and usually targets shallower subsurface compared to the other conventional seismic techniques (Park et al. 2007). The standard MASW method usually includes three steps: (1) field data acquisition; (2) estimation of dispersion curve from either phase or group velocity image; (3) dispersion curve inversion to obtain the 1D or 2D V_S velocity profile.

In the standard MASW, the source type can be either active source or passive; and the data acquisition usually includes a 24-channel seismic recorder with low-frequency (e.g. 4.5 Hz are always recommended) receivers (geophones) aligned on the surface (Figure 1). The source is positioned on either side of the array.

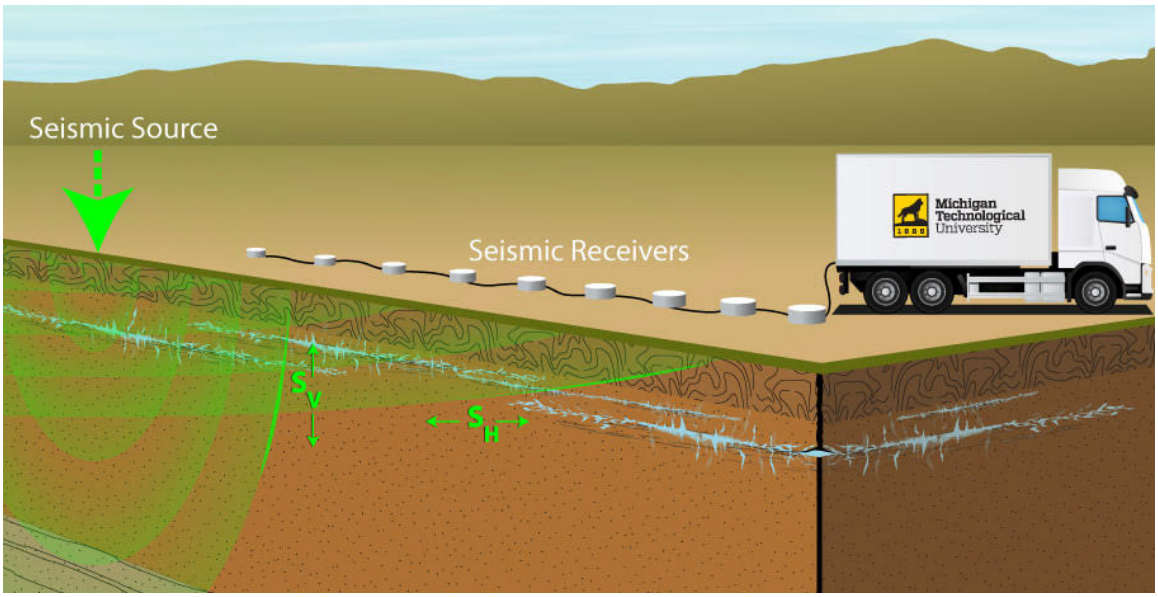

Figure 1. A scheme of conventional MASW data acquisition. Here, as the S_H wave oscillates parallel to the fracture network, S_H wave is faster, and hence ahead of the S_V wave.

In the next step, the dispersion curve can be obtained from either phase or group velocity images. This step is most critical in the MASW survey, and many methods have been developed to obtain the phase and group velocities. For the group velocity, some methods include multiple filter analysis (MFA) (Herrmann 1973), wavelet transform (Holschneider et al. 2005, Kulesh et al. 2005), modified S-transform and slant stacking (Askari and Hejazi 2015), and sparse S-transform (Dolatabadi et al. 2017, Dokht Dolatabadi Esfahani et al. 2018). For the phase velocity, Fourier phase spectrum analysis (Sato 1955), frequency-wavenumber (f-k) transform (Yilmaz 1987), tau-p transform (McMechan and Yedlin 1981), phase-shift (Park et al. 1998), High-resolution Linear Radon Transform (HRLRT) (Luo et al. 2008), and generalized S-transform (Askari and Ferguson 2012).

In areas such as the ones used in this study (Mirror Lake and Hannaville), where there is a high S-wave velocity contrast between the subsoil and bedrock, it can be challenging to obtain the accurate dispersion curve at low frequencies due to a sudden change of the phase velocity (Casto et al. 2010, Casto et al. 2009, Khaheshi Banab and Motazedian 2010). In the rest of this section, the general approach used in the present study will be described with brief justifications; later sections will provide more details.

First, the phase shift method (Park et al. 1998) was applied for the phase velocity dispersion curve imaging, which transforms the data into frequency-velocity (*f*-*v*) domain; however, no distinguishable dispersion curves at the low frequency was observed (Figure 2a & 2c). The HRLRT (Luo et al. 2008) was also implemented (Figure 2b & 2d). From all the datasets in this study, it was observed that HRLRT yields more distinguishable dispersion curves compared to the phase shift method (Figure 2), and therefore HRLRT method was used for this study for dispersion curve estimation. With the data transformed into the *f*-*v* domain, different modes of dispersion curve can be picked from phase velocity image with the higher values indicated.

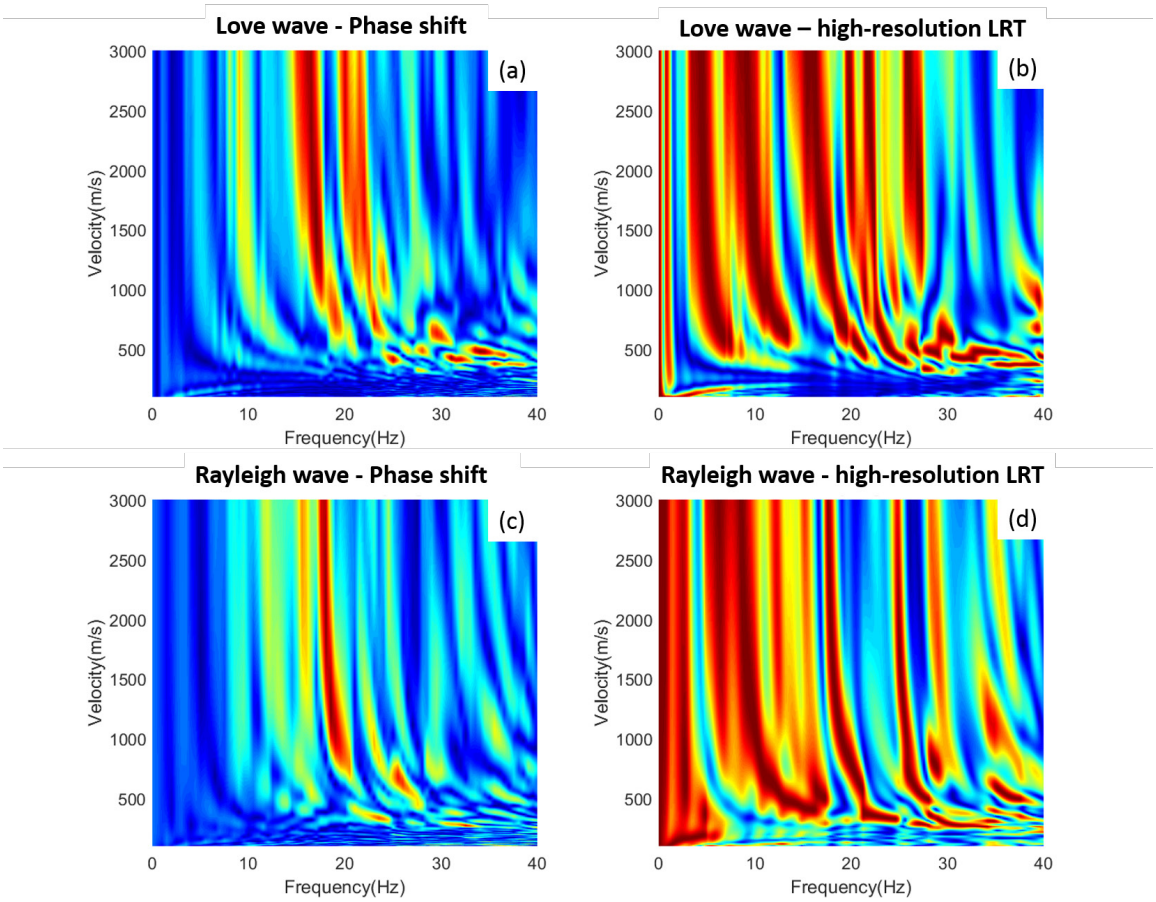

Figure 2. Comparison of phase shift and HRLRT method for phase velocity imaging from Line 3 dataset with both Love wave and Rayleigh wave. (a) Love wave with phase shift method. (b) Love wave with high-resolution LRT method. (c) Rayleigh wave with phase shift method. (d) Rayleigh wave with high-resolution LRT method. Warm colors represent higher values. From both Love and Rayleigh wave dataset, high-resolution LRT have more information on low frequency (<10Hz).

After obtaining the dispersion curves from either phase or group velocity image, which in this thesis phase velocity is used, the final step of data inversion was performed to obtain an S-wave velocity model. In the inversion, an S-wave velocity model was obtained

which gives phase or group velocities that minimize the difference between phase or group velocities predicted from the model, and the observed phase or group velocities from step 2 (data processing). There are several inversion approaches including the linearized (Nolet 1981, Tarantola 1987) and direct search methods (Sen and Stoffa 1991, Lomax and Snieder 1994, Wathelet 2008). Linearized inversion usually gives acceptable results if the initial velocity model, which is updated through the inversion, is close to the real subsurface velocity model. In other words, the optimality of the final results highly depends on the initial velocity model (Goldberg et al. 1989). On the other hand, the direct search method provides acceptable non-unique multiple solutions which converge towards the global minimum. In this research, an open software package called Dinver, from geopsy.org, was used to apply inversion in this study (Wathelet 2008). The software is based on the enhanced neighborhood algorithm, which is one of the direct search methods and could provide an efficient search and ensure the solution converged towards a global solution.

3.1 High-resolution Linear Radon Transform

The high-resolution Linear Radon Transform is based on the standard Linear Radon Transform (LRT) (Yilmaz 1987) and Least-Square Linear Radon Transform (Yilmaz and Taner 1994).

The standard Linear Radon Transform is a plane-wave decomposition obtained by summation over amplitudes from a data to which linear-moved-out has applied. The standard Linear Radon Transform is expressed by

$$\boldsymbol{d} = \boldsymbol{Lm} \qquad (3)$$

$$\boldsymbol{m_{adj}} = \boldsymbol{L^T d} \quad (4)$$

where $\boldsymbol{L} = e^{i\pi f 2px}$ is the forward LRT operator, $\boldsymbol{d}$ is the shot gather, $\boldsymbol{m}$ represent the Radon panel and $\boldsymbol{m_{adj}}$ indicate a low-resolution Radon panel using the transpose or adjoint operator $\boldsymbol{L^T}$. The standard LRT method usually suffer from loss of resolution (Trad et al. 2003). Least-Square LRT is improved by adding an objective function (Equation 5) to minimize the error found in the least-square solution (Equation 6) and is stabilized with a damping parameter λ (Equation 7) (Yilmaz and Taner 1994).

$$J = \|\boldsymbol{d} - \boldsymbol{Lm}\|^2 \qquad (5)$$

$$\boldsymbol{m} = (\boldsymbol{L^T L})^{-1}\boldsymbol{L^T d} \qquad (6)$$

$$\boldsymbol{m} = (\boldsymbol{L^T L} + \lambda \boldsymbol{I})^{-1}\boldsymbol{L^T d} \qquad (7)$$

Least-Square LRT can separate signal and noise better since it provides better reconstruction and resolution in the Radon domain (Schonewille and Duijndam 2001). The pitfall of least-square LRT is an increase in the amplitude of aliased events in the Radon domain, which degrades signal periodicity and causes some problems such as body-wave suppression (Marfurt et al. 1996). To address this pitfall, the high-resolution Linear Radon Transform (Luo et al. 2008) incorporates a weighted preconditioned conjugate gradient (CG) to perform high-resolution Linear Radon Transform (equation 8) and the objective function (equation 9) is minimized with respect to equation (10) (Trad et al. 2002),

$$\boldsymbol{d} = \boldsymbol{L}\boldsymbol{W}_{\boldsymbol{m}}^{-\mathbf{1}}\boldsymbol{W}_{\boldsymbol{m}}\boldsymbol{m} \qquad (8)$$

$$J = \left\|\boldsymbol{W}_{\boldsymbol{d}}(\boldsymbol{d} - \boldsymbol{L}\boldsymbol{W}_{\boldsymbol{m}}^{-\mathbf{1}}\boldsymbol{W}_{\boldsymbol{m}}\boldsymbol{m})\right\|^2 + \lambda\|\boldsymbol{W}_{\boldsymbol{m}}\boldsymbol{m}\|^2 \qquad (9)$$

$$\left(\boldsymbol{W}_{\boldsymbol{m}}^{-\mathbf{1}}\boldsymbol{L}^{\boldsymbol{T}}\boldsymbol{W}_{\boldsymbol{d}}^{\boldsymbol{T}}\boldsymbol{W}_{\boldsymbol{d}}\boldsymbol{L}\boldsymbol{W}_{\boldsymbol{m}}^{-\mathbf{1}} + \lambda\boldsymbol{I}\right)\boldsymbol{W}_{\boldsymbol{m}}\boldsymbol{m} = \boldsymbol{W}_{\boldsymbol{m}}^{-\mathbf{1}}\boldsymbol{L}^{\boldsymbol{T}}\boldsymbol{W}_{\boldsymbol{d}}^{\boldsymbol{T}}\boldsymbol{W}_{\boldsymbol{d}}\boldsymbol{d} \qquad (10)$$

where $\boldsymbol{I}$ is an identity matrix, $\boldsymbol{W}_{\boldsymbol{d}}$ is the data weight, and $\boldsymbol{W}_{\boldsymbol{m}}$ is the weighting factor matrix. The solution is obtained by using $\boldsymbol{W}_{\boldsymbol{d}}$ and $\boldsymbol{W}_{\boldsymbol{m}}$ of *i*-th iteration of the CG algorithm. By including the weighting matrix into the calculation, the data constraint is relaxed for noisy data. The HRLRT significantly increases the resolution of dispersion curves at the low frequencies and provides more distinguishable trends of different modes (Xia et al. 2003, Luo et al. 2007).

3.2 Enhanced Neighborhood Algorithm

The Rayleigh and Love wave inversions are performed in order to obtain for the shear wave velocity profiles from dispersion curves identified in the images that had been obtained using HRLRT. The inversion method is based on the Neighborhood algorithm. Neighborhood algorithm is a stochastic direct-search method, similar to Genetic Algorithms (GA) (Lomax and Snieder 1994, Nagai et al. 2005) and Simulated Annealing (SA) (Sen and Stoffa 1991, Ryden and Park 2006, Beaty et al. 2002), to solve a multidimensional parameter space problems with acceptable models fitting in the constraint. In the original Neighborhood algorithm, parameters are scaled to 0 to 1 at the beginning of the inversion but in Enhanced Neighborhood algorithm, a dynamic scaling is proposed by Wathelet (2008), where the parameters are scaled along the corresponding

axis, by defining the area along the active region. For the surface wave inversion, the main parameters are the P-wave and S-wave velocity, density, and thickness of layers. First, the Neighborhood Algorithm generates $\boldsymbol{n_{s0}}$ random samples (similar to standard Markov Chain Monte-Carlo method) in the parameter space and then computes dispersion curves for all these models. A range for all the chosen parameters is defined from all the $\boldsymbol{n_{s0}}$ random models generated in the beginning. The algorithm compares the computed dispersion curves with the observed one (obtained in step 2) via a misfit function (equation 11) (Wathelet et al. 2004),

$$\boldsymbol{misfit} = \sqrt{\sum_{i=0}^{n_F} \frac{(x_{di}-x_{ci})^2}{\sigma_i^2 n_F}}, \qquad (11)$$

where $\boldsymbol{x_{di}}$ is the phase velocity of the picked dispersion curve and $\boldsymbol{x_{ci}}$ are the phase velocity of the calculated theoretical curve from the inversion model at the frequency $\boldsymbol{f_i}$, $\boldsymbol{n_F}$ is the number of the frequency samples considered and the $\boldsymbol{\sigma}$ is the uncertainty of the frequency samples considered. The method is iterative where the improvement in those $\boldsymbol{n_r}$ models are made by performing the uniform random walk in the Voronoi cell of the models to generate $\boldsymbol{n_s}$ new models in each iteration. This inversion processing will continue generating new models within the range of last improved models until the iteration reaches its maximum number or new models cannot minimize the objective function further. Compared to other stochastic search methods like GA and SA, the tuning parameters in the neighborhood algorithm are fewer and should achieve better results (Sambridge 1999). Compare to linearized inversion, neighborhood algorithm provides several non-unique solutions close to the true model.

4 Seismic Radial Anisotropy

Since 1960, many studies have noted seismic anisotropy in the Earth's crust and upper mantle, (Anderson 1961, Aki 1963, McEvilly 1964). The anisotropy in the mantle is caused by the orientation of olivine, the seismic velocity parallel to *a* axis of the olivine is greater than that perpendicular (Christensen and Lundquist 1982, Montagner and Anderson 1989). By analyzing the anisotropy in the upper mantle, its deformation and flow patterns can be characterized (Montagner 2007, Becker et al. 2008). Several mechanisms have been proposed to explain the anisotropy in the crust including aligned faults, layering, fractures, and crystals. Fine layering within sedimentary or magmatic rocks, or highly foliation of metamorphic rocks, can create the radial anisotropy. For example, Jaxybulatov et al. (2014) used the radial anisotropy to characterize the horizontal layering of magmatic intrusions. Godfrey et al. (2000) observed that the schist layer in the crust with appropriate orientation could yield considerable anisotropic behavior in the crust. Preferred mineral or lattice orientation in sedimentary rocks is also one of the mechanism causing seismic anisotropy (Valcke et al. 2006). In Xie et al. (2013), they believed in the shallow crust underlying Tibet there are vertical cracks or faults that cause negative anisotropy. Structural weaknesses such as aligned open fractures can also lead to radial anisotropy (Bates and Phillips 2000).

Other than crust and upper mantle studies, seismic radial anisotropy has also been used in the near-surface studies. Safani et al. (2005) found that the shear-wave velocities obtained from the Love and Rayleigh waves had different velocities at similar depths, which

indicates the anisotropic behavior in shallow sediments. Dal Moro and Ferigo (2011) observed the radial anisotropy in shallow layers. Socco et al. (2011) compared the S-wave velocities model obtained from the Scholte and Love waves and concluded possible subsurface anisotropy. Tomar et al. (2017) also performed their studies based on Scholte and Love wave and obtained subsurface shear wave velocities profiles up to 600 m. Tomar et al. (2017) noted two layers with radial anisotropy, where the shallowed layer had significant negative radial anisotropy and the deeper layer with positive radial anisotropy. For a recent application, Gao et al. (2017) used the radial anisotropy to detect groundwater flow.

Seismic radial anisotropy as used here is the difference between the vertically polarized S-wave velocity (V_{SV}) and the horizontally polarized S-wave velocity (V_{SH}). Because the Rayleigh wave is affected by the vertically polarized S_V wave and the Love wave by the horizontally polarized S_H wave, the estimated S-wave velocities from the separate dispersion analyses of the Rayleigh waves and the Love waves can be used to estimate the radial anisotropy. The radial anisotropy parameter ξ can quantify seismic radial anisotropy in equation (1) (Anderson 1961). In this research, the seismic radial anisotropy is apparently correlated with near-surface fractures.

5 Data Acquisition

Six different seismic lines were conducted from two different area (Table 1). Twenty-four 3-component 4.5 Hz geophones with Geode® recording systems recorded data from vertical and transverse components to obtain Rayleigh and Love waves (inline component data was not used). All the data was recorded for 2 s with a 0.125 ms sample rate. An active source, Betsy M3 Seisgun®, was used, barreled in a hole around 0.2 m depth and backfilled with wet soil. Studies have shown that Betsy gun is a good active source for near-surface study (Miller et al. 1994, Miller et al. 1986).

Table 1. List of detail information about each line

Name	Location	Nearest well	Geophone interval (m)	Total length (m)
Line 1	Mirror Lake, NH	FSE 8	3.5	80.5
Line 2	Mirror Lake, NH	FSE 11	3.5	80.5
Line 3	Hannahville, MI	Community 1 &2	3.5	80.5
Line 4	Hannahville, MI	Community 1 &2	4	92
Line 5	Hannahville, MI	Casino 5	3.5	80.5
Line 6	Hannahville, MI	Casino 5	4	92

At Mirror Lake, the geophone interval used was 3.5 m with a total length of 80.5m. The centers of two lines were close to wells FSE8 and FSE11 (Figure 3), enabling a comparison between our radial anisotropy results with log data.

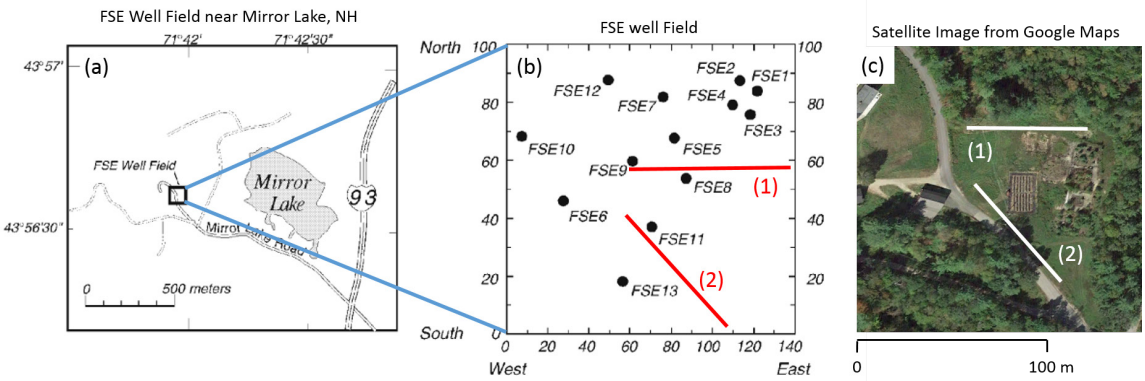

Figure 3. Research site near Mirror Lake, NH. Figure modified from Day-Lewis et al. (2006). (a) FSE well field near Mirror Lake, NH. (b) Well location from the site, we have two lines (1) and (2) in this location. (c) Satellite image from google maps.

At the Hannahville Indian Community, two lines were located near a pair of wells: community 1 (38-25 CO1) and community 2 (38-25 CO2). The geophone interval in Line 3 was 3.5 m with a total length of 80.5 m and geophone interval in Line 4 was 4 m with total length 92 m. While the target of the maximum depth of investigation in both lines was 100 m, the geophone intervals were chosen due to accommodate surface obstacles and limitations. We specifically deployed two lines in different directions in order to investigate azimuthal anisotropy (different velocities in different horizontal directions). Two additional lines were deployed near well Casino 5 (38-25 C5). In Line 5, the

geophone interval was 3.5 m with a total length of 80.5 m and Line 6 geophone interval 4 m with a total length of 92 m (Figure 4).

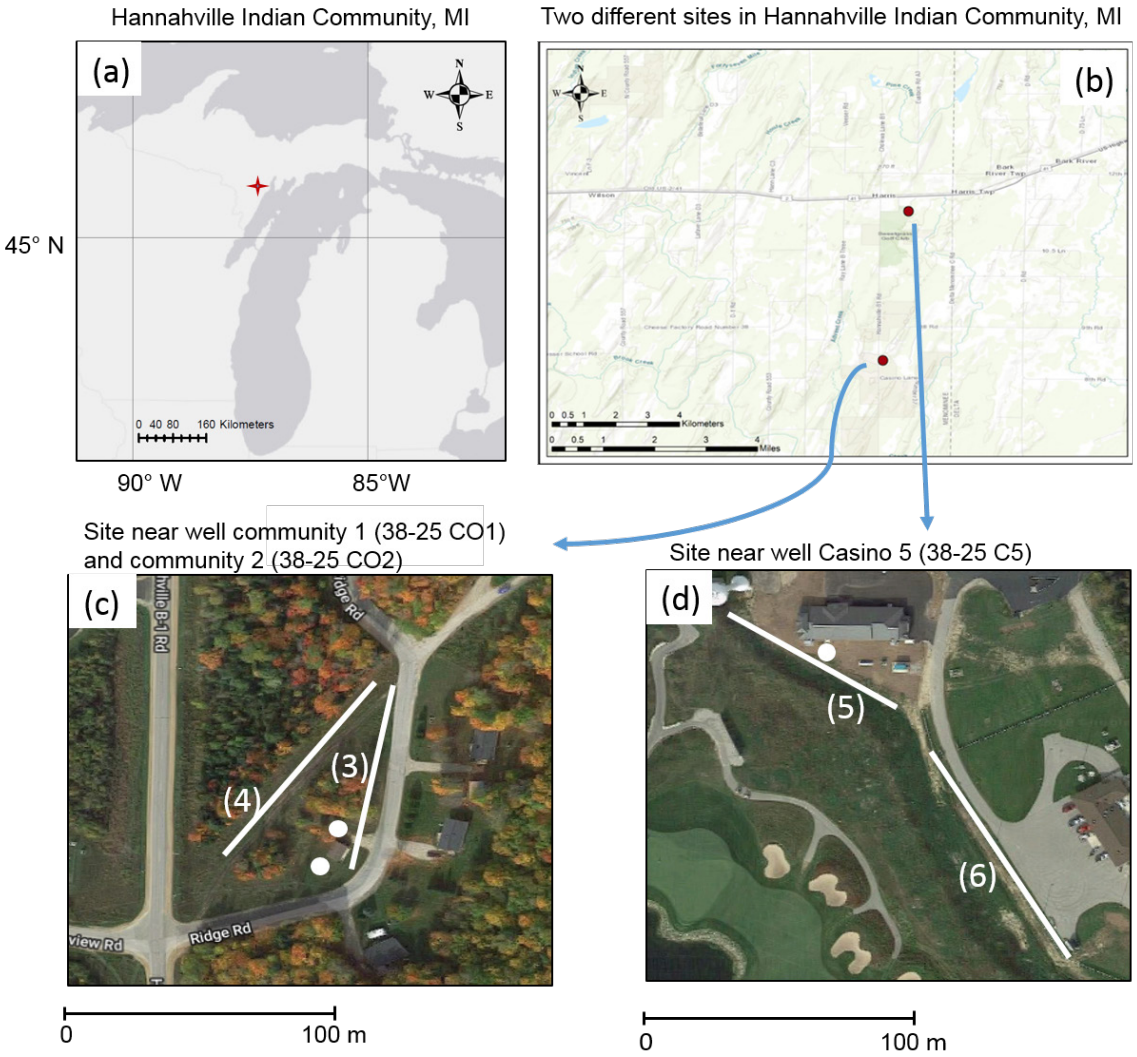

Figure 4. Research site in Hannahville Indian Community, MI. (a) Research location of Hannahville Indian Community, MI. (b) Two different sites in Hannahville Indian Community, MI, the locations are about 3.5 miles apart from each other. (c) Line 3 and

Line 4 near well community 1 and community 2 (white dots in the figure) located in 45°39'27"N, 87°20'44"W. (d) Line 5 and Line 6 near well Casino 5 (white dot in the figure) located in 45°41'58"N, 87°20'18"W.

6 Data Processing

The same general processing steps of stacking, denoising, muting, low-pass filtering, and f-k filtering were applied to both data sets. Nonetheless, estimation of dispersion curves from data obtained at the Mirror Lake site was more challenging than at the Hannahville Indian Community site, which can be explained with respect to the differences in the geologic structure at the sites. The geology of Mirror Lake, NH is more heterogeneous, and modal energy is transferred from one mode to another mode at different offsets (O'Neill and Matsuoka 2005), restricting the observation of some modes only over limited offset ranges. In order to detect a specific mode (e.g., fundamental or higher modes), windowing of the traces over a limited range of receivers in which the modal energy of that mode is available was conducted. This enabled the dispersion curves of different modes to be estimated at Mirror Lake. For the data processing, MATLAB with CREWES MATLAB Toolbox, SeisLab for MATLAB toolbox and SegyMAT MATLAB toolbox were used. In this section, a processing overview will be presented for Mirror Lake Line 1 first, followed by variations applicable to the other lines; other specific details are presented in Appendix A.

6.1 Mirror Lake, New Hampshire

6.1.1 Data Processing for Line 1

Seismic data were analyzed from the vertical component and transverse components. Rayleigh waves were assumed to be recorded on the vertical component and Love waves on the transverse component. The general processing workflow is shown in Table 2.

Table 2. General data processing workflow used in this study.

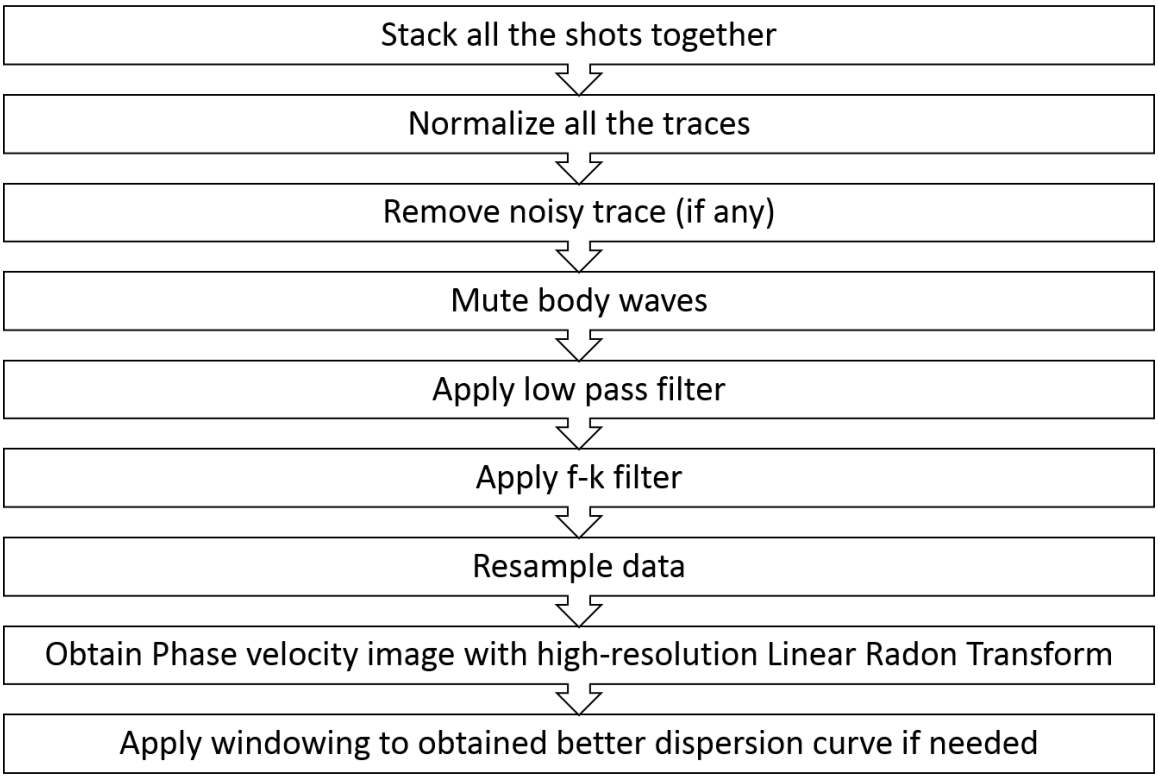

6.1.1.1 Rayleigh Wave

First, for every line of acquisition, five shots from the shotgun source were available. All the shots were stacked to improve the signal to noise ratio (Figure 5a). After stacking, the data were trace-normalized to remove the distance-dependent amplitude decay (Figure 6a). After normalization, very noisy traces were removed. Since our study is focused on the surface wave, the data were top-muted to remove the body waves. The data were also bottom-muted to remove the scattered noise arriving after the surface waves (Figure 6b). Because body waves have higher frequencies than surface waves, a low pass filter (0-80 Hz) was applied (Figure 7) to further attenuate the body waves. The f-k filters were also applied (Figure 8) (Askari and Siahkoohi 2008) for body wave removal. To save the computational time in the next step, the data were resampled from 0.125 ms sample rate to 2 ms. Then, the high-resolution Linear Radon transform was used to identify the dispersion curve (Luo et al. 2008). Dispersion curve was manually picked from the part with higher spectrum in the phase velocity image. By trial and error, the optimum iteration number was obtained to better separate the fundamental mode and higher modes. As in the Mirror Lake data the energy of fundamental mode tends to jump from one mode to higher modes, the energy of fundamental and higher modes might be dominant at some specific offsets (O'Neill and Matsuoka 2005, Askari and Hejazi 2015). Based on the observation, this phenomenon was more troublesome in the Rayleigh wave data than in the Love wave data. Hence, windowing to the Rayleigh wave datasets were applied where each window uses encompasses specific offset range. The fundamental mode of the Rayleigh wave data was observable from the 1st to 10th geophones. The first

higher mode was noticeable from the 4th to 17th geophones and the second higher mode from the 7th to 16th geophones (Figure 9).

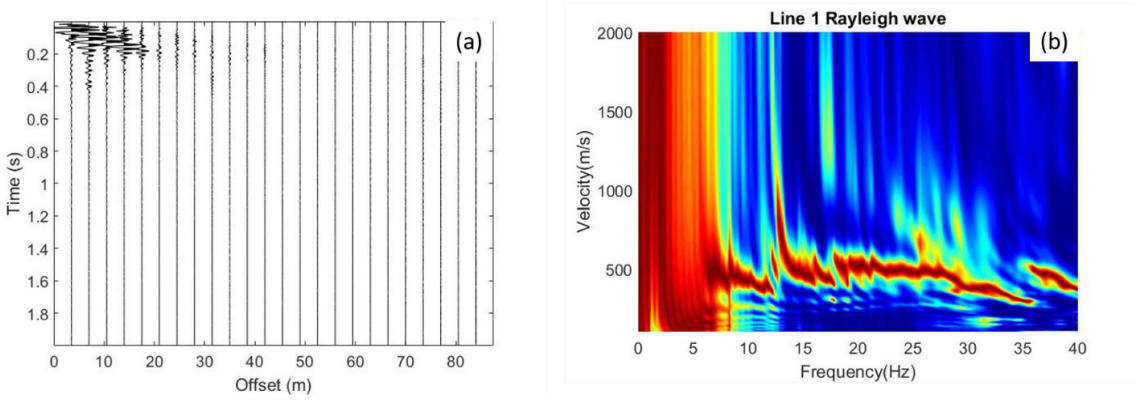

Figure 5. Line 1 Rayleigh wave analysis from Mirror Lake. (a) Seismic record of the gather after stacking vertical components from five shots; the seismic traces show that the energy decreases rapidly with time and distance. (b) Phase velocity image before additional processing; in this figure, it is difficult to assign dispersion curves because the modes overlap.

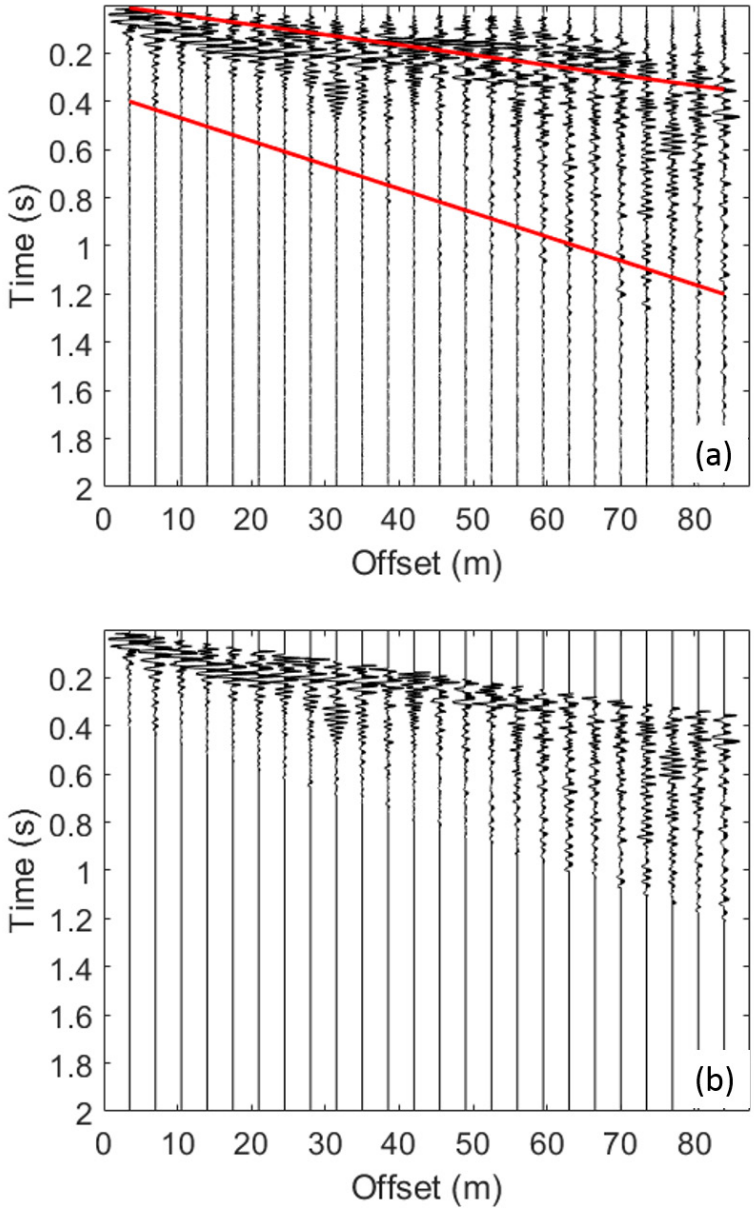

Figure 6. (a) Line 1 Rayleigh wave normalized seismic trace with top and down muting to preserve the surface wave only. The seismic data was preserved within two red lines. The body waves were muted from the top and the noise from the bottom is also muted. (b) Line 1 Rayleigh wave data after applied muting.

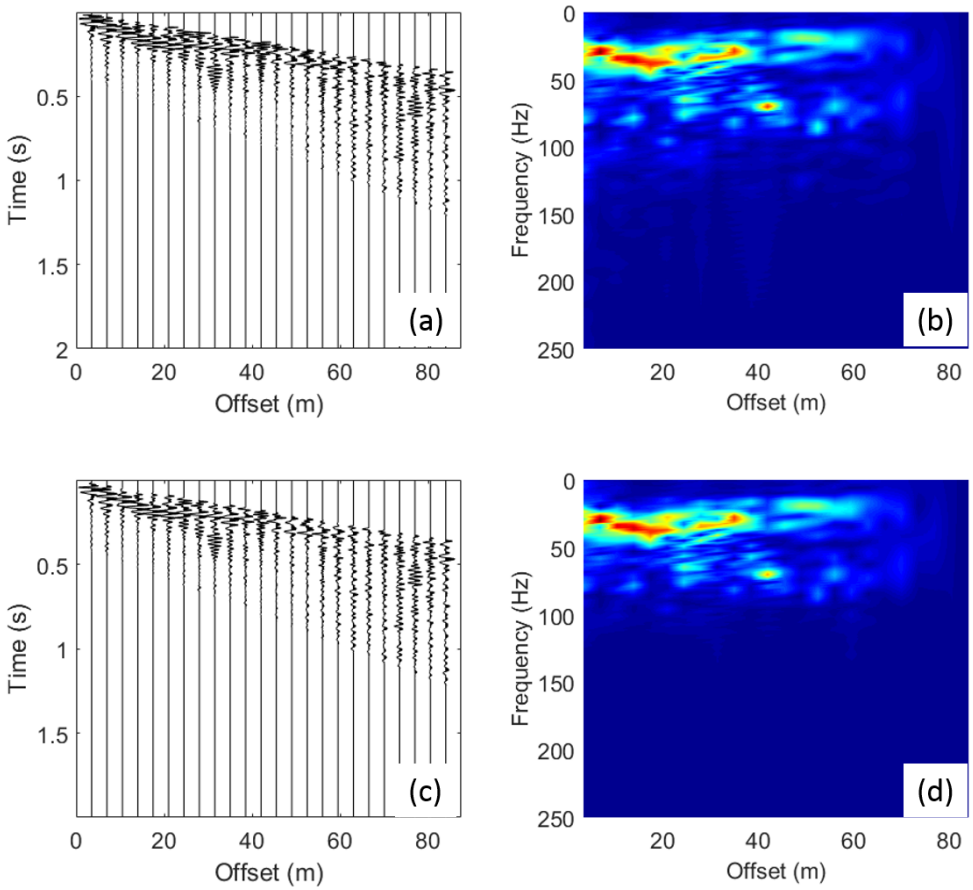

Figure 7. Line 1 Rayleigh wave data comparison before (a) and after (c) applying a low pass filter (0 - 80 Hz). The f-x spectrum before (b) and after (d) applying filter.

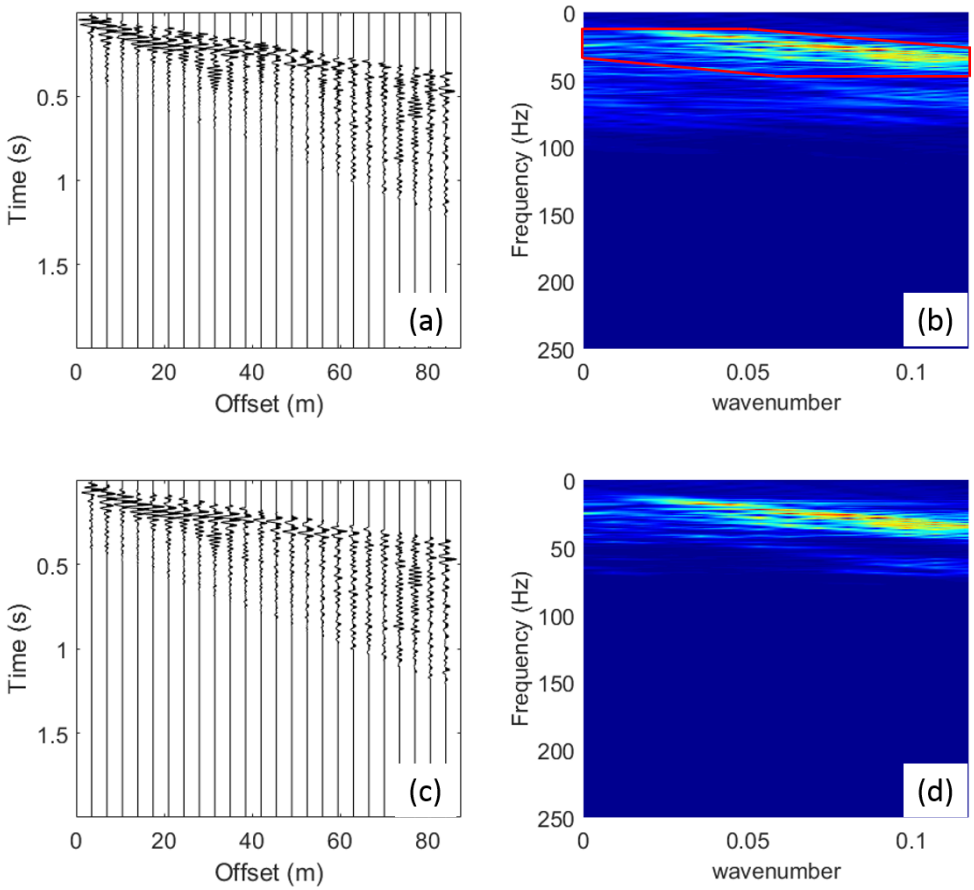

Figure 8. Line 1 Rayleigh wave data comparison before (a) and after (c) applying an f-k filter. The f-k spectrum before (b) and after (d) applying filter. The red polygon in (b) highlights the surface waves within the f-k domain which the f-k filter is designed to preserve.

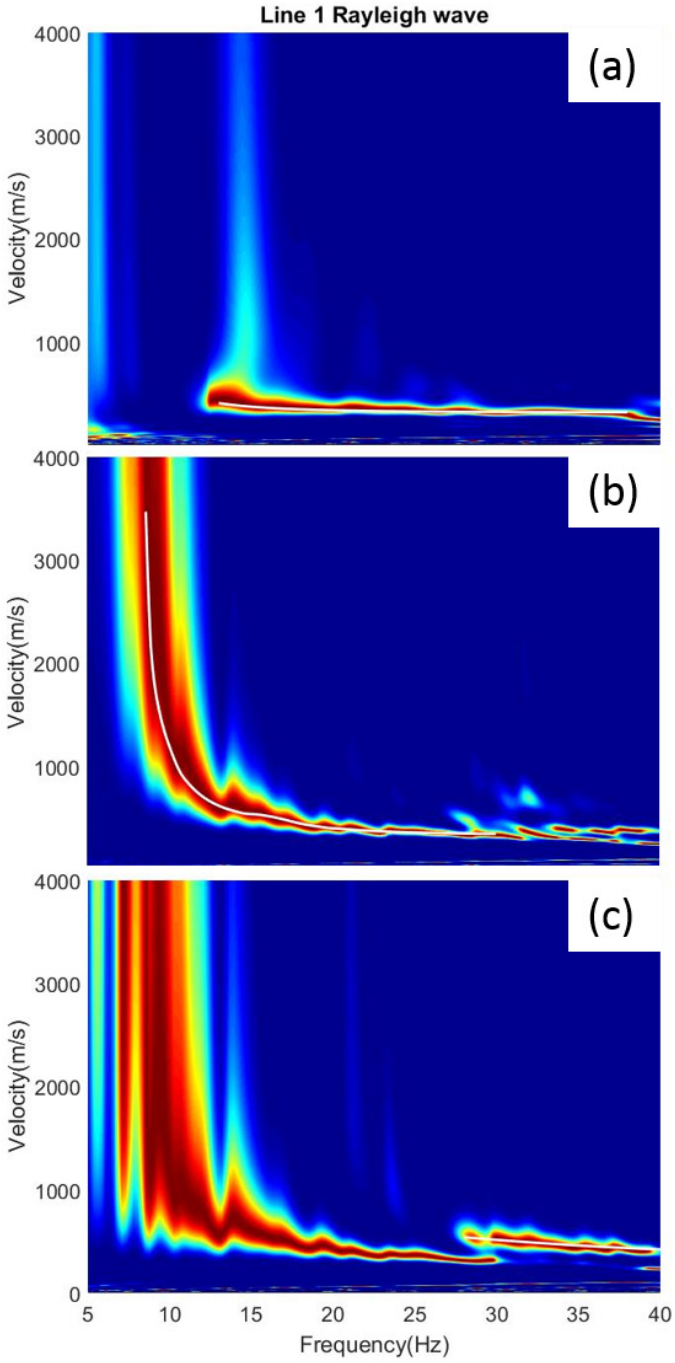

Figure 9. Line 1 Rayleigh wave with the obtained dispersion curve from different windowing. (a) Fundamental mode (From 1st to 10th geophones) (b) First higher mode (From 4th to 17th geophones) and (c) Second higher mode (From 7th to 16th geophones).

6.1.1.2 Love wave

For the Love wave data, the same processing workflow including stacking (Figure 10), normalizing the traces (Figure 11a), muting (Figure 11b), low pass filter (0 – 80 Hz) (Figure 12), and f-k filters (Figure 13) was followed.

However, the only windowing applied was to remove the last few traces to remove the noisy data, enabling identification of fundamental and first higher modes from 1st to 17th geophone offset (Figure 14).

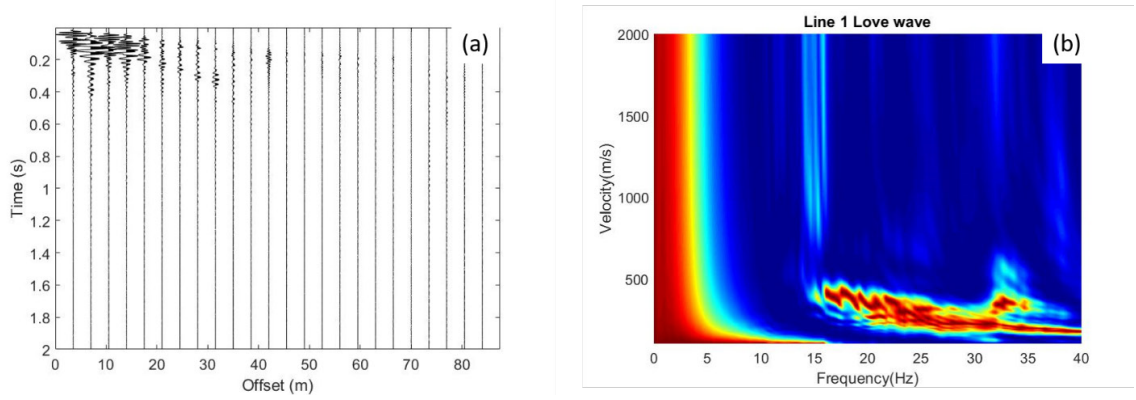

Figure 10. Line 1 Love wave analysis from Mirror Lake (a) Seismic record of the gather after stacking transverse components from five shots; the seismic traces show that the energy decreases rapidly with time and distance. (b) Phase velocity image before additional processing; all the modes are stacked together and it is hard to identify separate modes.

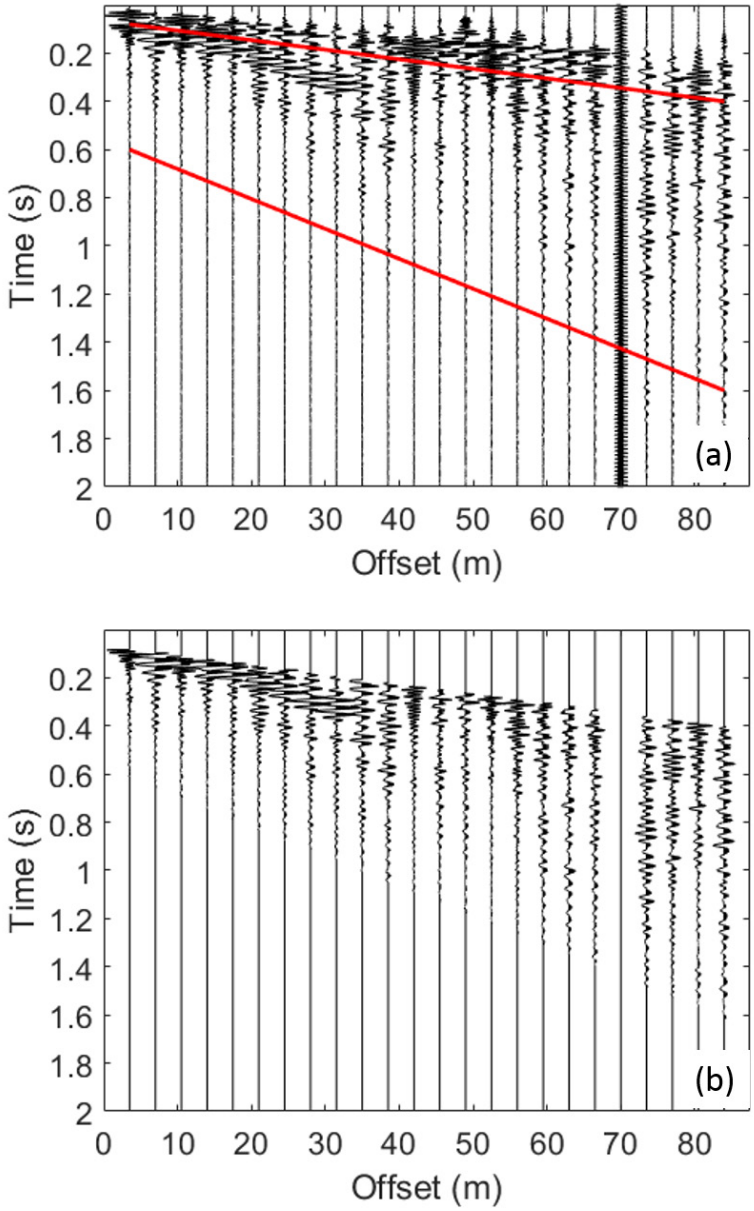

Figure 11. (a) Line 1 Love wave normalized seismic trace with top and down muting to preserve the surface wave only. The seismic data was preserved within two red lines. The body waves were muted from the top and the noise from the bottom is also muted. In the Love wave dataset, the bad trace was also removed. (b) Line 1 Love wave data after applied muting.

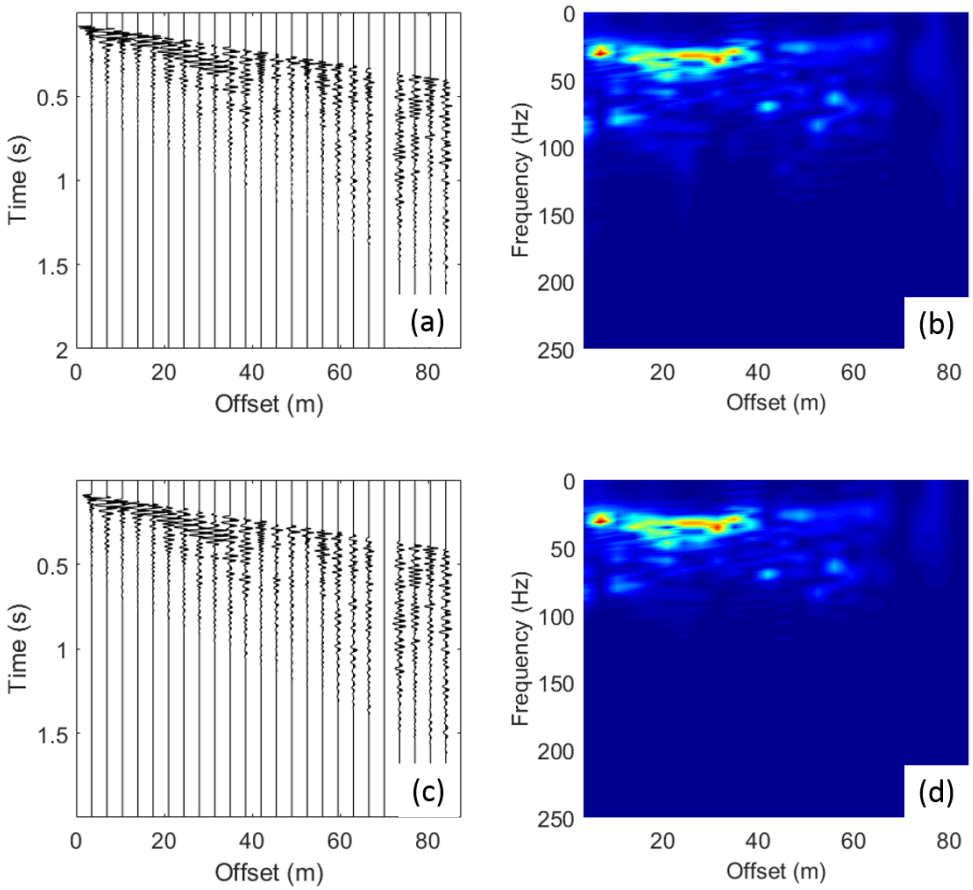

Figure 12. Line 1 Love wave data comparison before (a) and after (c) applying a low pass filter (0 - 80 Hz). The f-x spectrum before (b) and after (d) applying filter.

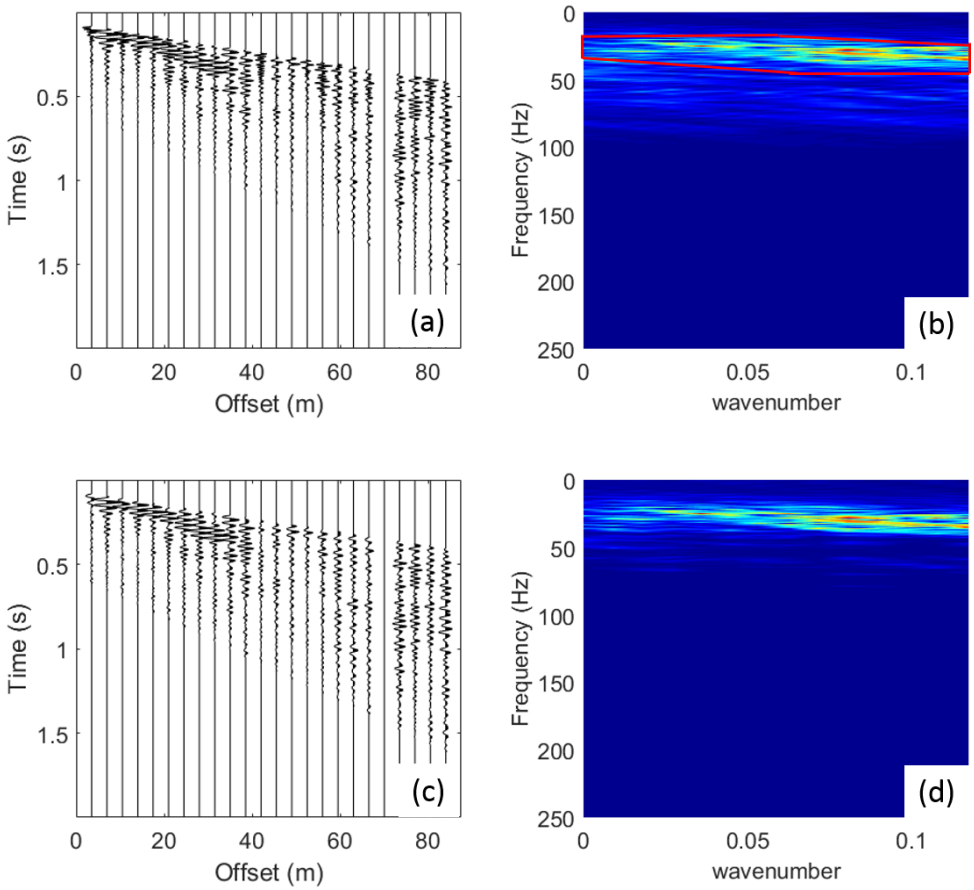

Figure 13. Line 1 Love wave data comparison before (a) and after (c) applying an f-k filter. The f-k spectrum before (b) and after (d) applying filter. The red polygon in (b) highlights the surface waves within the f-k domain which the f-k filter is designed to preserve.

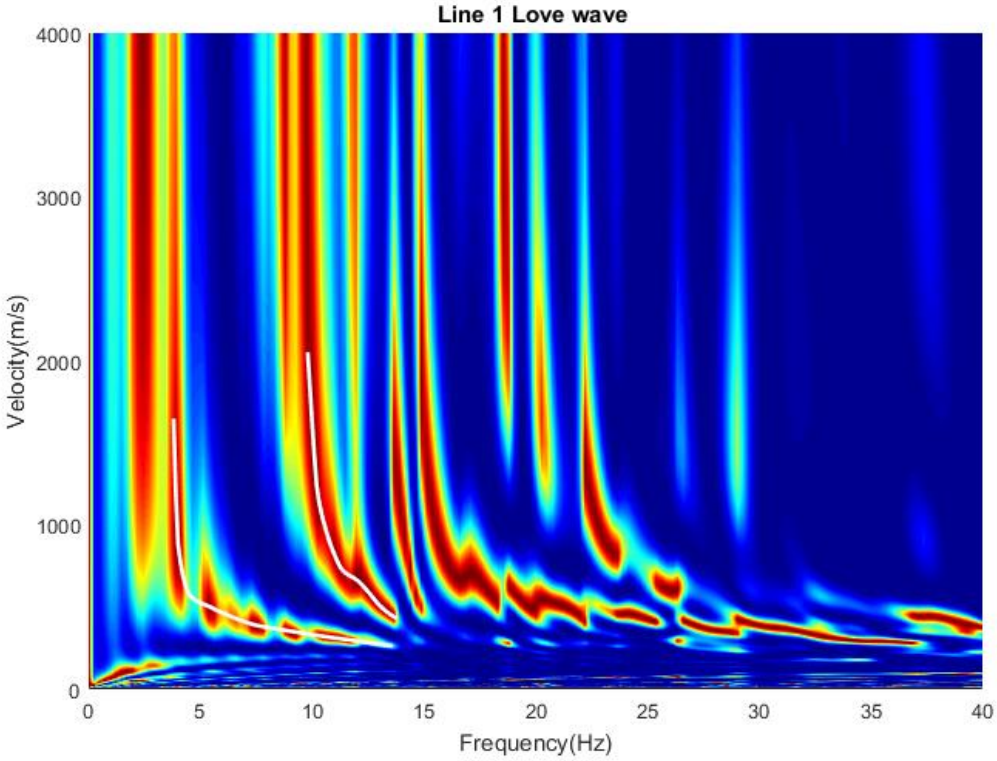

Figure 14. Dispersion curves for Line 1 Love wave with fundamental and first higher mode from 1st to 17th geophones.

6.1.2 Data Processing for Line 2

Data processing for Line 2 is similar to Line 1, and individual steps are not repeated here (some details are found in Appendix A). The windows applied to obtained dispersion curves for the Rayleigh wave are as follows: The fundamental mode was found from the 1st to 9th geophones; the first higher mode 7th to 18th geophone; and the second higher mode from the 1st to 24th geophones (Figure 15). For the Love wave data, the fundamental mode, first higher mode and second higher mode were obtained from 1st to 15th geophones (Figure 16).

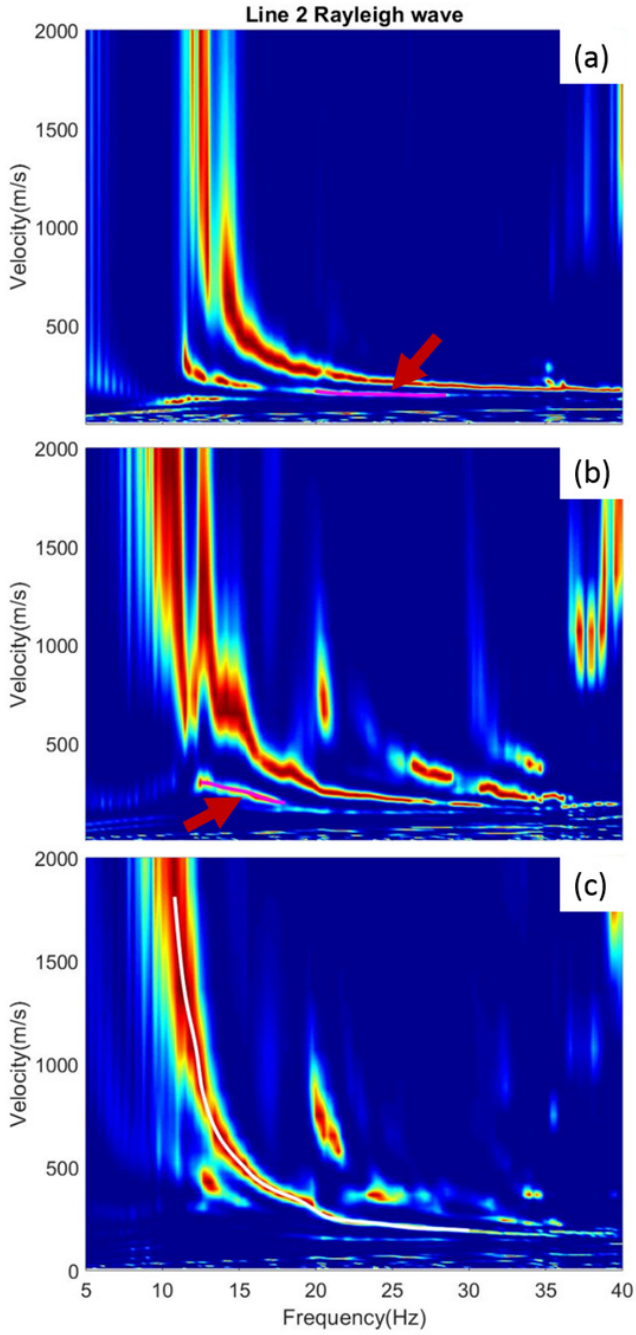

Figure 15. Line 2 Rayleigh wave with the obtained dispersion curve from different windowing. (a) Fundamental mode (From 1st to 9th geophones), (b) First higher mode (From 7th to 18th geophones) and (c) Second higher mode (From 1st to 24th geophones).

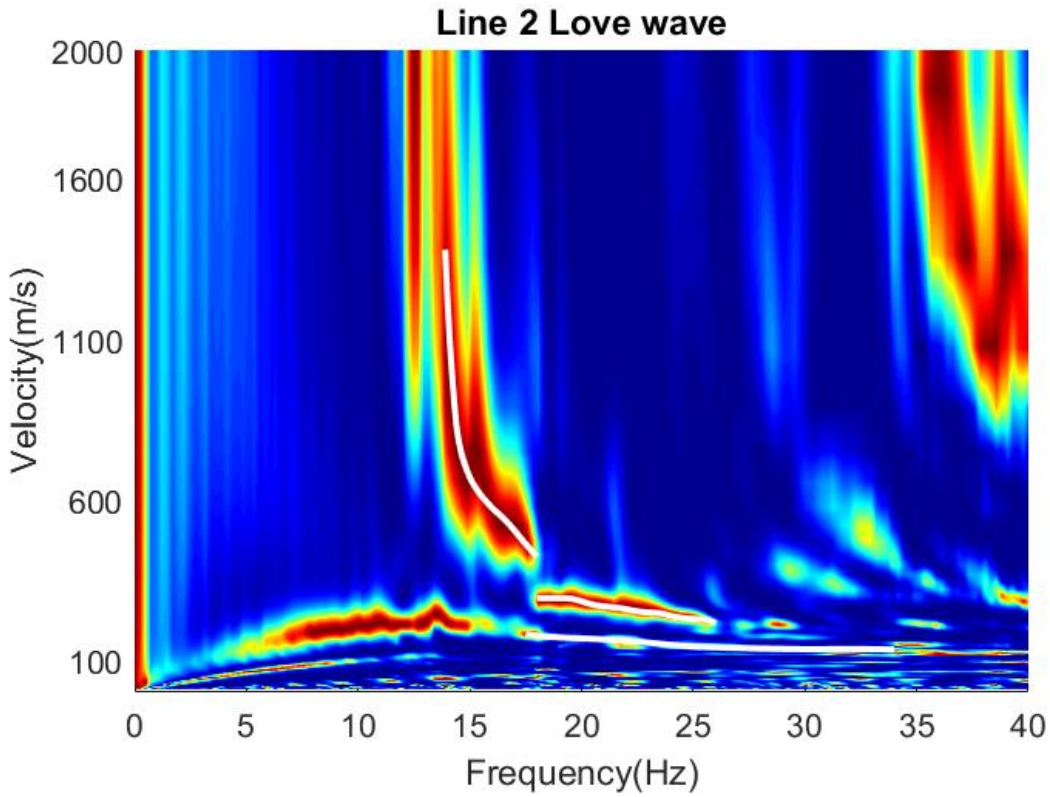

Figure 16. Dispersion curve for Line 2 Love wave with fundamental and first higher mode from 1st to 15th geophones.

6.2 Hannahville Indian Community, Michigan

Since the geology of the Hannahville Indian Community, Michigan, consists of layered sedimentary rocks, it was easier to obtain different dispersion curves. For this dataset, the same workflow in Table 1 was used; however, windowing was not required as different modes were distinguishable for all offset ranges except for the Love wave data of Line 6. However, the "Mode Kissing" phenomenon was observed in this dataset (Gao et al. 2016, Xia et al. 2012). Mode Kissing phenomenon is when two different modes nearly meet at some frequencies, it is commonly seen in near-surface models and usually occurs in low

frequencies between the fundamental mode and first higher mode. It is also noted that the fundamental mode energy is relatively low, which by increasing the iterations in HRLRT, the fundamental mode almost disappears and almost impossible to identify. Therefore, a lower iteration number was used during the HRLRT to provide better observe the dispersion curves of low energy modes. The processing detail will be in Appendix A.

6.2.1 Data Processing for Line 3

For Line 3, the fundamental and first higher modes of the Rayleigh waves (Figure 17) and fundamental and first higher modes of the Love waves were obtained (Figure 18). In this dataset, it was difficult to pick the dispersion curve at the higher frequency since the dispersion curve was not distinguishable.

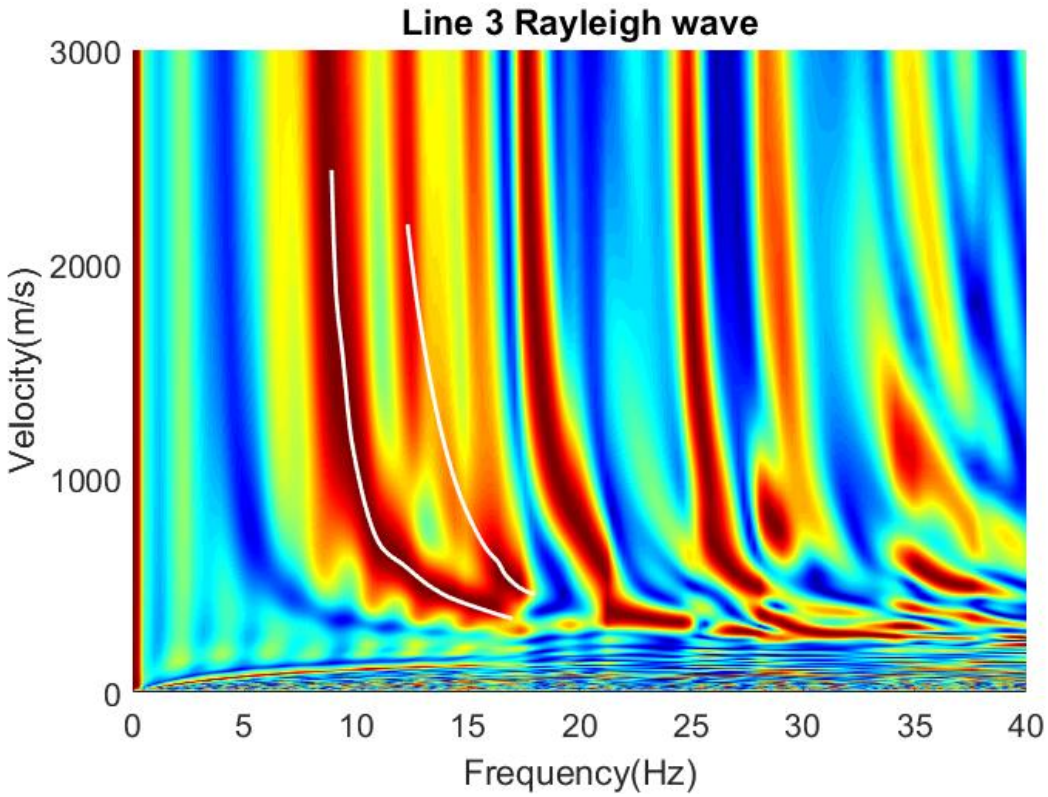

Figure 17. Dispersion curve for Line 3 Rayleigh wave with the fundamental and first higher mode.

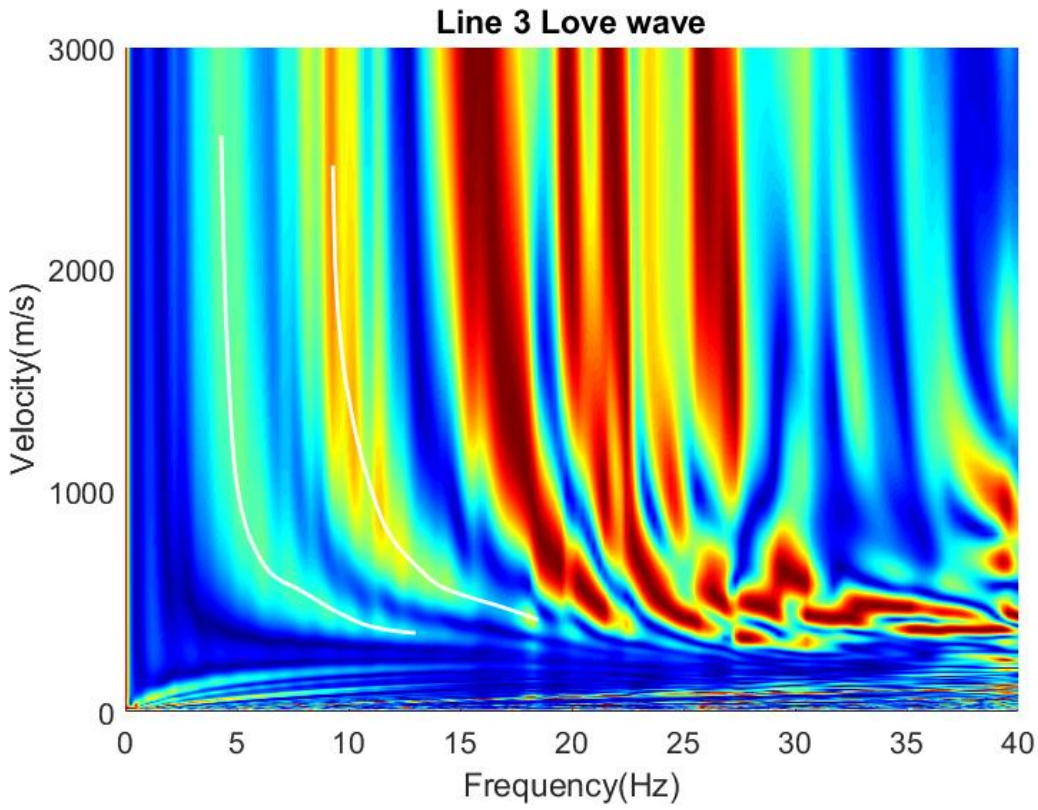

Figure 18. Dispersion curve for Line 3 Love wave with the fundamental and first higher mode.

6.2.2 Data Processing for Line 4

For the Line 4 dataset, the fundamental and first higher modes of the Rayleigh wave (Figure 19) and fundamental and first higher modes of the Love waves were obtained (Figure 20). It is noted that the energy from the fundamental mode in both Rayleigh wave and Love wave are low. In this case, although increasing the iteration number in HRLRT yields a better resolution of higher modes, the fundamental mode is completely attenuated, which consequently might end up with wrong modal identification. In this dataset, the dispersion curve at higher frequencies was difficult to trace (>25 Hz).

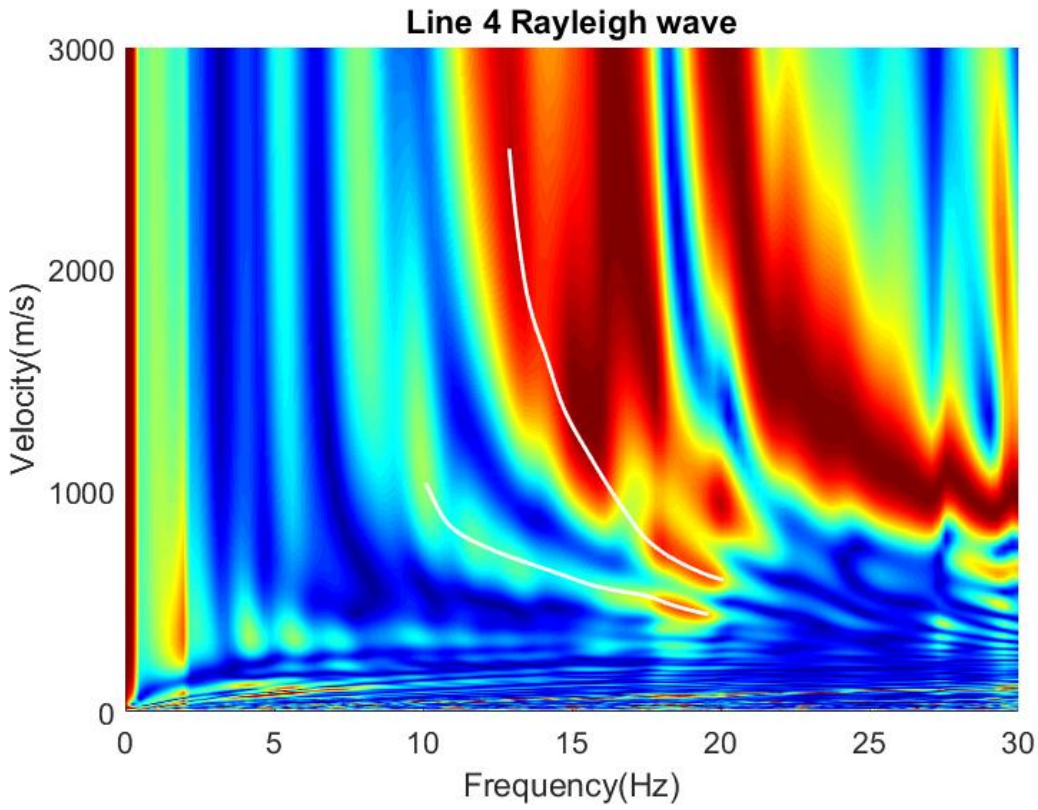

Figure 19. Dispersion curve for Line 4 Rayleigh wave with the fundamental and first higher mode.

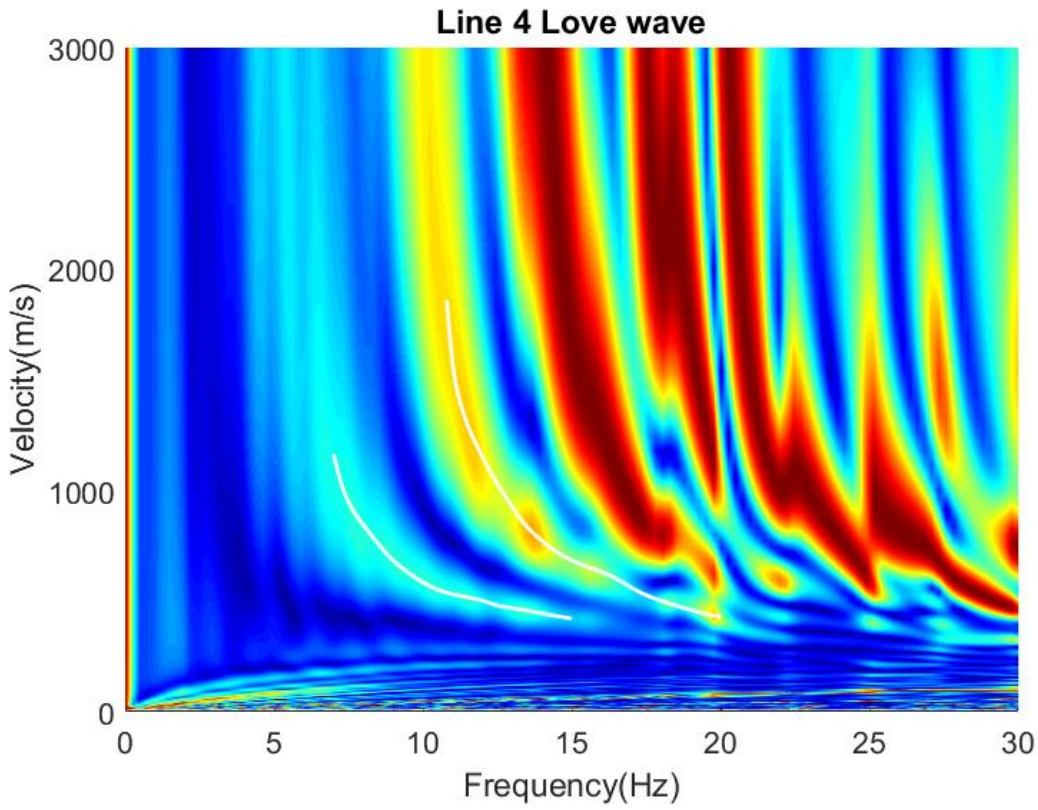

Figure 20. Dispersion curve for Line 4 Love wave with the fundamental and first higher mode.

6.2.3 Data Processing for Line 5

For Line 5, the fundamental and first higher modes of the Rayleigh waves (Figure 21) and fundamental, first higher and second higher modes of the Love waves were obtained (Figure 22).

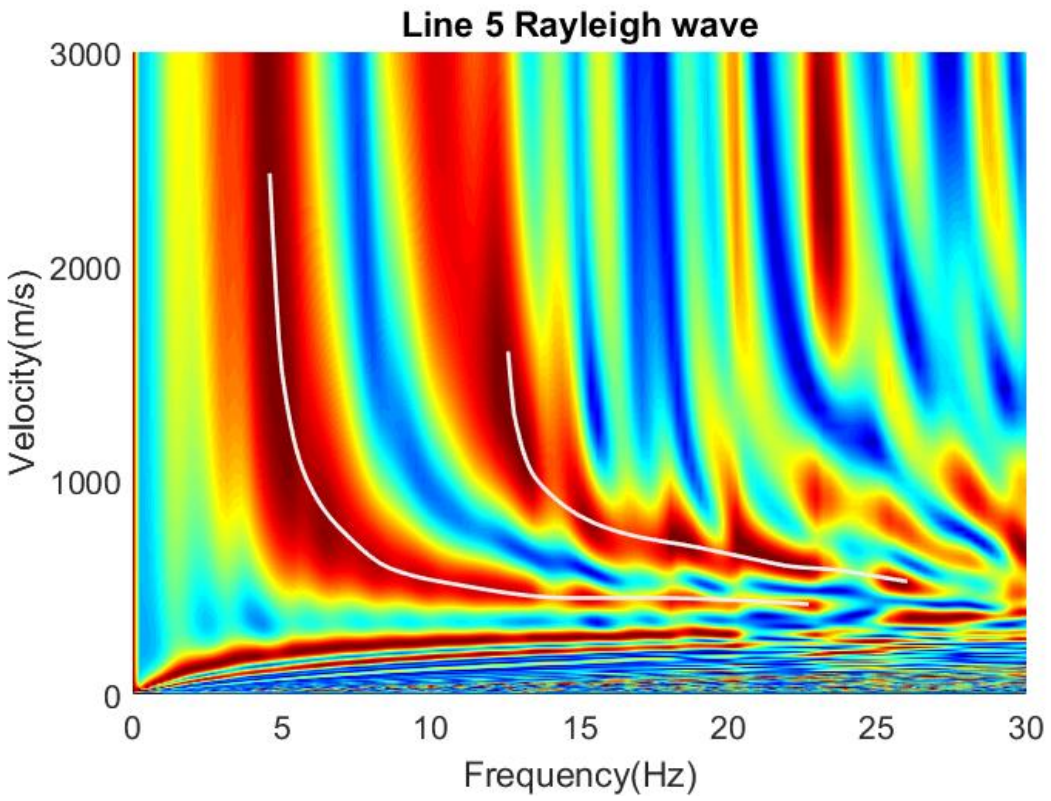

Figure 21. Dispersion curve for Line 5 Rayleigh wave with the fundamental and first higher mode.

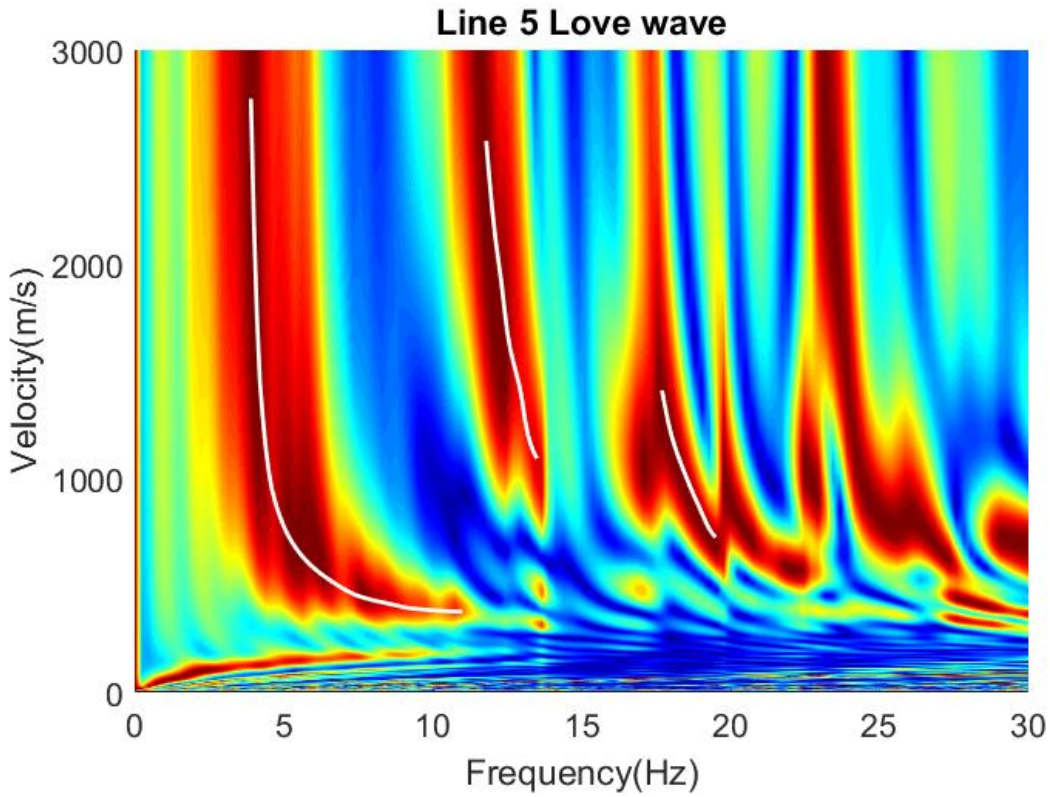

Figure 22. Dispersion curve for Line 5 Love wave with the fundamental, first higher mode and second higher mode.

6.2.4 Data Processing for Line 6

For Line 6, the fundamental and first higher modes of the Rayleigh waves (Figure 23) and the fundamental and first higher modes of the Love waves (Figure 24) were obtained. For the Rayleigh waves, the dispersion curve was quite distinguishable and by increasing the iteration number, the dispersion curve does not disappear and it was decided to proceed with higher iteration number to get more reliable dispersion curve. In addition, the dispersion curve up to 80 Hz was traced, unlike the other lines. For the Love wave data, however, it is hard to obtain the fundamental and first higher modes in the same

window. Like the approach followed in the Mirror Lake dataset, different windowing was applied to capture the fundamental and first higher modes (Figure 10 & 17). The fundamental mode was distinguishable from 1st to 11th geophones and the first higher mode from first to 20th geophones.

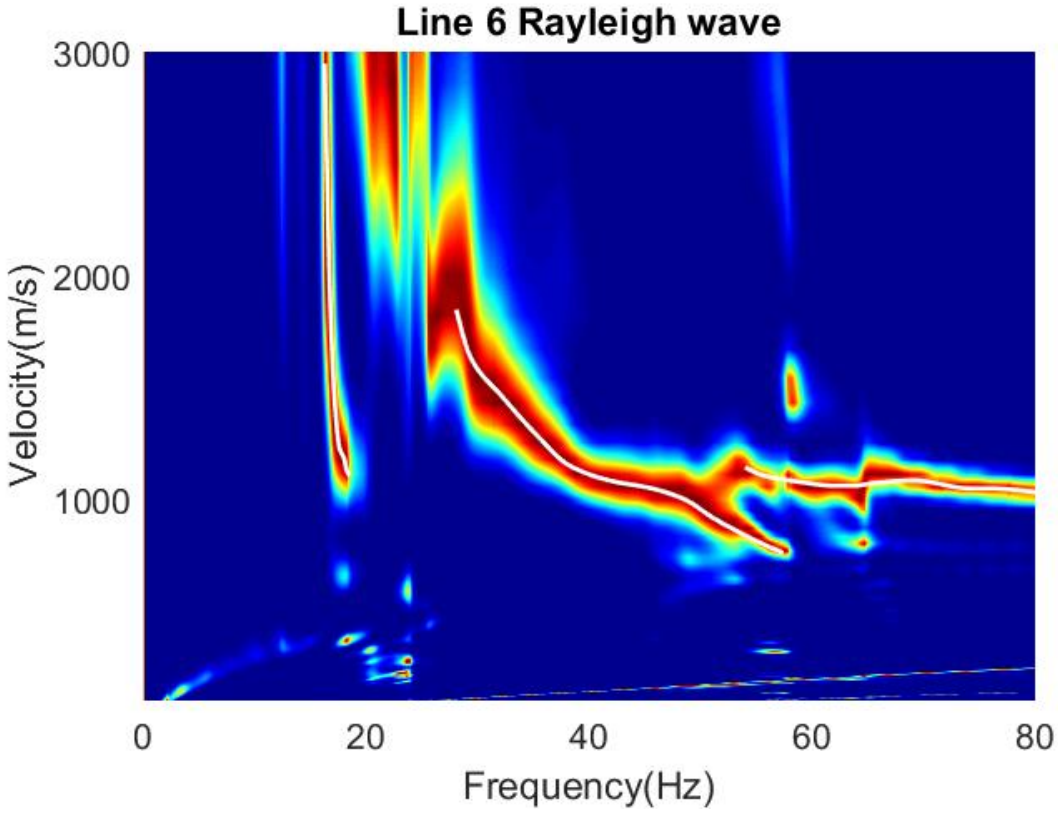

Figure 23. Dispersion curve for Line 6 Rayleigh wave with fundamental, first higher mode and second higher mode.

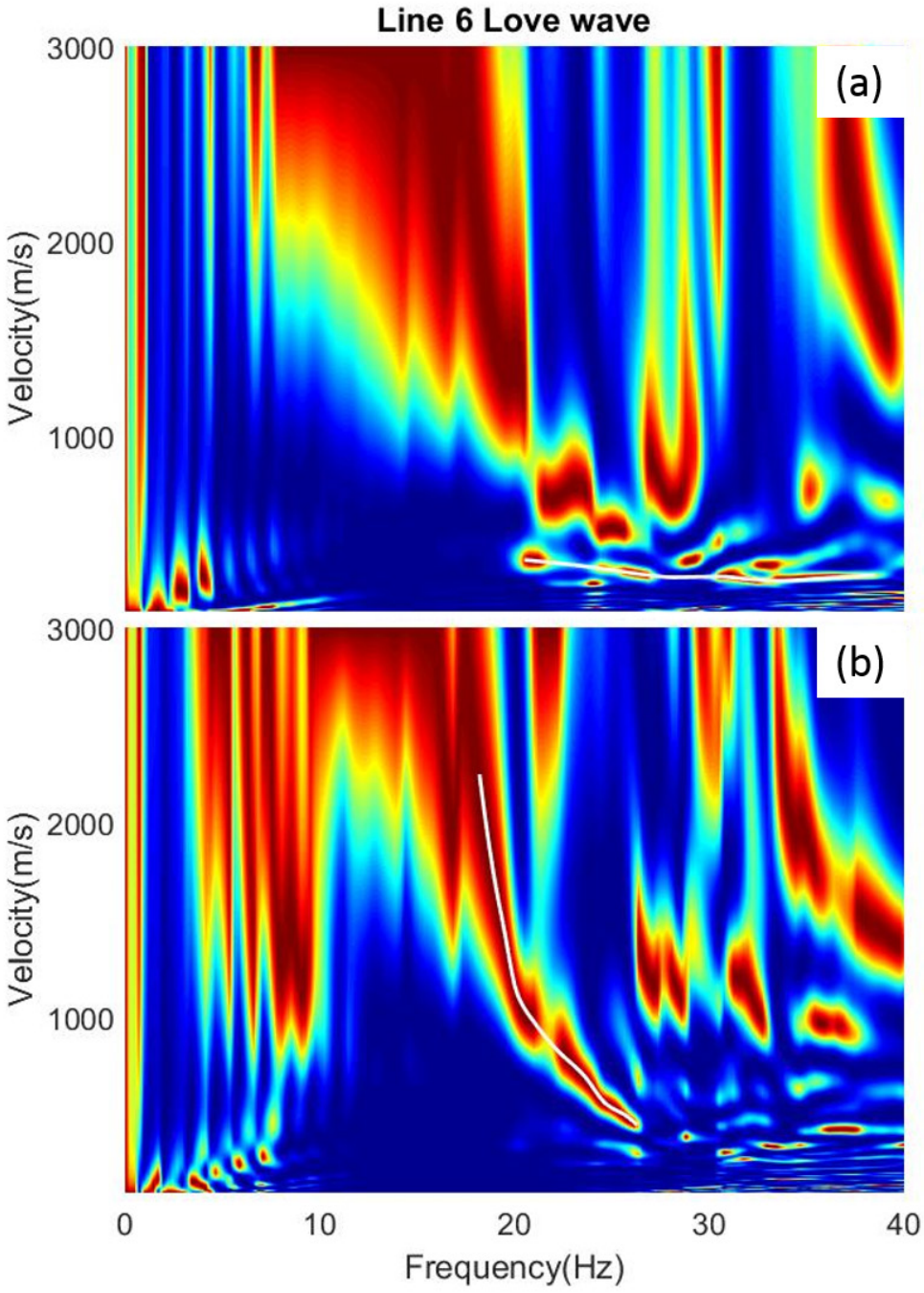

Figure 24. Dispersion curve for Line 6 Love wave with fundamental and first higher mode from different windowing. (a) Fundamental mode (From 1st to 11th geophones) and (b) First higher mode (From 1st to 20th geophones).

7 Data Inversion

After getting dispersion curve of all the lines, data inversion was performed to obtain the subsurface horizontally polarized and vertically polarized S-wave velocity profile from Love and Rayleigh waves. As mentioned in the earlier chapter, the Dinver software was used to apply inversion in this study. In the data inversion, the parameter range was defined, which include number of layers, layer thickness, and P and S-wave velocity. Amongst them, range of the S-wave velocity is critical part of inversion. In this section, a detailed explanation was provided to show how these parameters are defined.

7.1 Define number of layers

The length of the geophone array could usually provide the similar length of the depth of investigation. In these datasets, since the geophone array have total length are at least 80.5 m, it was targeted to have S-wave velocity profile up to the depth of 80 meters.

To determine the suitable number of layers in this study, the inversion was performed with considering different number of layers from two to fifteen and evaluate the models from the misfit value. It was noticed that with the increase of the layer number, the misfit value decreased, the theoretical dispersion curve calculated from the inversion results will be closer to the observed dispersion curve (Figure 25). It was also noted that after the number of layers exceeds eight, the misfit value reaches a plateau and didn't have significant improvement. Therefore, I considered 8 layers for the inversion processing to have reliable results and also to save on the computational time. To determine the

iteration number of the inversion, it was observed from all the dataset that after reaching 10,000 models (200 iterations) the solutions will converge (Figure 26). However, 25,000 models (500 iterations) were generated in each inversion to make sure the solutions converged to the global solution close to the true model.

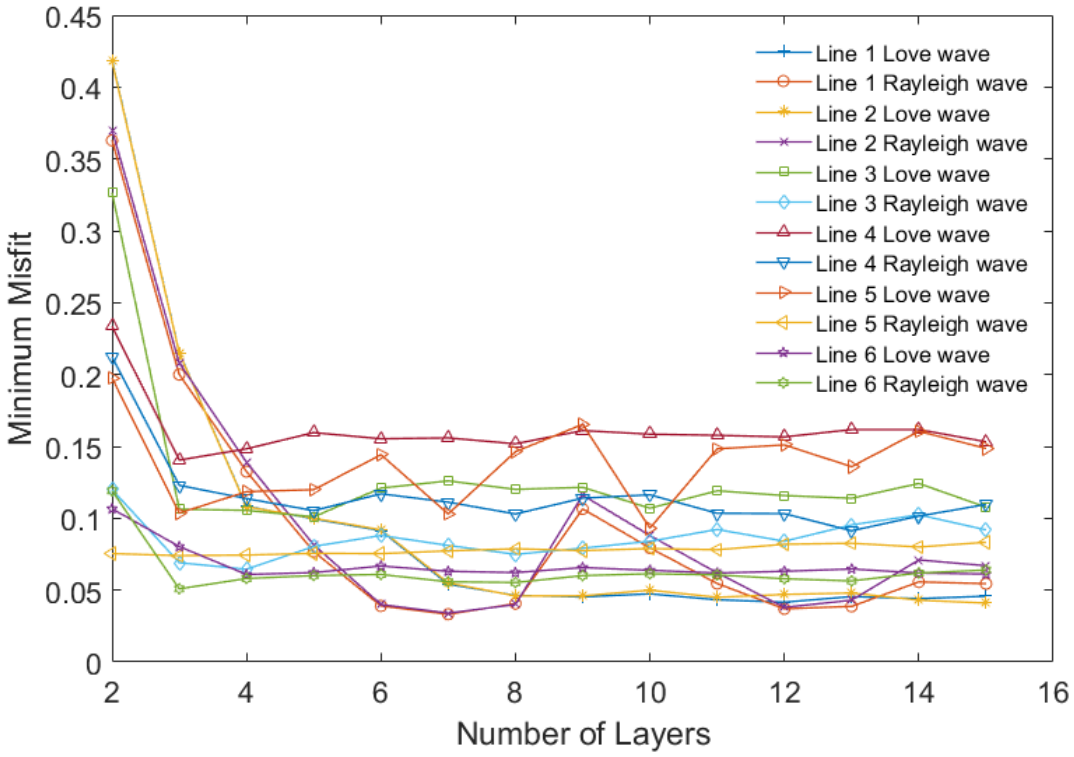

Figure 25. To define the layer number, note that after reach layer number of 8 the minimum misfit doesn't have significant improvement.

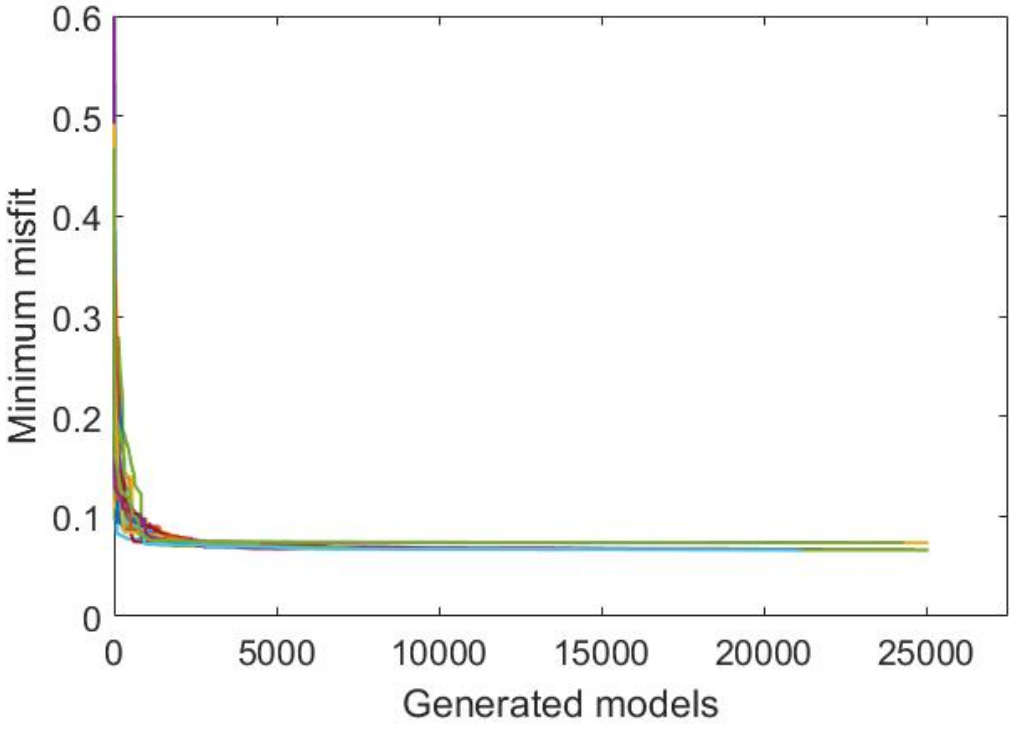

Figure 26. During the inversion process, the minimum misfit reaches to solution after generated 10000 models.

7.2 Layer Thickness

With the number of layers determined, having proper layer thickness in each layer is the next step. To define the layer thickness, the joint inversion on Rayleigh and Love wave was performed, considering the subsurface as isotropic medium to get thickness information of each layer. To avoid the bias on the data, the inversion was run 20 times with different initial models, with each layer in 5-15 meter range. To prevent bias on a single solution, the weighted average of the inversion results was calculated. With 20 inversion results, the weighted average with a weighted vector was calculated via

equation (12) based on misfit value and define the thickness of each layer, where m_i is the misfit value of each inversion results.

$$w_i = \frac{\left(\frac{1}{m_i}\right)^2}{\sum_{i=1}^{20}\left(\frac{1}{m_i}\right)^2} \qquad (12)$$

With the number of layers and the layer thickness defined from joint inversion of each lines, the inversion of Love wave and Rayleigh wave was performed.

7.3 Inversion of Love wave and Rayleigh wave

Since the inversion was based on neighborhood algorithm, the final result is usually checked with running the same inversion several times and observe if the results converge to the same trend (Wathelet et al. 2004). To make sure the results are reliable, the inversion (Love and Rayleigh wave inversion in each lines) was done 20 times while each being started with different random seeds. The following figures (Figure 27-44) have shown the inversion result of each lines and the horizontal and vertical S-wave velocity profile.

The velocity profiles from Line 1 dataset is shown in Figure 27, in this dataset, the Rayleigh wave result has smaller variation than Love wave data. Since in this dataset, three different modes in Rayleigh wave are incorporated into inversion (Figure 28) which have more constrained since the only fundamental and first higher modes are used in Love wave dataset (Figure 29). Also noted that with the increase of the depth the range of

the possible solution is wider, the reason is the limited low-frequency data gave us the low resolution in the deeper layers.

The velocity profiles from Line 2 dataset is shown in Figure 30. In this dataset, both Rayleigh wave (Figure 31) and Love wave (Figure 32) data incorporated fundamental mode, first and second higher modes into dispersion curve inversion. Overall the Love wave inversion result is more coverage than Rayleigh wave dataset, Safani et al. (2005) also noted that Love wave inversion shown more stability and sensitivity than Rayleigh wave inversion with a simple fundamental mode dominated model and in this dataset Love wave inversion seems more stable in joint inversion as well. Again, in this dataset low-frequency data is lacked therefore in the deeper layer shows more uncertainty.

The velocity profiles from Line 3 dataset is shown in Figure 33. In this dataset both Rayleigh wave (Figure 34) and Love wave (Figure 35) data incorporated fundamental mode and first higher mode into dispersion curve inversion. The solutions of both Love wave and Rayleigh wave inversion are within a small range up to around 50 m (The 6^{th} layer) and after this, the uncertainty of the solutions increased. The vertical resolution might be good up to this point.

The velocity profiles from Line 4 dataset is shown in Figure 36. In this dataset both Rayleigh wave (Figure 37) and Love wave (Figure 38) data incorporated fundamental mode and first higher mode into dispersion curve inversion. Horizontal shear wave velocity from Love wave up to 60 m is more converged toward a solution while the vertical shear wave velocity from Rayleigh wave have more uncertainty. The Love wave

dispersion curves have more low-frequency data (<10 Hz) which provide more vertical resolution than Rayleigh wave.

The velocity profiles from Line 5 dataset is shown in Figure 39. In this dataset Rayleigh wave (Figure 40) data incorporated fundamental and first higher modes into dispersion curve inversion and Love wave (Figure 41) data incorporated fundamental mode, first higher mode and second higher mode into dispersion curve inversion. In this dataset, the Love wave inversion result seems to have smaller uncertainty than Rayleigh wave data in the deeper depths since second higher modes are included in the Love wave dataset.

The velocity profiles from Line 6 dataset is shown in Figure 42. In this dataset Rayleigh wave (Figure 43) data incorporated fundamental mode, first higher mode and second higher mode into dispersion curve inversion. Love wave (Figure 44) data incorporated fundamental mode and first higher mode into dispersion curve inversion. The variation of the solutions increased after around 40 m (the 5^{th} layer). From the 6^{th} layer, the velocities below are within the same range between Love wave and Rayleigh wave dataset. Although in this dataset Rayleigh wave inversion included second higher mode but since both Love wave and Rayleigh wave data are lacked of low-frequency data (< 10Hz) the vertical resolution in this line is limited.

Overall, in general, from all the dataset the results are more stable from Love wave dataset than Rayleigh wave dataset except for Line 1 since more modes in Rayleigh wave dataset is used for dispersion curve inversion it provides more constraint to the inversion.

With the increased of the depth, the inversion results might be more unreliable since the limitation of the low-frequency data and reached the limitation of the vertical resolution.

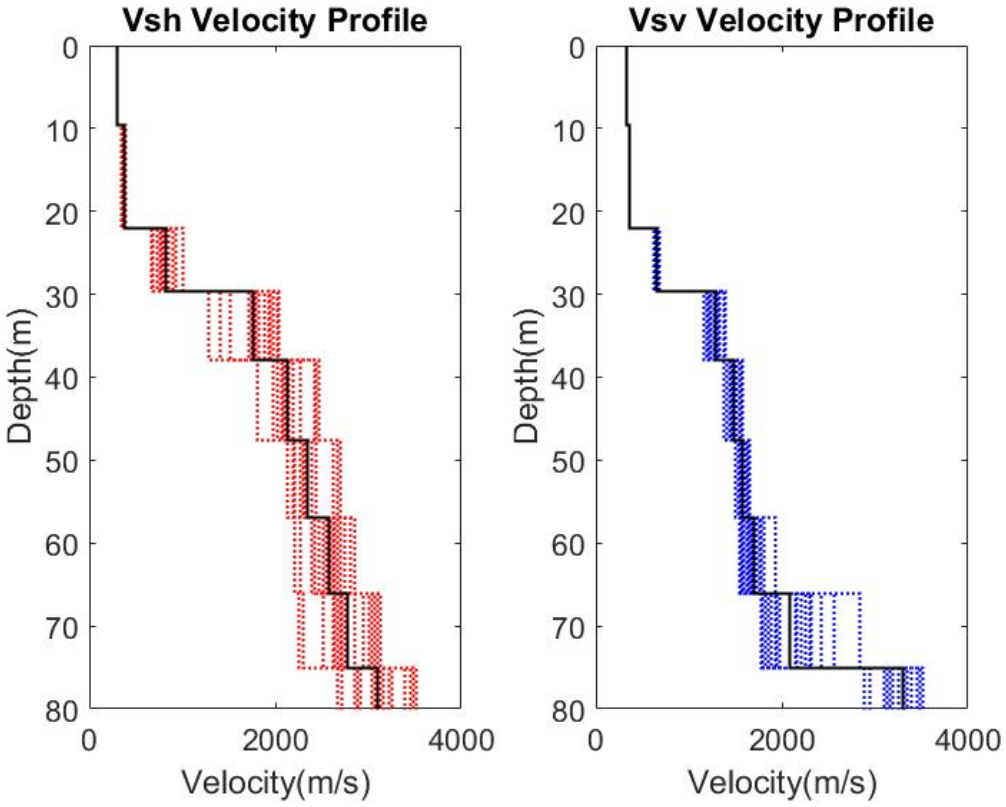

Figure 27. Inversion results of Line 1. The dot lines are all result from 20 different inversions, the solid black line is the weighted average of all the results.

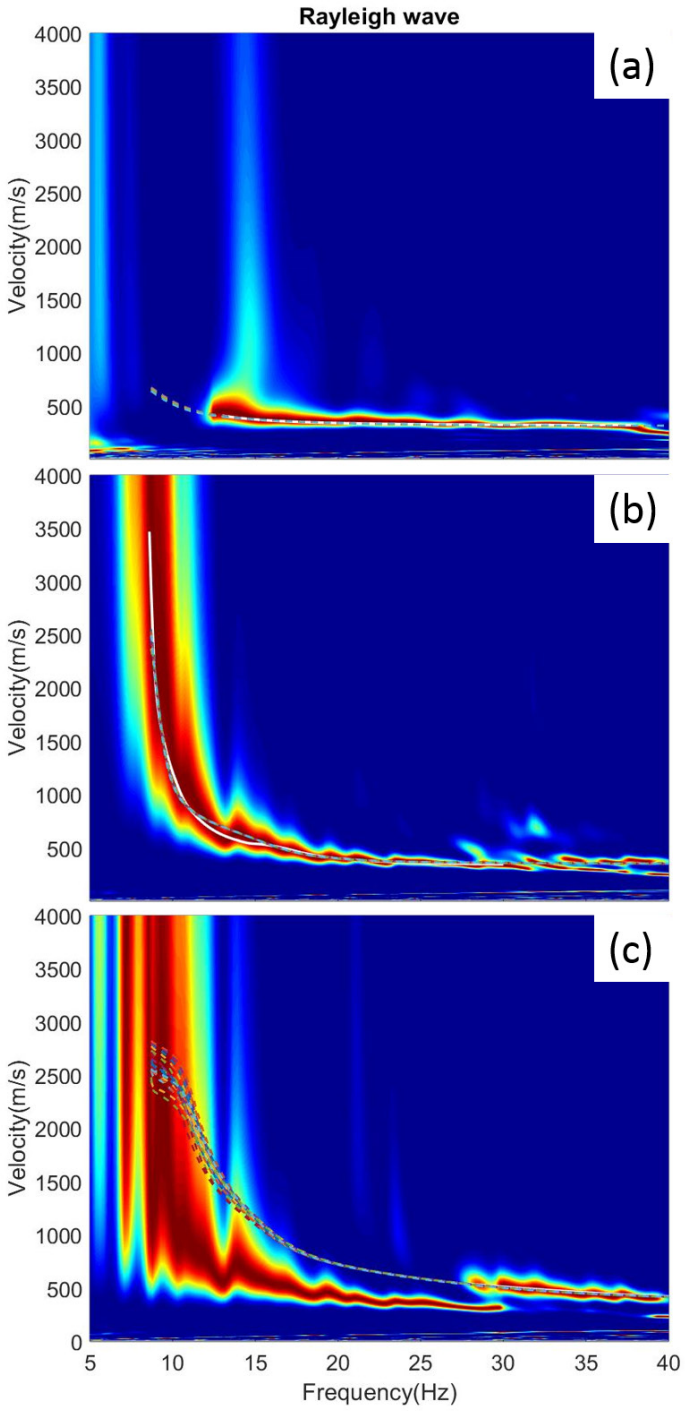

Figure 28. Comparison of the observed curve (solid lines) and the calculated theoretical curves (dash lines) of Line 1 Rayleigh wave from the twenty models shown in Figure 29.

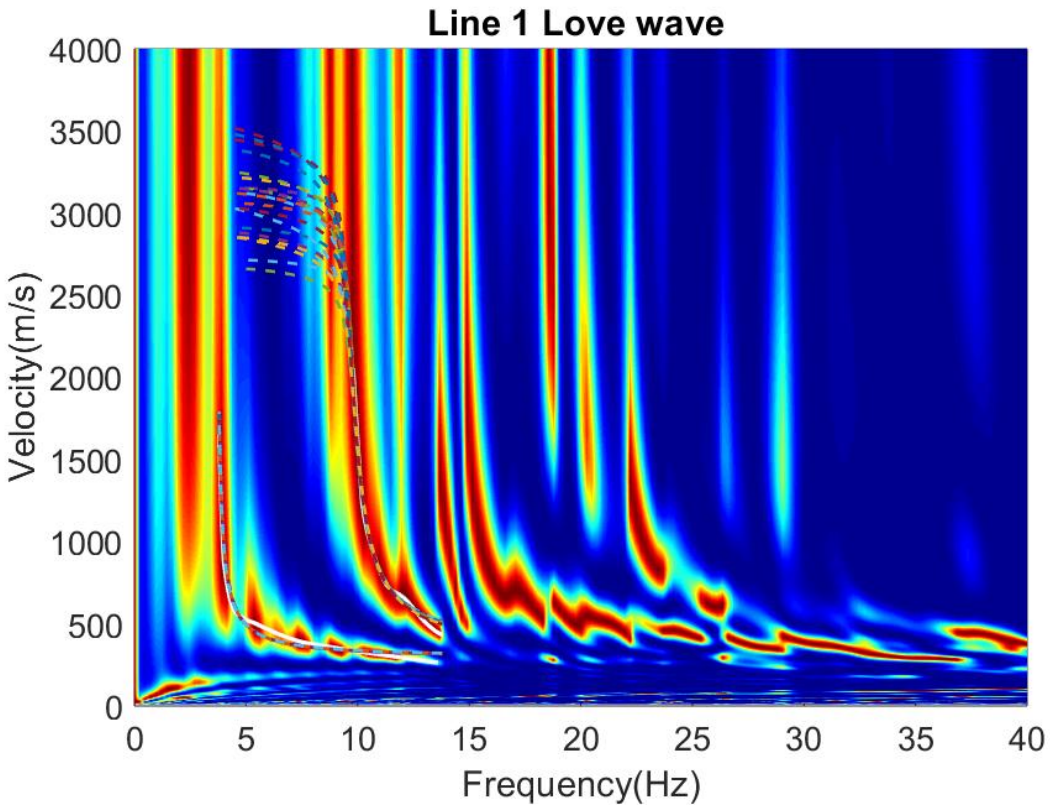

Figure 29. Comparison of the observed curve (solid lines) and the calculated theoretical curves (dash lines) of Line 1 Love wave from the twenty models shown in Figure 29.

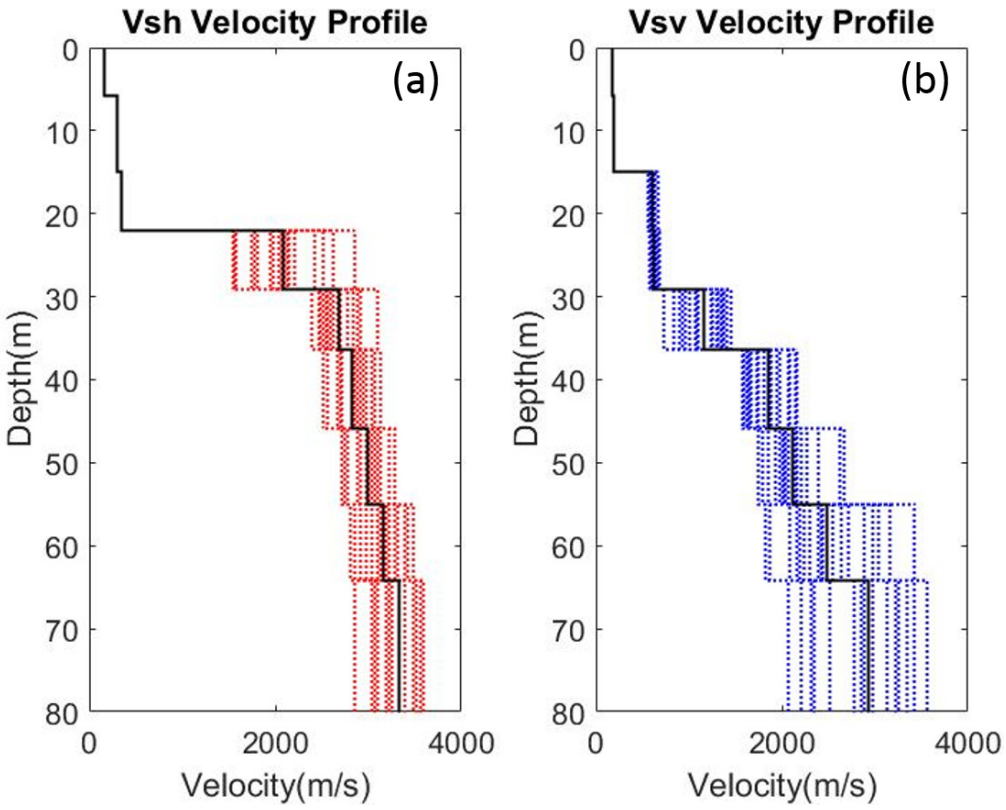

Figure 30. Inversion results of Line 2. The dot lines are all result from 20 different inversions, the solid black line is the weighted average of all the results.

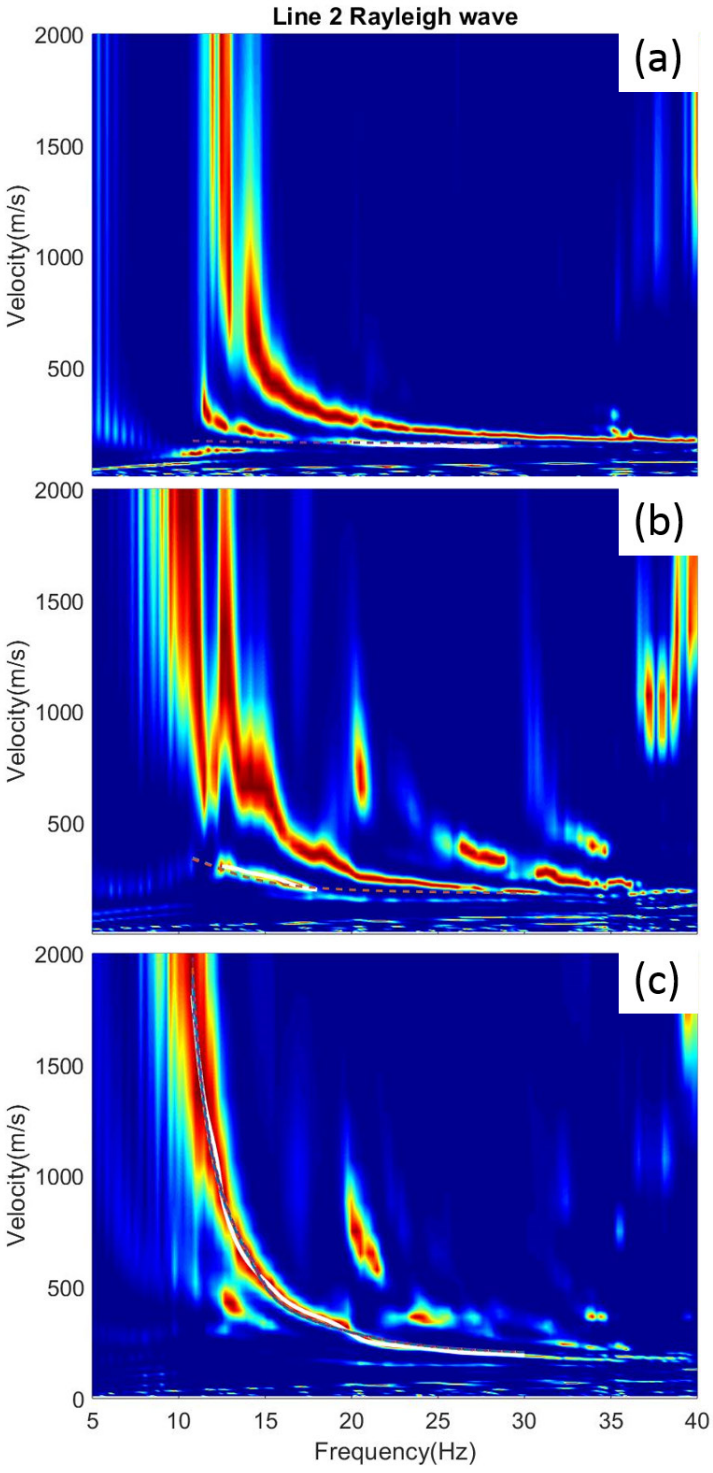

Figure 31. Comparison of the observed curve (solid lines) and the calculated theoretical curves (dash lines) of Line 2 Rayleigh wave from the twenty models shown in Figure 32.

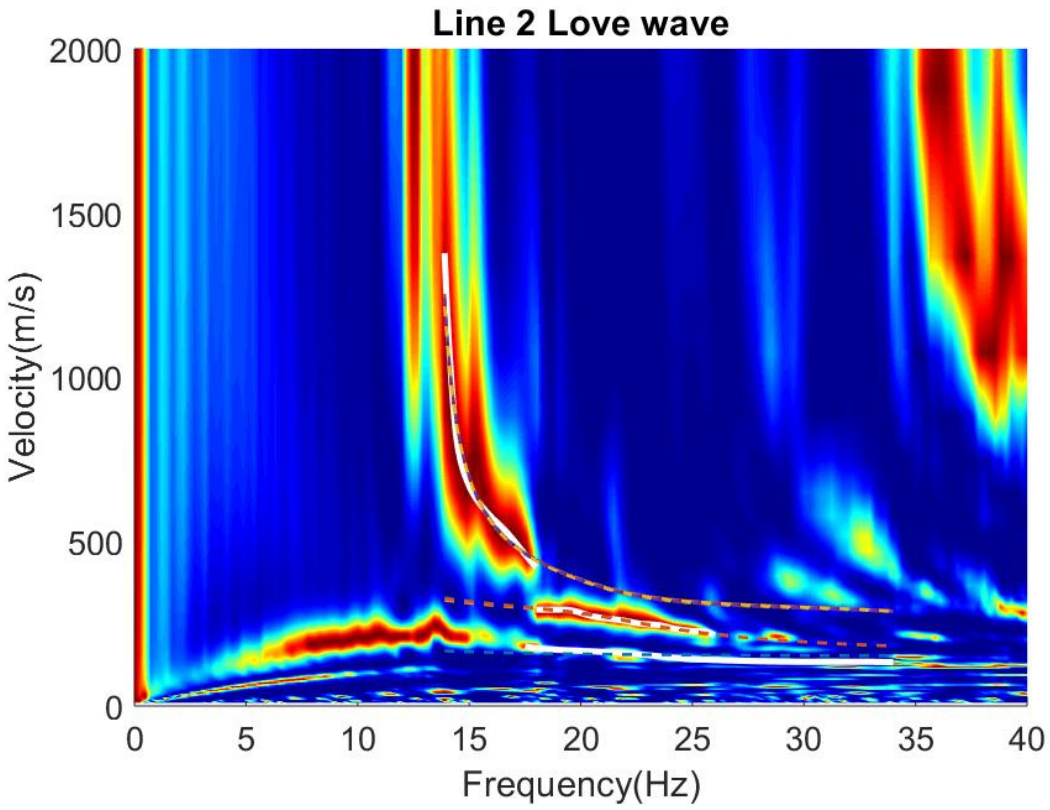

Figure 32. Comparison of the observed curve (solid lines) and the calculated theoretical curves (dash lines) of Line 2 Love wave.

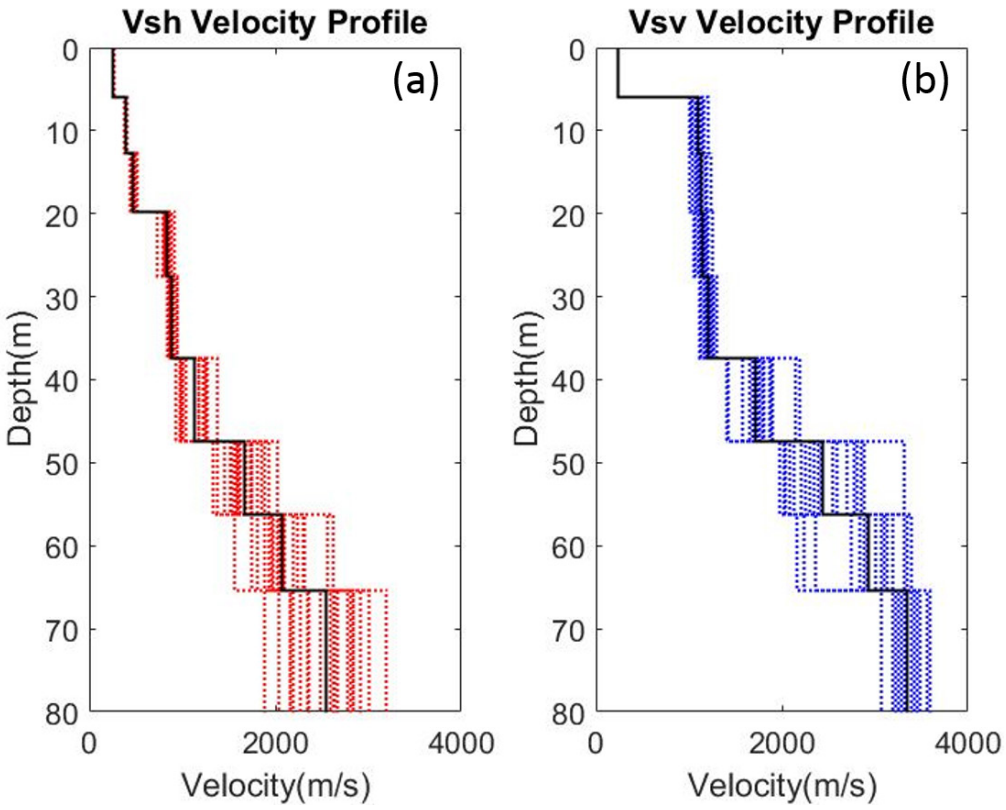

Figure 33. Inversion results of Line 3. The dot lines are all result from 20 different inversions, the solid black line is the weighted average of all the results.

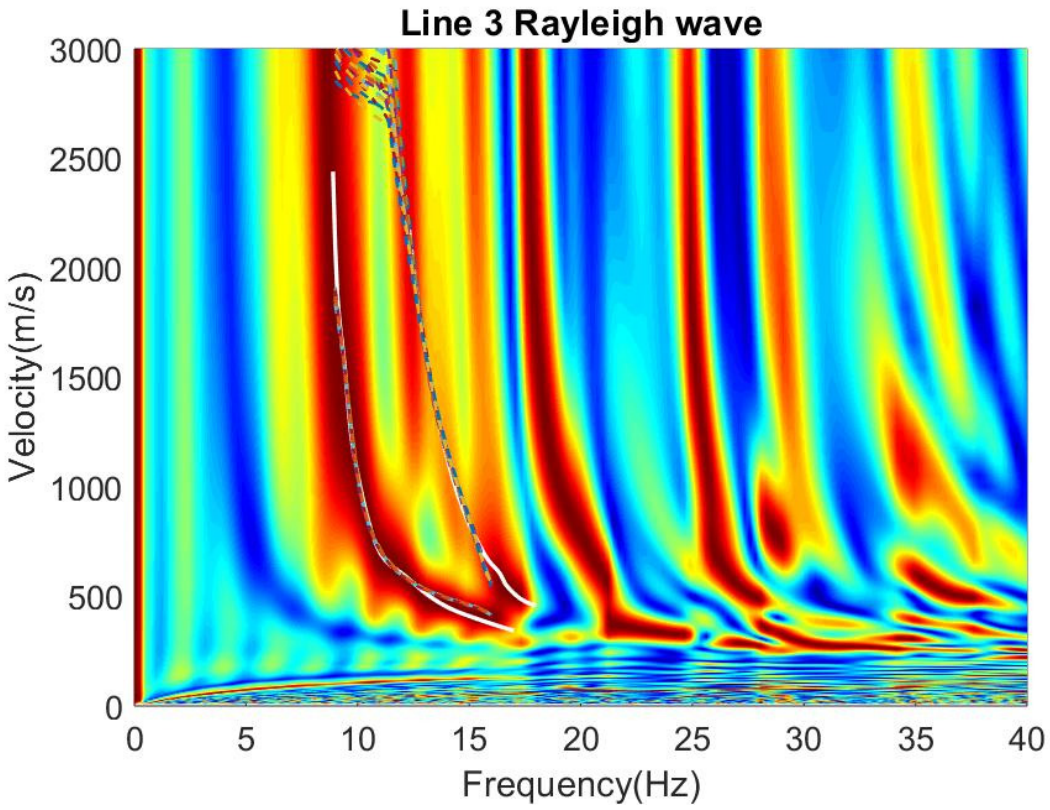

Figure 34. Comparison of the observed curve (solid lines) and the calculated theoretical curves (dash lines) of Line 3 Rayleigh wave from the twenty models shown in Figure 35.

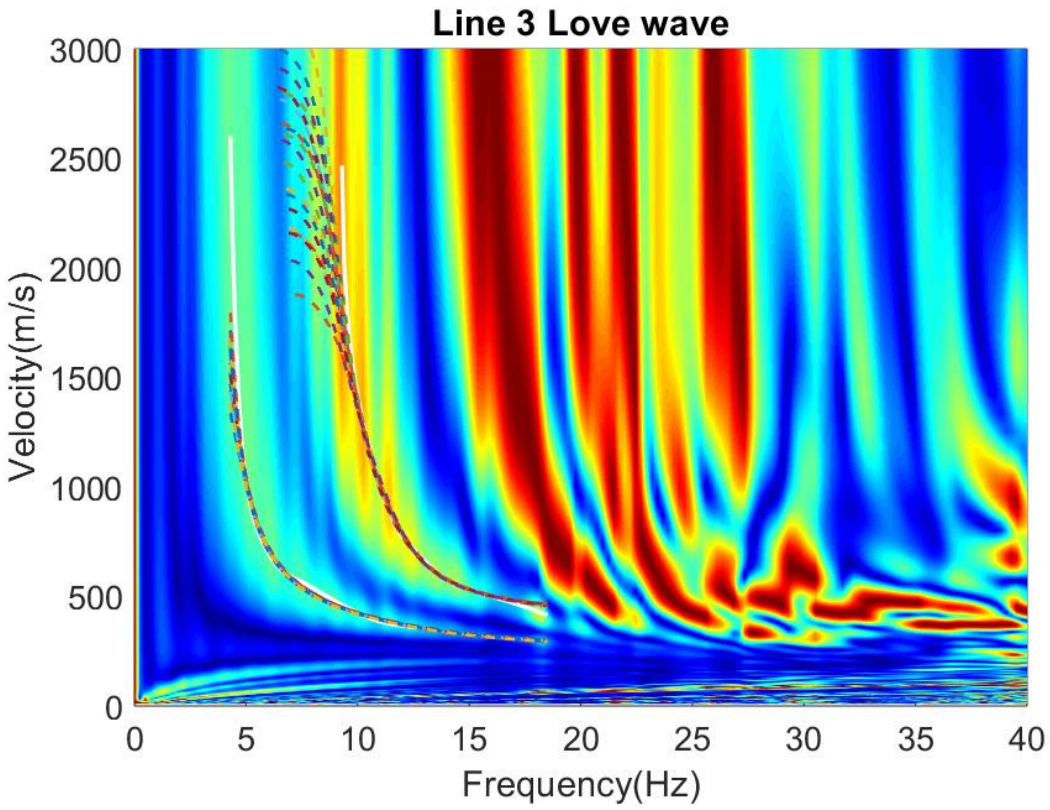

Figure 35. Comparison of the observed curve (solid lines) and the calculated theoretical curves (dash lines) of Line 3 Love wave from the twenty models shown in Figure 35.

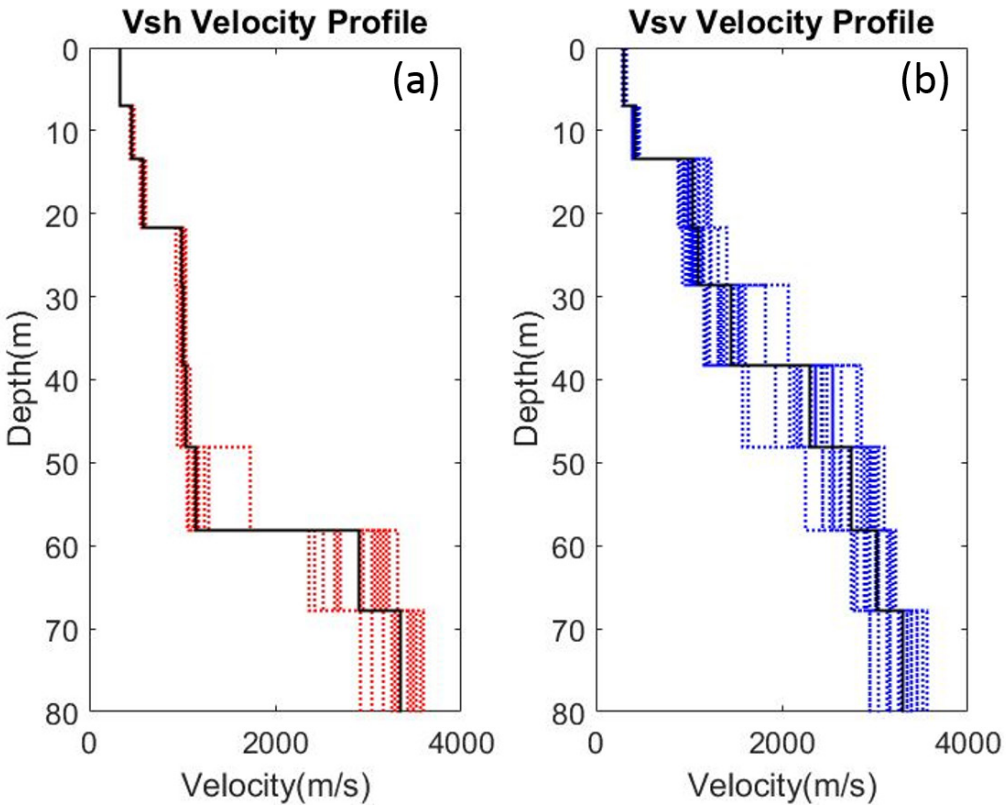

Figure 36. Inversion results of Line 4. The dot lines are all result from 20 different inversions, the solid black line is the weighted average of all the results.

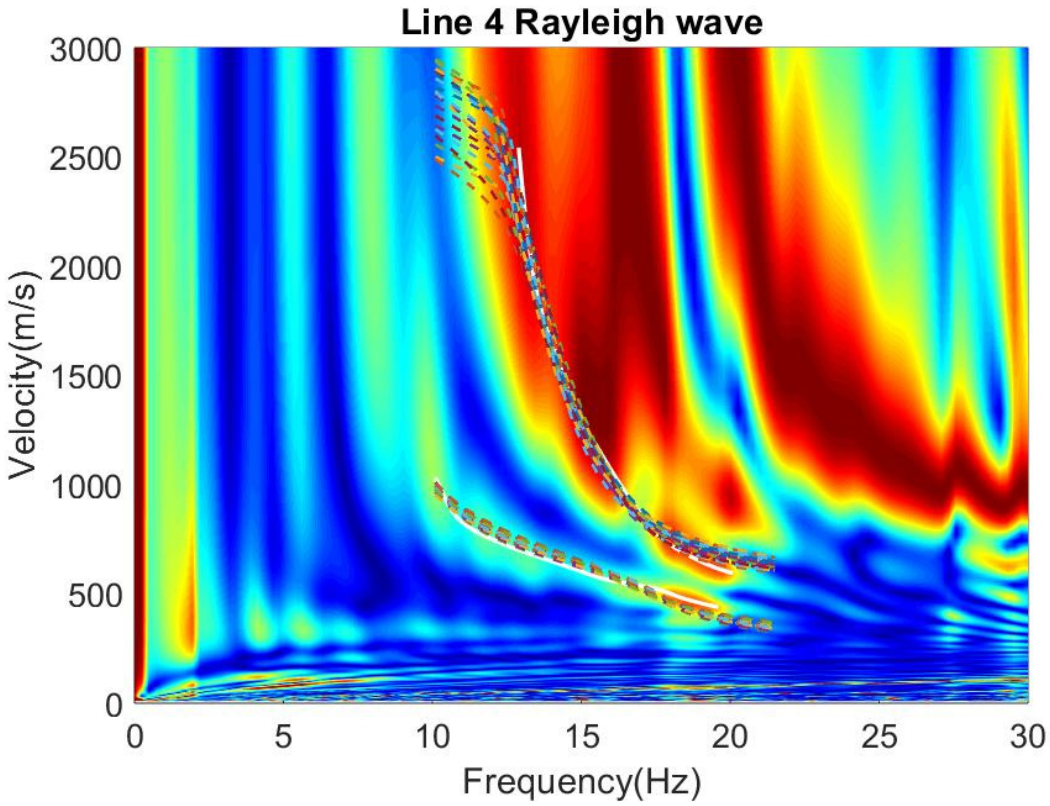

Figure 37. Comparison of the observed curve (solid lines) and the calculated theoretical curves (dash lines) of Line 4 Rayleigh wave from the twenty models shown in Figure 38.

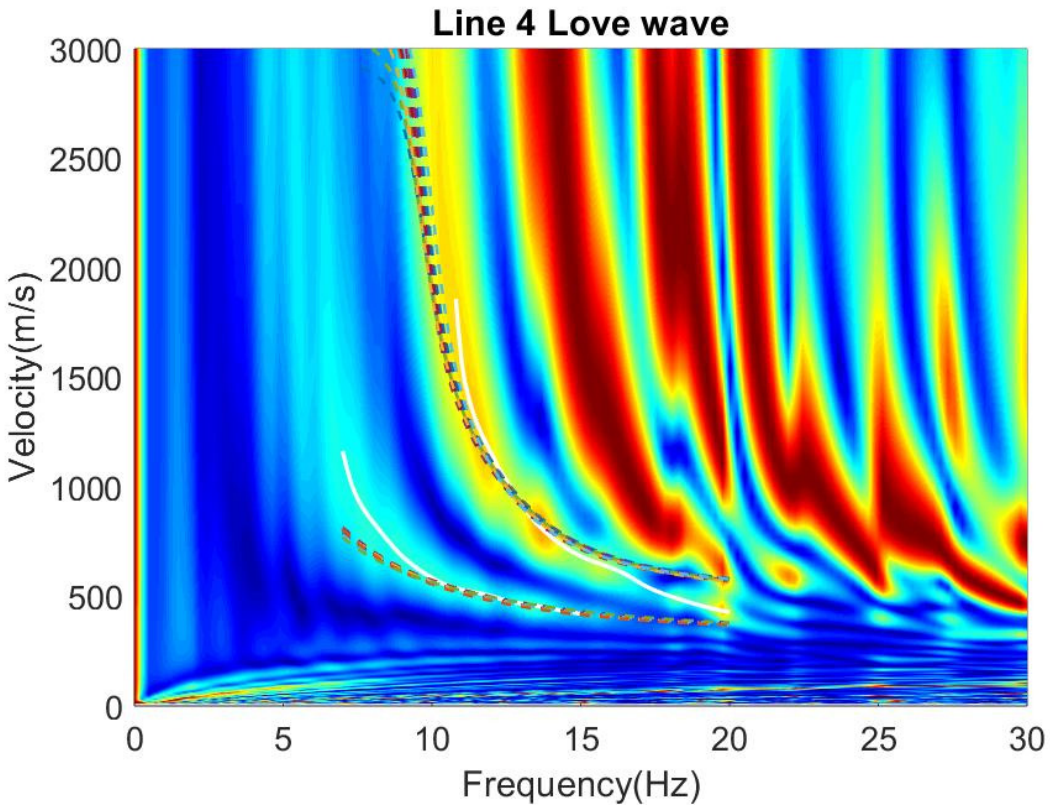

Figure 38. Comparison of the observed curve (solid lines) and the calculated theoretical curves (dash lines) of Line 4 Love wave from the twenty models shown in Figure 38.

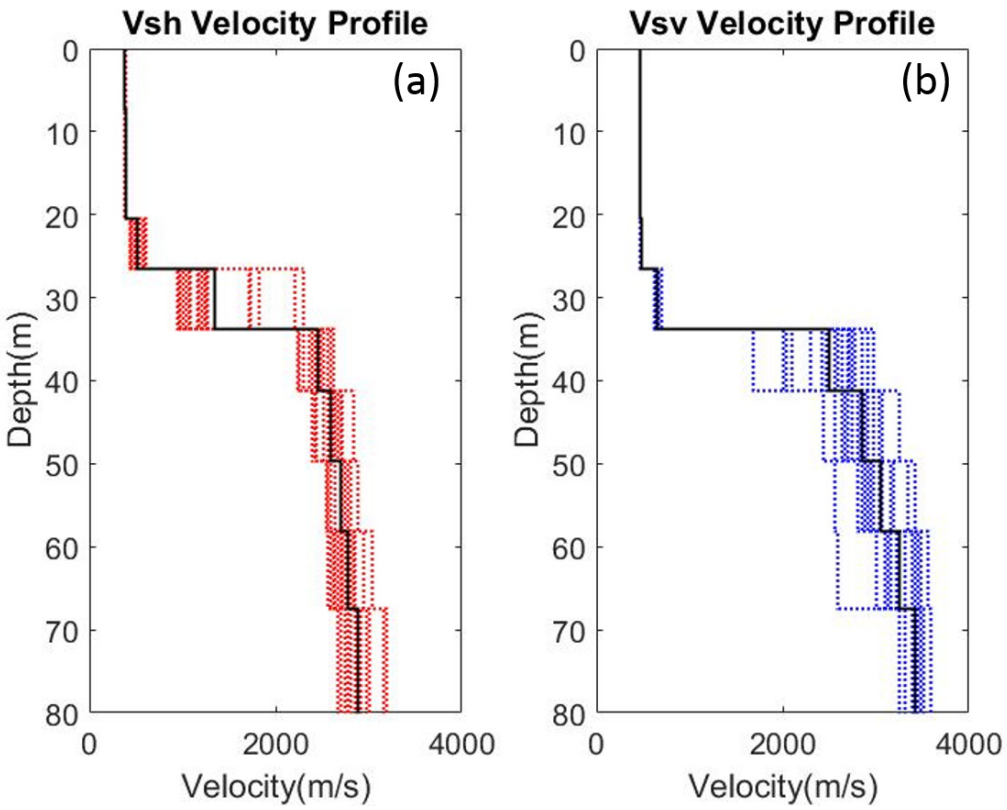

Figure 39. Inversion results of Line 5. The dot lines are all result from 20 different inversions, the solid black line is the weighted average of all the results.

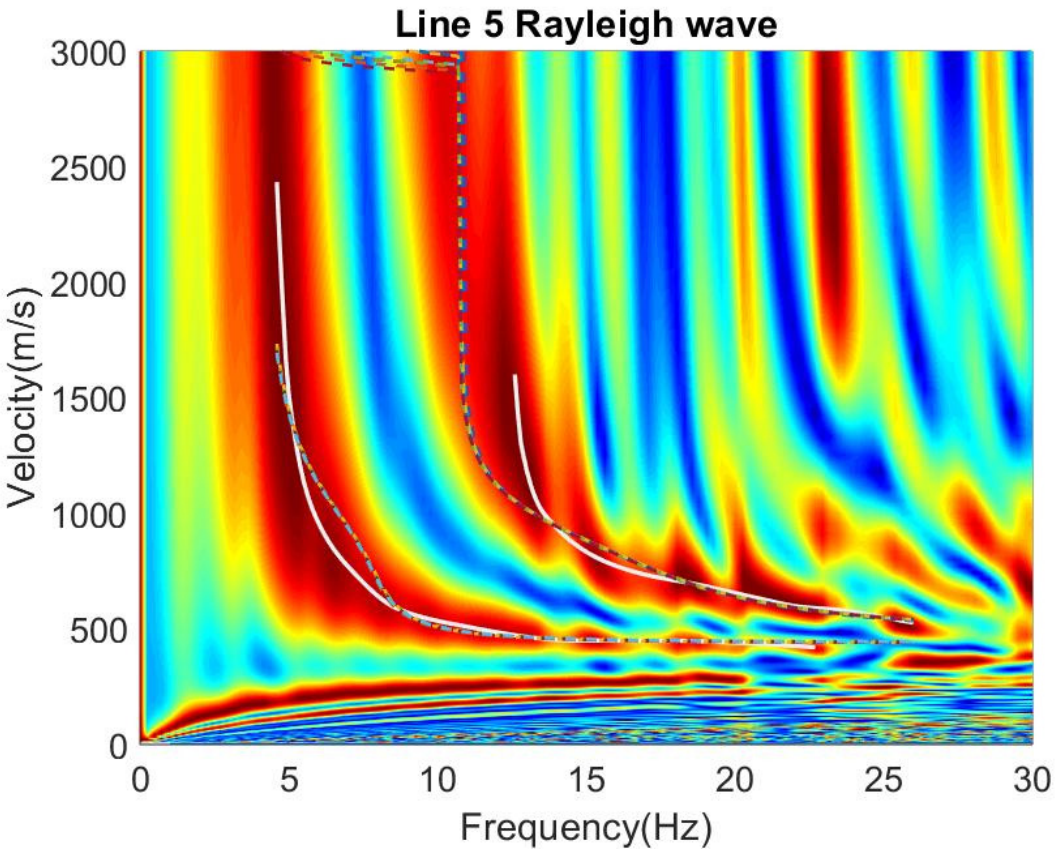

Figure 40. Comparison of the observed curve (solid lines) and the calculated theoretical curves (dash lines) of Line 5 Rayleigh wave from the twenty models shown in Figure 41.

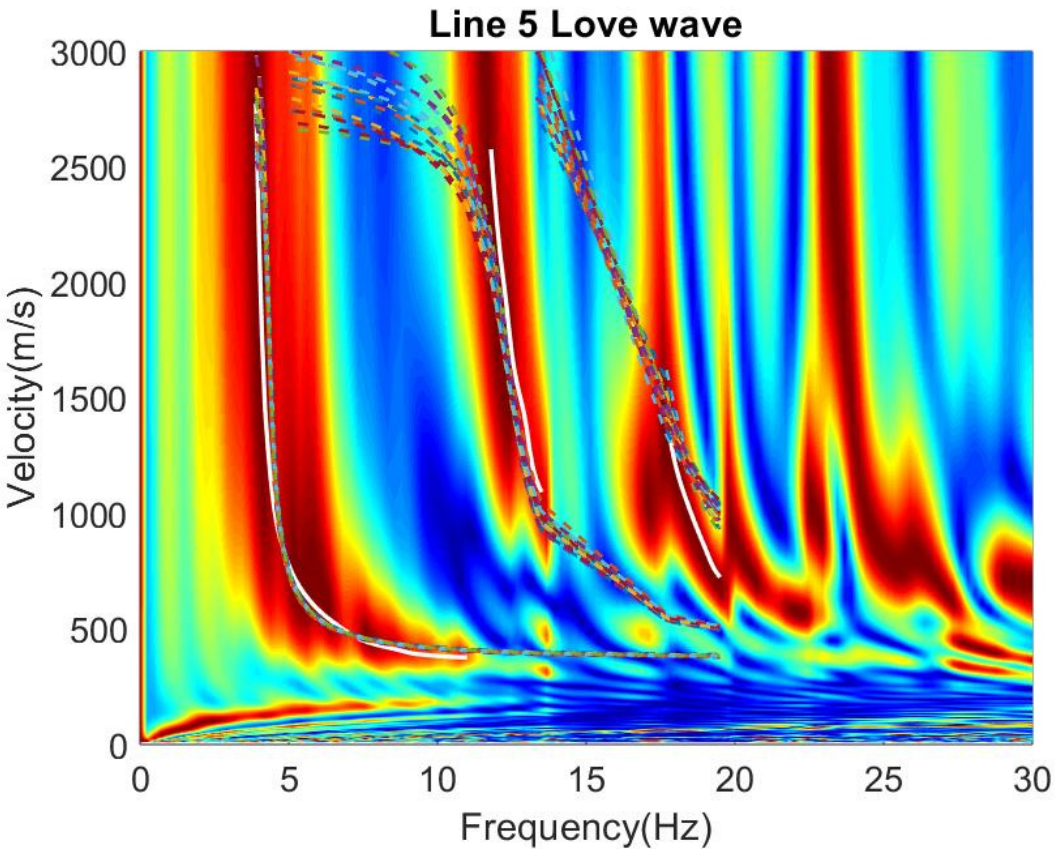

Figure 41. Comparison of the observed curve (solid lines) and the calculated theoretical curves (dash lines) of Line 5 Love wave from the twenty models shown in Figure 41.

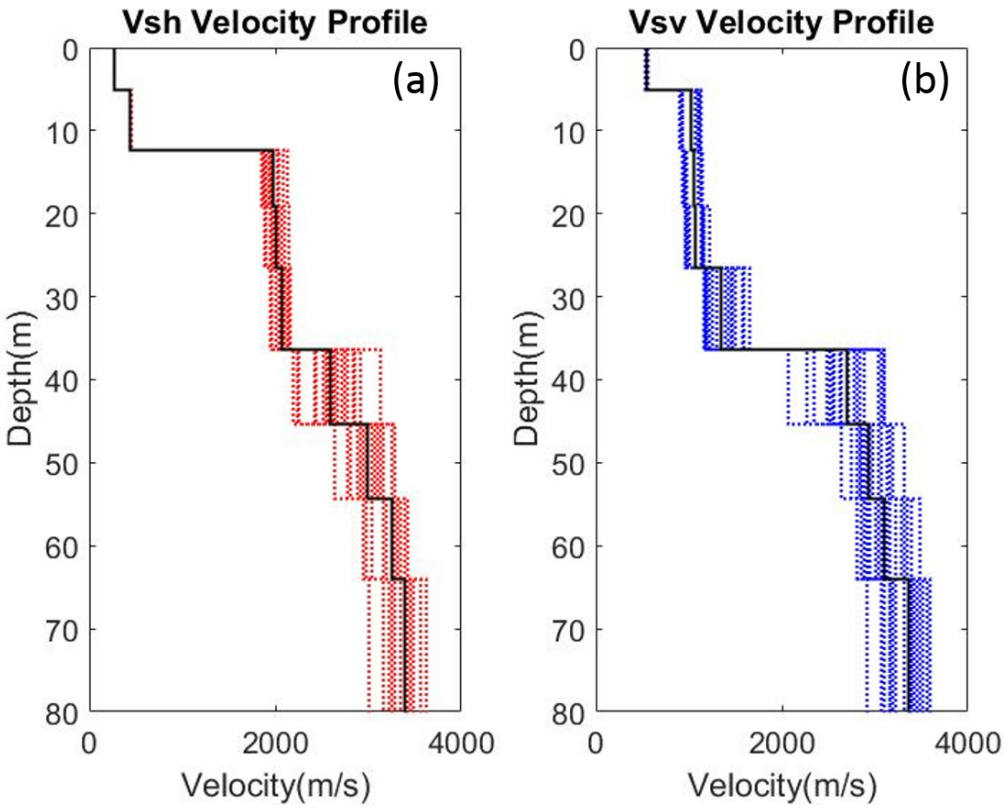

Figure 42. Inversion results of Line 6. The dot lines are all result from 20 different inversions, the solid black line is the weighted average of all the results.

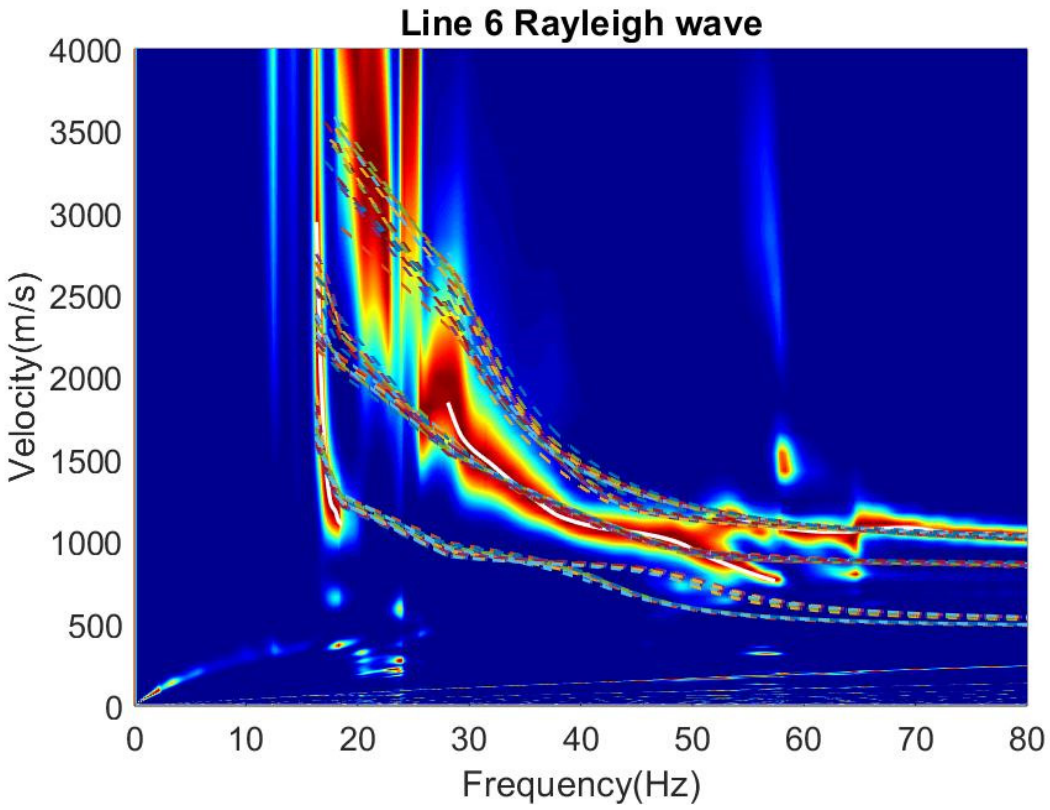

Figure 43. Comparison of the observed curve (solid lines) and the calculated theoretical curves (dash lines) of Line 6 Rayleigh wave from the twenty models shown in Figure 44.

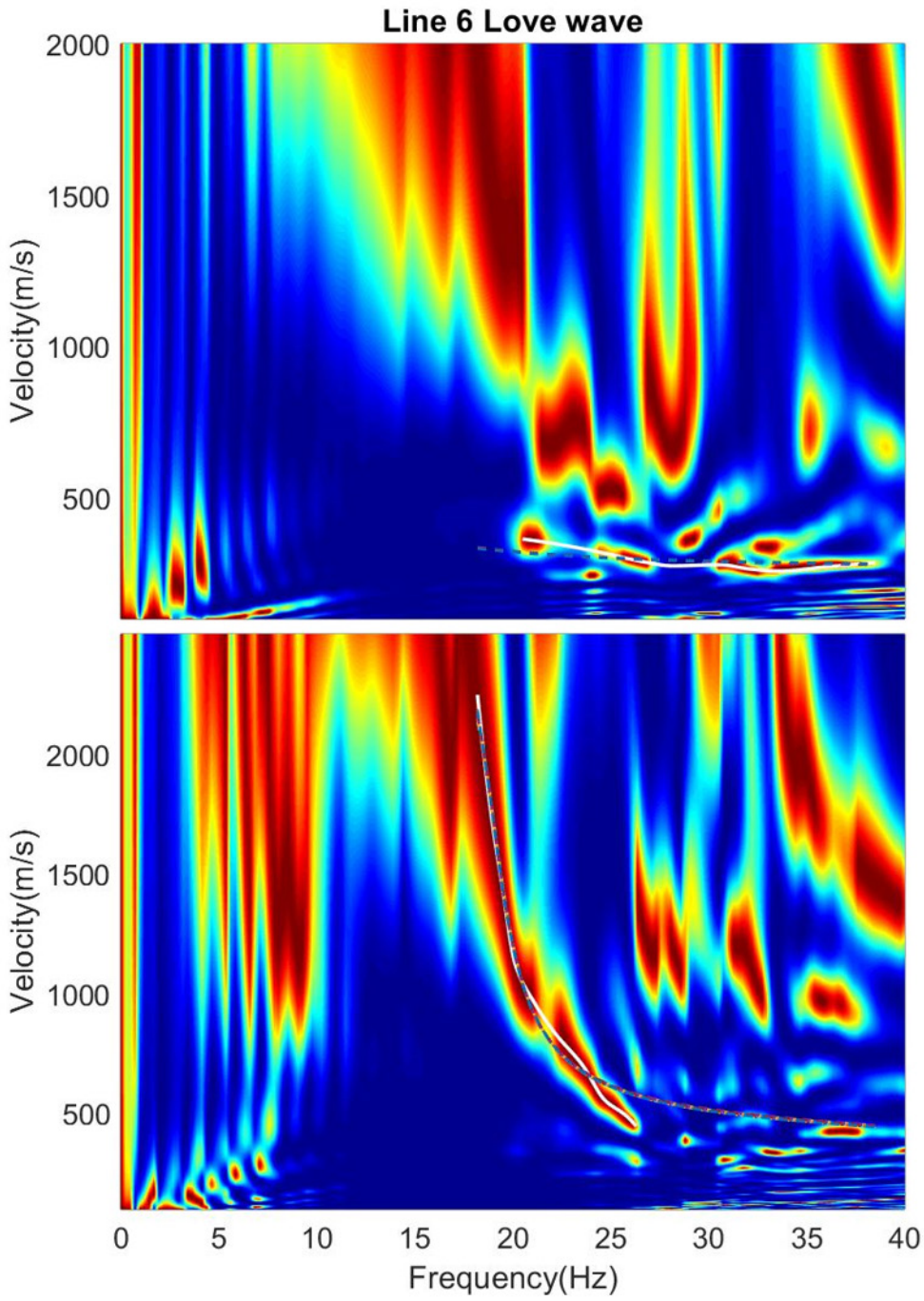

Figure 44. Comparison of the observed curve (solid lines) and the calculated theoretical curves (dash lines) of Line 6 Love wave from the twenty models shown in Figure 44.

8 Results and Discussion

8.1 Radial Anisotropy

After obtaining the V_{SV} and V_{SH} profile inverted from Rayleigh and Love waves, the radical anisotropy parameter ξ was obtained from equation (1). From the previous 20 inversion results of V_{SV} and V_{SH} profiles each, 400 possible radial anisotropy parameter ξ was obtained in each line. For those 400 possible radial anisotropy models, the mean value and 95% confidence interval based on t distribution was calculated and compared with the fracture location from well log data close to each lines (Table 1). From the lab result, Dande et al. (2018) found that a dry fractured model creates about 22% anisotropy in shear wave and fluid substitution does not have a significant effect on S-wave anisotropy. Wei et al. (2018) used different synthetic models of different fracture density and found that for high-density fractured models (> 10%), anisotropy is above 12-18%.

Therefore, 0.2 (20%) as a cutoff value of the radial anisotropy parameter was used to determine a proxy of the fracture presence, which means if the absolute value of the radial anisotropy parameter is greater than 0.2, there will be higher possibility to observe fractures. From the 400 results of radial anisotropy parameter ξ in each line, the probability of fracture existence of each zones was calculated with the cutoff value of 20%.

In the following figures, the subsurface velocity profile, radial anisotropy parameter, fracture location from log data and the probability of fracture presence in each Line were presented (Figure 45-50).

8.1.1 Mirror Lake, New Hampshire

In the Mirror Lake, New Hampshire dataset, the bedrock is highly fractured from 20 - 50 m. As a result, the high values of radial anisotropy are expected from 20-50 m down the hole. It was also noted that high correlation between fracture locations and the radial anisotropy profiles was observed from the wells. However, since the bedrocks in Mirror Lake is mainly formed by schist, which has been observed have contributions on anisotropy and can cause as much as 45% anisotropy (Godfrey et al. 2000), some of the high anisotropy behavior might not be purely caused by fracture but partially be caused by schist.

8.1.1.1 Result of Line 1

Figure 45 shows the result of Line 1. In Figure 45a, the S-wave velocity increases rapidly at the depth around 22 m, which be the boundary between bedrock and the soil layer. Comparison of the radial anisotropy parameter shown in Figure 45b and the fracture location map from well FSE 8 (Figure 45c) shows a strong correlation. Note that at the depth between 50-60 m there is no fracture according to well data, however a strong radial anisotropy was observed for the inversion result. According to Johnson and Dunstan (1998), at this depth, there is a schist layer that is inherently anisotropic due to

foliation. In the probability map (Figure 45d), in the highly fractured area the probability of fracture presence is also high, this matched the prediction with the fracture locations and provided a valid prediction of fractured zones.

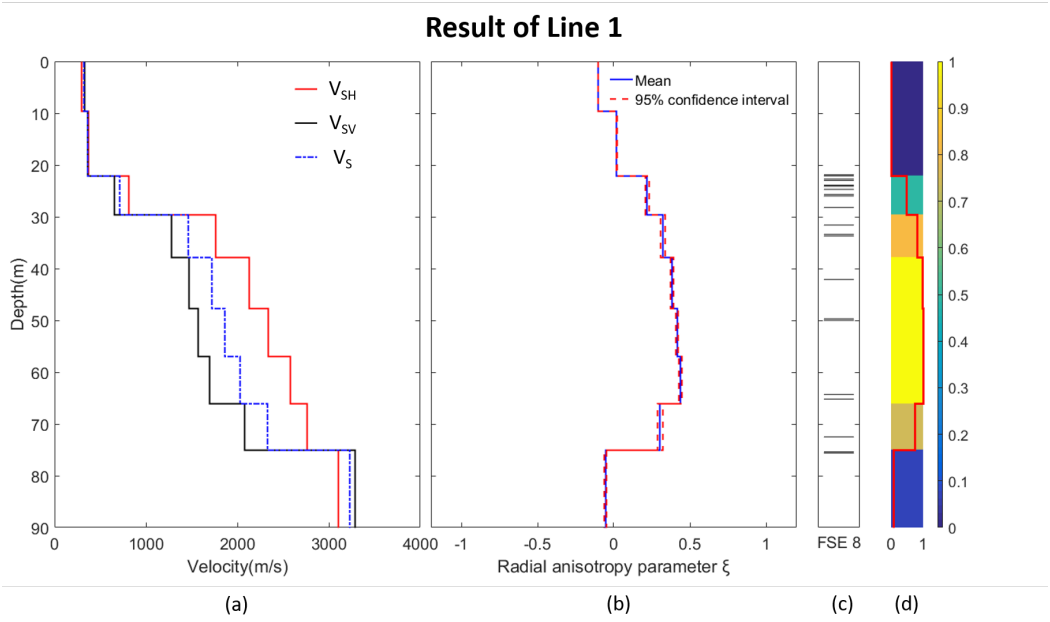

Figure 45. Result of Line 1 includes (a) V_{SV} and V_{SH} profile, (b) Radial anisotropy parameter ξ, (c) fracture location obtained from well FSE 8 and (d) the probability map of fracture presence.

8.1.1.2 Result of Line 2

Figure 46 shows the results of Line 2. From Figure 46a it is noted that the boundary between bedrock and the soil layer is around 22 m. Comparison of the radial anisotropy parameter shown in Figure 46b and the fracture location map from well FSE 11 (Figure 46c) also shows a strong correlation. At the depth between 20 – 30 m, it shown high anisotropy whereas only one fracture was found in the location; but from the geological

report, this zone appeared to be schist layer, high anisotropy could be due to the foliation. The highly fractured area from 35 to 50 m also shown high radial anisotropy.

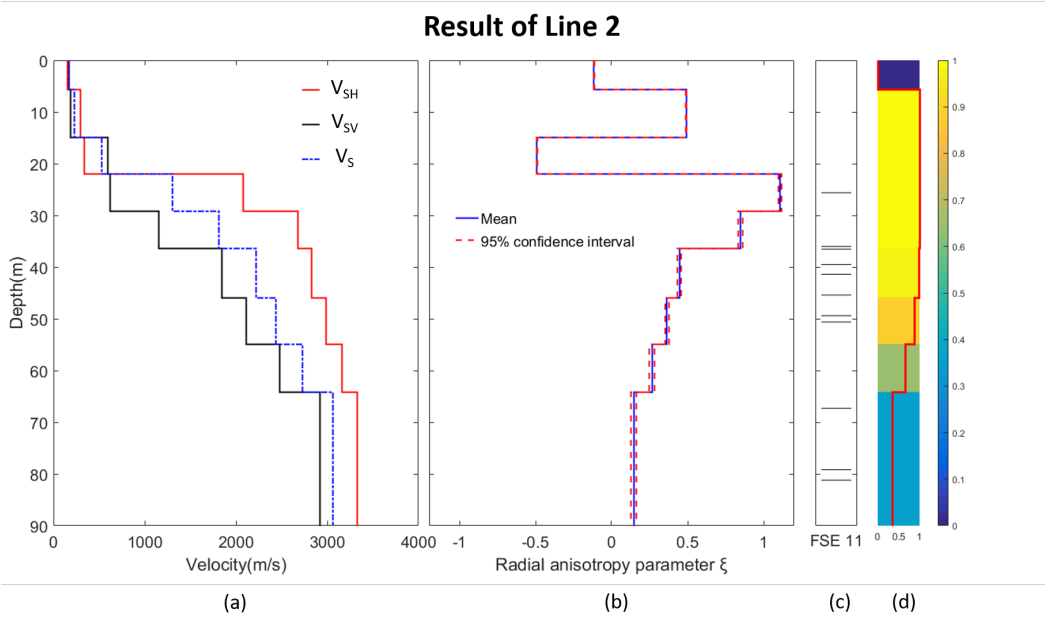

Figure 46. Result of Line 2 includes (a) V_{SV} and V_{SH} profile, (b) Radial anisotropy parameter ξ, (c) fracture location obtained from well FSE 11 and (d) the probability map of fracture presence.

8.1.2 Hannahville Indian Community, Michigan

In the Hannahville Indian Community, Michigan dataset, the seismic data was collected at two separate sites. Line 3 and Line 4 are close to community well 1 and 2; whereas, Line 5 and Line 6 are close to the well, casino 5. From community wells 1 and 2, the highly fractured area is near 40 - 70 m. In this area, high correlation between radial anisotropy and the fracture location was observed. However, there are no fracture

location information of the well Casino 5 is available from the surface to the depth of 88 m.

8.1.2.1 Result of Line 3 and 4

The results of Lines 3 and 4 are shown in Figure 47 and 48, respectively. The results of Line 3 show a high negative radial anisotropy from 7 m (Figure 47b). Since the shorten wavelength are more sensitive to the surface layer (Xia et al. 1999), the dispersion curve obtained from the Line 3 dataset are only limited to low frequencies (<20 Hz). As short wavelengths are not available in this data, the inversion results are valid for the depths above 15 m. Overall the radial anisotropy parameter and the fracture location (Figure 47 c and d) from the two wells in this site are highly correlated. The probability map (Figure 47e) is also shown high correlation with the fracture location.

The results from Line 4 are shown in Figure 48. In this line, after 12 m, V_{SH} and V_{SV} are significantly different (Figure 48a). From 30-60 m, high radial anisotropy (Figure 48b) is notable, which matches the fracture location from the well data (Figure 48 c and d). The fracture probability map (Figure 48e) shows a high correlation with the highly fractured areas.

Overall, these two lines show the same trend: the subsurface velocity are in the same range, negative anisotropy parameter and high anisotropy in highly fractured area.

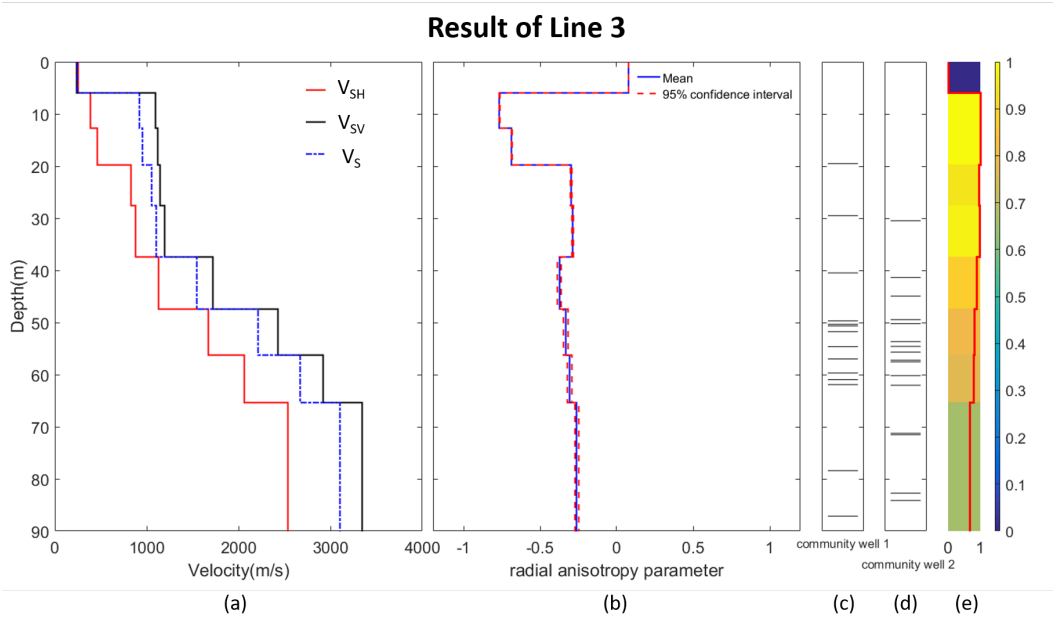

Figure 47. Result of Line 3 includes (a) V_{SV} and V_{SH} profile, (b) Radial anisotropy parameter ξ, (c) fracture location obtained from well community 1, (d) fracture location obtained from well community 2 and (e) the probability map of fracture presence.

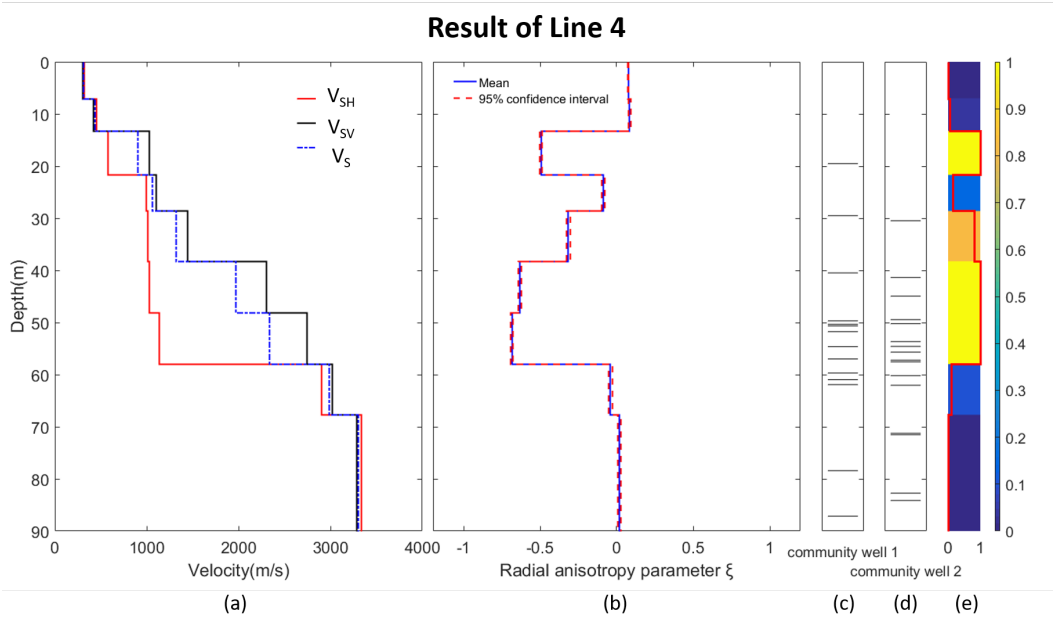

Figure 48. Result of Line 4 includes (a) V_{SV} and V_{SH} profile, (b) Radial anisotropy parameter ξ, (c) fracture location obtained from well community 1, (d) fracture location obtained from well community 2 and (e) the probability map of fracture presence.

8.1.2.2 Result of Line 5 and 6

The results of Line 5 and Line 6 are shown in Figure 49 and 50 respectively. Lines 5 and 6 were close to well Casino 5, however, in well Casino 5 there is no fracture location information from the surface until the depth of 88 m. In the inversion result, an eight-layer model up to 80 m is obtained. For Line 5, a high positive radial anisotropy from 26-33 m is observed (Figure 49b). The probability map also shows high probability in this zone (Figure 49d). For Line 6, from 12-34 m, radial anisotropy is high and positive (Figure 50b), the probability map also indicates that this zone might be highly fractured.

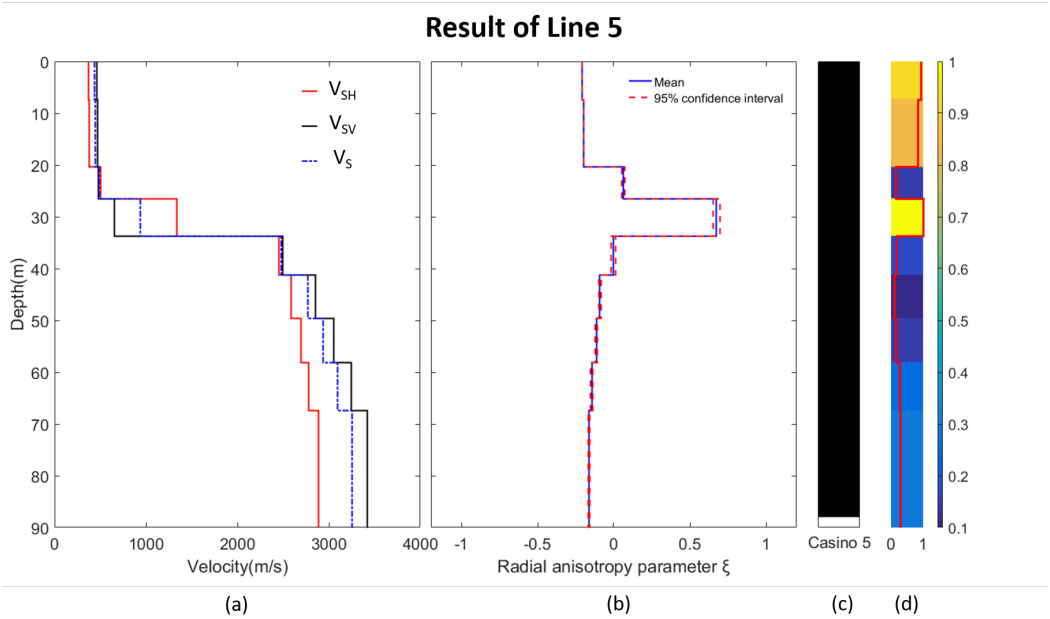

Figure 49. Result of Line 5 includes (a) V_{SV} and V_{SH} profile, (b) Radial anisotropy parameter ξ, (c) fracture location obtained from well Casino 5 and (d) the probability map of fracture presence

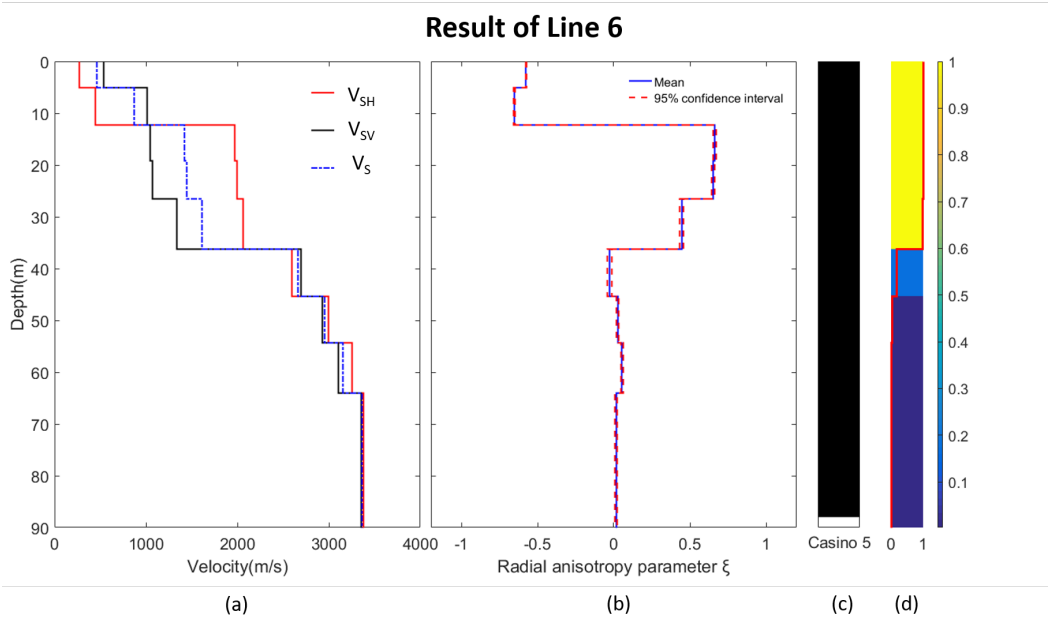

Figure 50. Result of Line 6 includes (a) V_{SV} and V_{SH} profile, (b) Radial anisotropy parameter ξ, (c) fracture location obtained from well Casino 5 and (d) the probability map of fracture presence

8.2 Sensitivity analysis

To better predict the fracture probability and understand a proper cutoff value of radial anisotropy parameter. A sensitivity analysis is performed to present how the probability change when choosing different cutoff values since in different geological setting, the cutoff value for predicting the probability of fracture presence can be different due to the material elastic property. Dande et al. (2018) observed that the anisotropy is about 4% for the solid model, therefore, for the sensitivity analysis a sensitivity test of cutoff value was conducted from 0.05 to 0.6 with an increment of 0.05. The results are shown in Figure 51-56.

In the Mirror Lake, New Hampshire, the results of Line 1 (Figure 51) indicated that from 22 to 74 m, the probability of fracture presence are high with any cutoff value less than 0.45, which matched the fracture location from the well data. When the cutoff value is 0.45 or more the probability of fracture is less than 50% at all locations within the Line 1.

The result of Line 2 (Figure 52) shown that in the highly fractured area (35 - 52 m) also have the high probability of fracture occurrence, which was highly fractured from the well data. Noted when cutoff value is 0.45 and more the probability of fracture is less than 50% at most of the locations within Line 2.

The result of Hannahville Indian Community, Michigan dataset are shown in Figure 53-56. The fracture location data from community well 1 and 2 shows that from 40-65 m are highly fractured. The probability result from Line 3 (Figure 53) and Line 4 (Figure 54) also suggest the same. The cutoff range from 0.15-0.4 in this area could provide valid prediction of the fracture probability.

For the result of Line 5 and Line 6 (Figure 55 & 56), since the fracture location is not available until 88 m, it is unable to compare the result. However, from both datasets it shown that from 20-35m the probability of fracture occurrence is high, and the result are consistent with different cutoff values.

From the sensitivity analysis, cutoff value from 0.15 to 0.3 seems to be appropriate value to calculate the fracture probabilities for the Mirror Lake dataset. For the Hannahville Indian Community dataset, the probabilities calculated from cutoff value 0.15 to 0.4 matched the fracture locations from the well data near the lines.

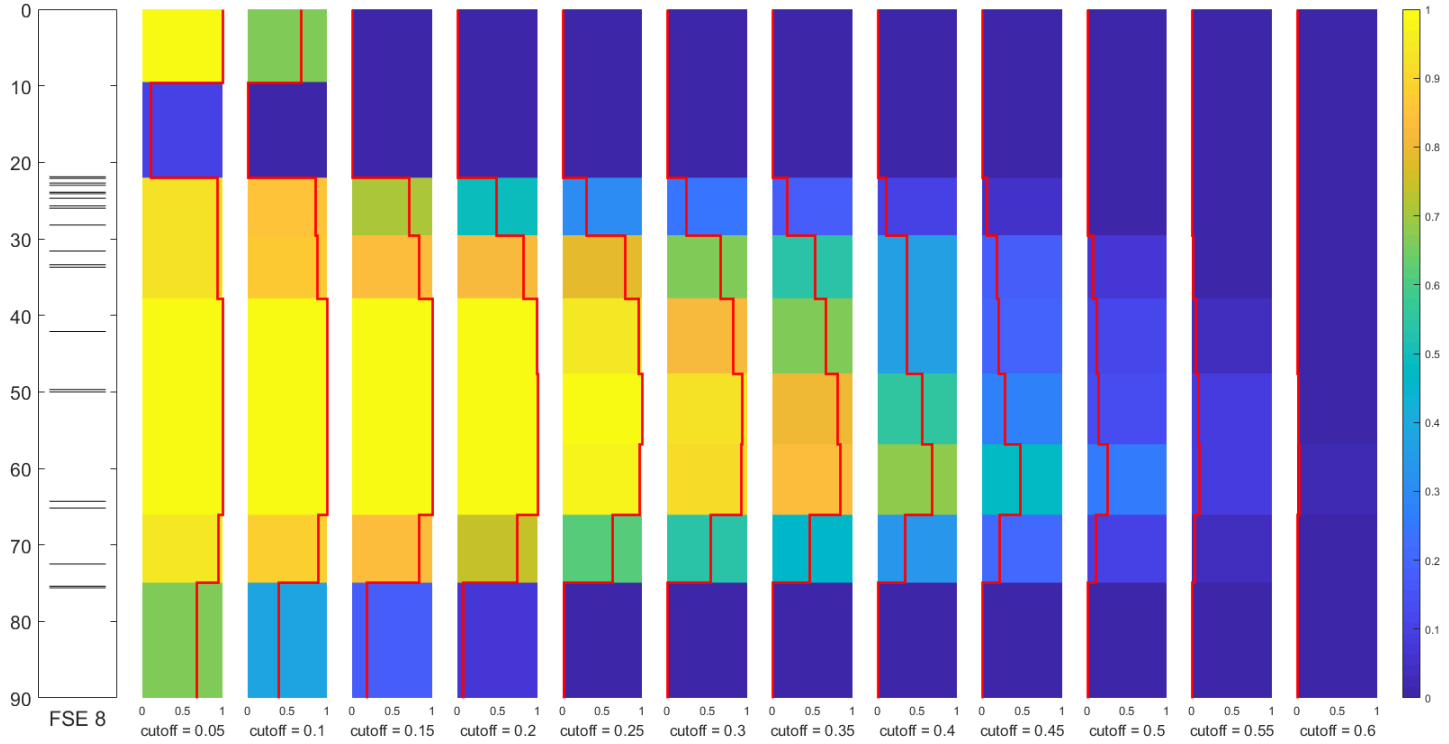

Figure 51. Probability of fracture occurrence with different cutoff values of Line 1

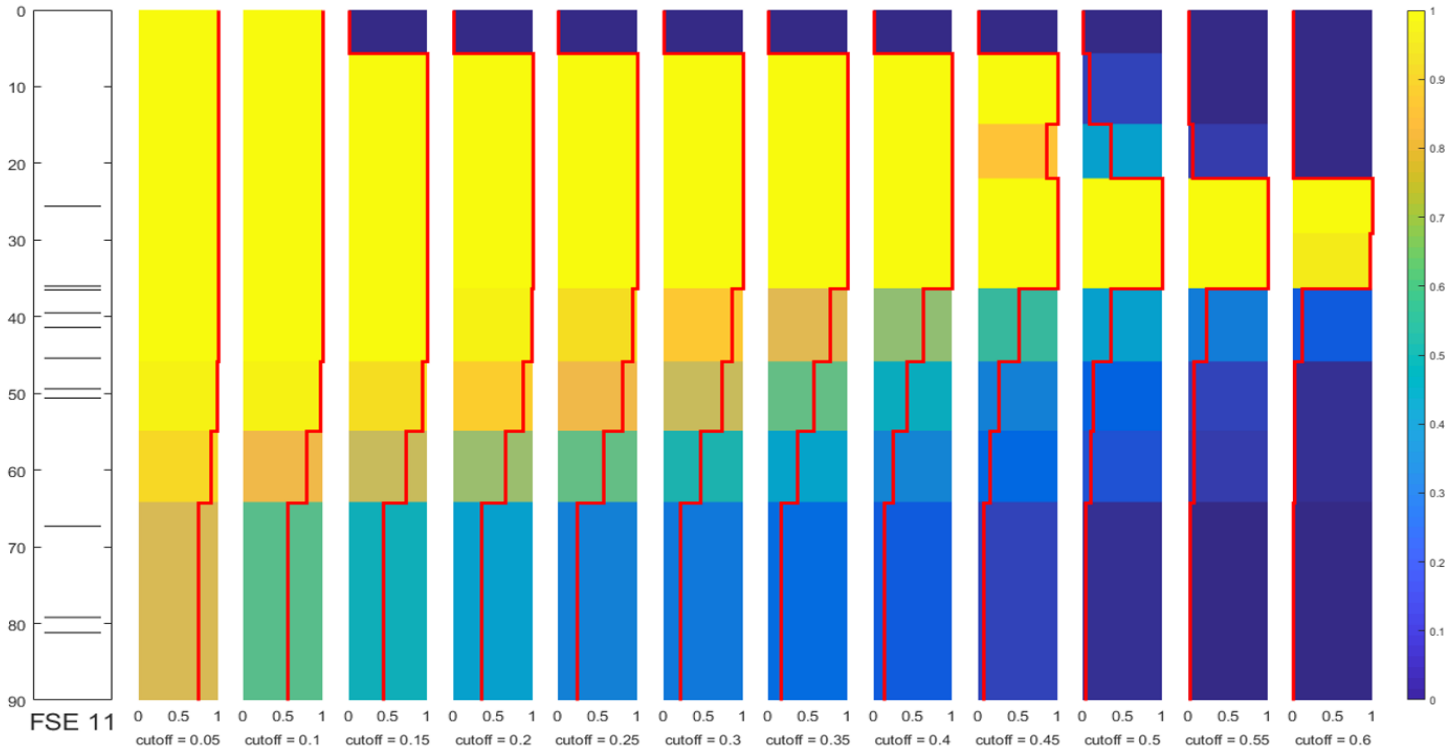

Figure 52. Probability of fracture occurrence with different cutoff values of Line 2

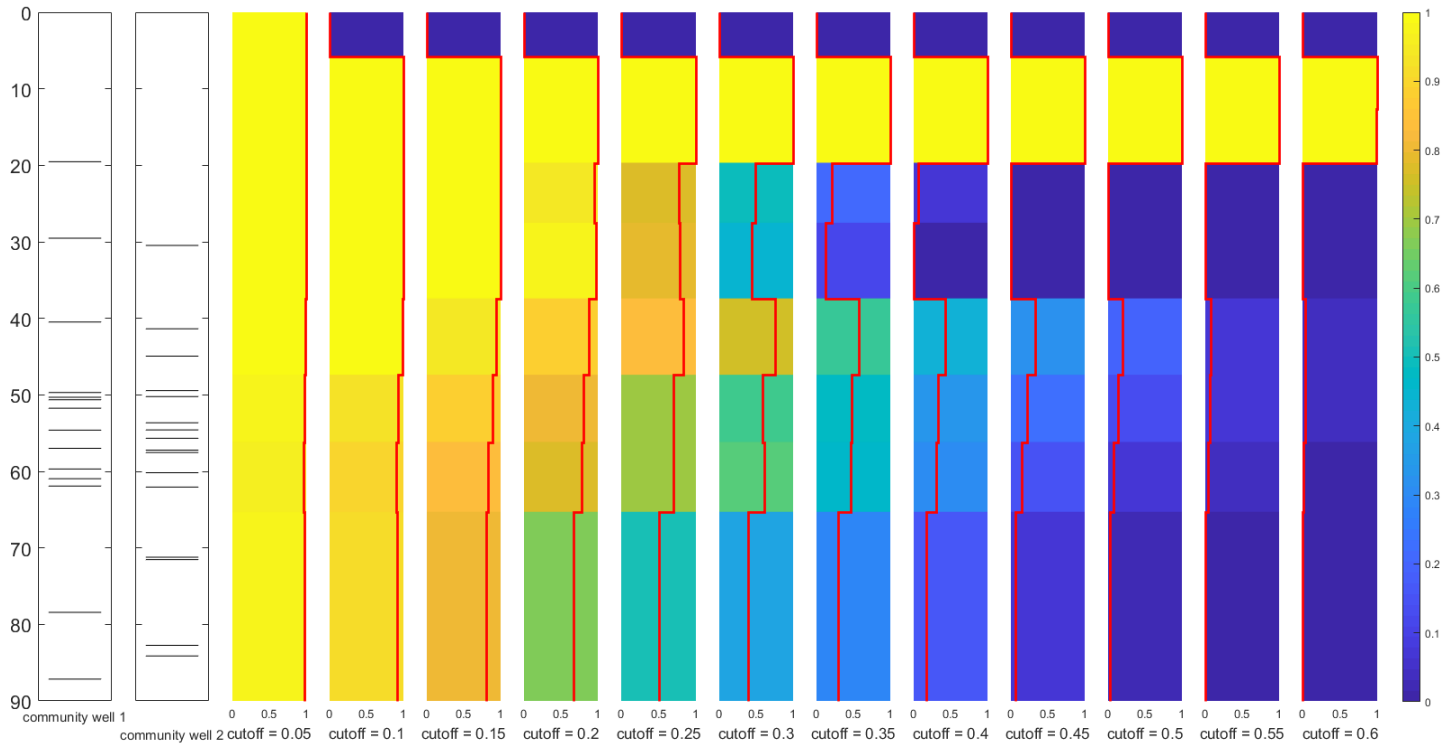

Figure 53. Probability of fracture occurrence with different cutoff values of Line 3

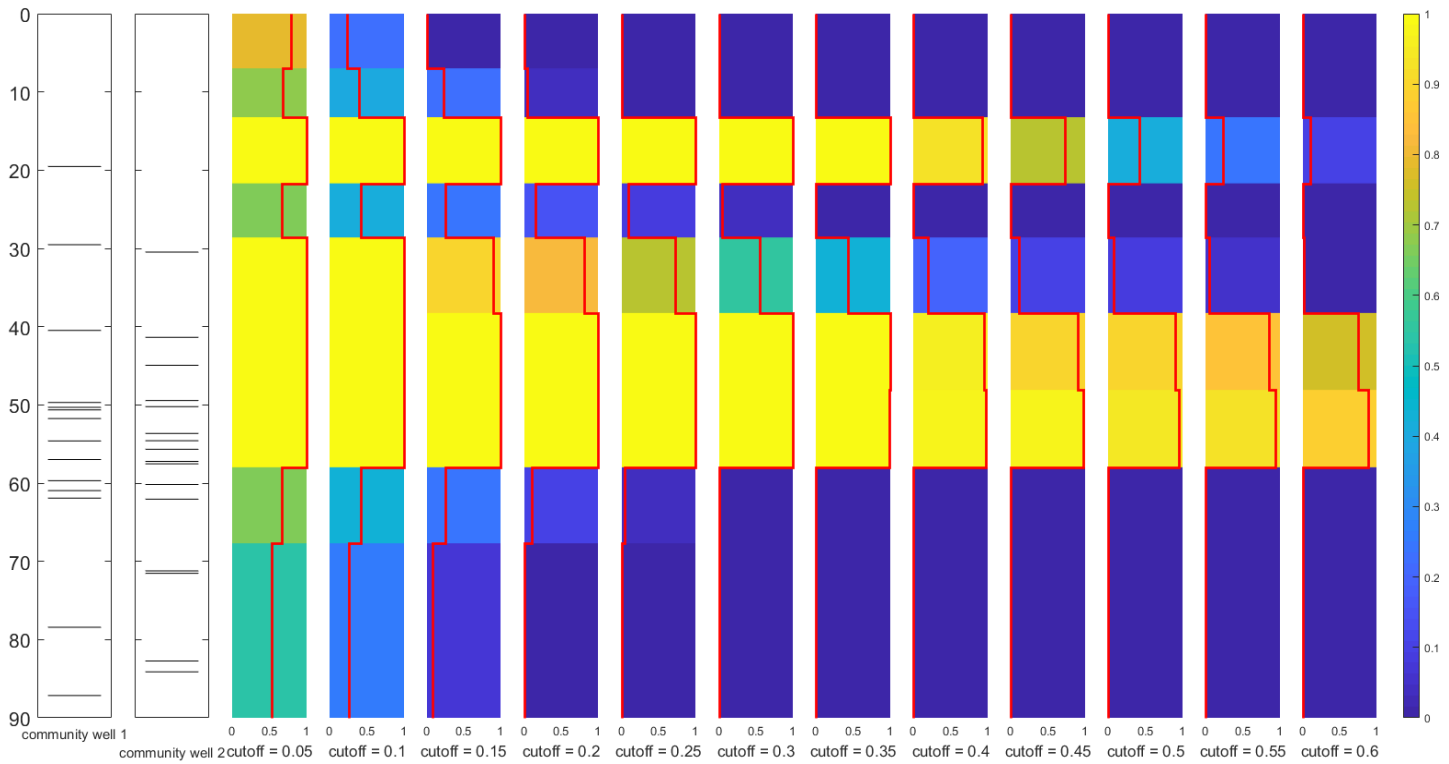

Figure 54. Probability of fracture occurrence with different cutoff values of Line 4

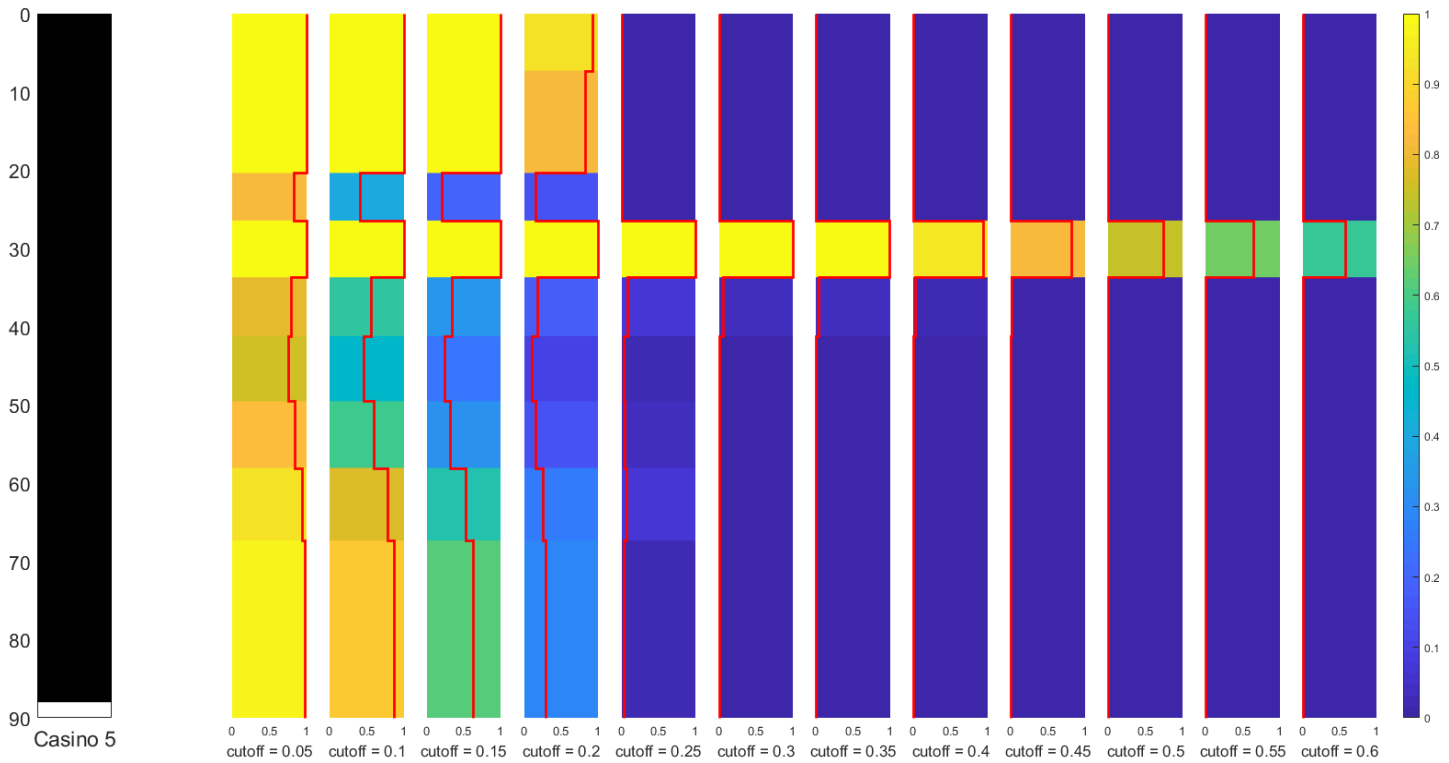

Figure 55. Probability of fracture occurrence with different cutoff values of Line 5

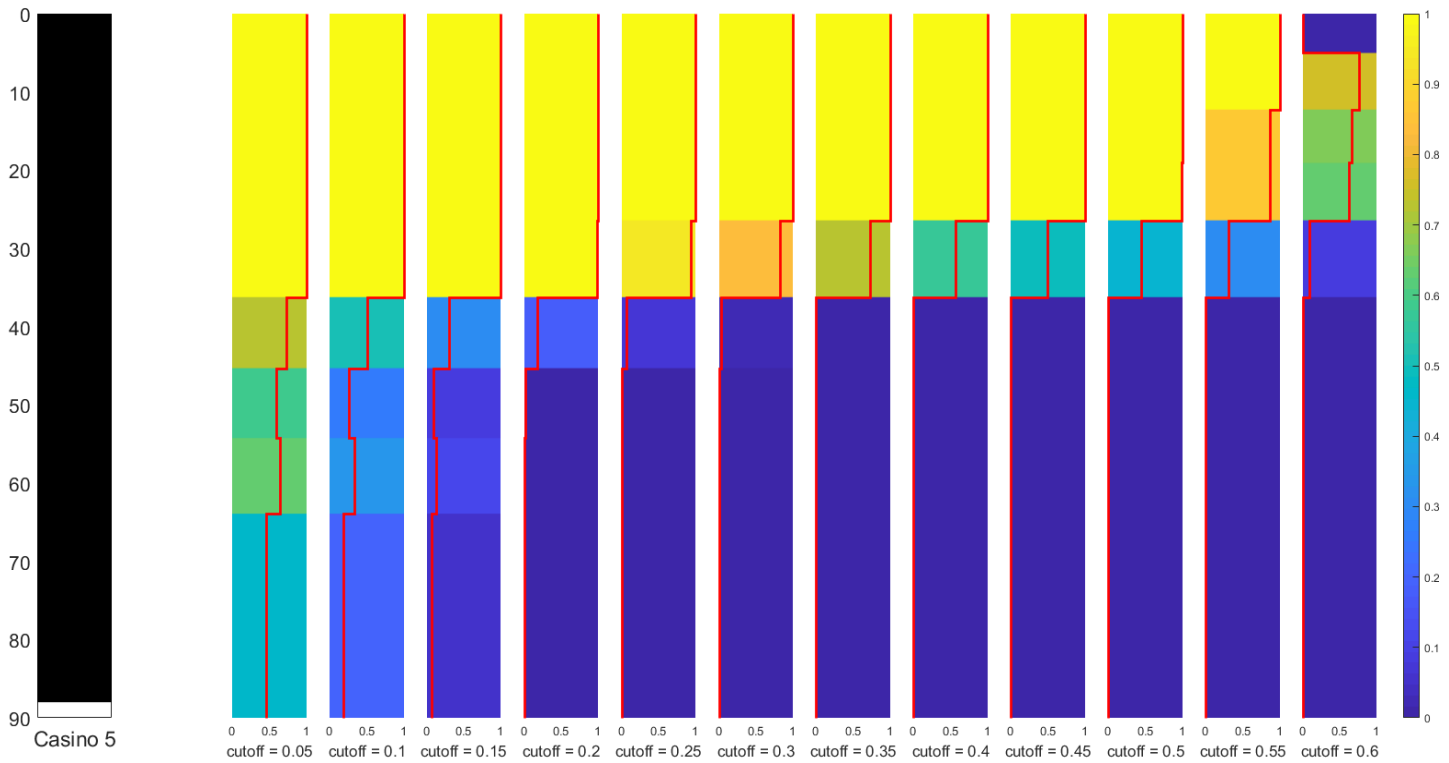

Figure 56. Probability of fracture occurrence with different cutoff values of Line 6

9 Conclusion

In this research, from the field data acquired in two locations with different geological settings, high correlations between near-surface fractures and radial anisotropy are notable. These findings suggest that radial anisotropy has a potential to be used as a strong attribute for the near-surface fracture identification.

From the processing and inversion aspects of the data, it was noted that in an area with highly heterogeneous bedrock, applying different windowing is useful to identify different dispersion modes. It is possible to obtain the S-wave velocity models of deeper zones by combining the higher modes into the joint inversion. Different cutoff values of radial anisotropy parameter can be used to obtain a better understanding of fracture density and better prediction of highly fractured zones. It was also noted that different material might have different elastic properties; therefore, more field and lab tests should be conducted in the future to better correlate fracture and the radial anisotropy.

10 Reference List

Adler, P. M., and J. F. Thovert. 1999, Fractures and fracture networks. Vol. 15: Springer Science & Business Media.

Aki, K. 1963, Phase velocity of Love waves in Japan, 1, 1, Love waves from the Aleutian shock of March 9, 1957. Bull. Earthq. Res. Inst. Univ. Tokyo, **41**,243-259.

Aki, K., and P. G. Richards. 1980, Quantitative Seismology, Vol. 2. WH Freeman San Francisco.

Anderson, D. L. 1961, Elastic wave propagation in layered anisotropic media. Journal of Geophysical Research, **66**, no. 9,2953-2963.

Armstrong, F. C., and E. L. Boudette. 1984, Two-mica granites; Part A, Their occurrence and petrography. US Geological Survey.

Askari, R., and R. J. Ferguson. 2012, Dispersion and the dissipative characteristics of surface waves in the generalized S-transform domainDispersion and dissipation of surface waves. Geophysics, **77**, no. 1,V11-V20.

Askari, R., and S. H. Hejazi. 2015, Estimation of surface-wave group velocity using slant stack in the generalized S-transform domainSurface-wave group velocity estimation. Geophysics, **80**, no. 4,EN83-EN92.

Askari, R., and H. R. Siahkoohi. 2008, Ground roll attenuation using the S and xfk transforms. Geophysical Prospecting, **56**, no. 1,105-114.

Aydin, A. 2000, Fractures, faults, and hydrocarbon entrapment, migration and flow. Marine and petroleum geology, **17**, no. 7,797-814.

Bates, C. R., and D. R. Phillips. 2000, Multi-component seismic surveying for near surface investigations: examples from central Wyoming and southern England. Journal of Applied Geophysics, **44**, no. 2-3,257-273.

Bayless, E. R., J. A. Anderson, D. C. Lampe, and J. H. Williams. 2013, Geophysical-Log and Hydraulic-Test Analyses of Groundwater-Production Wells at the Hannahville Indian Community, Menominee County, Michigan. US Geological Survey.

Beaty, K. S., D. R. Schmitt, and M. Sacchi. 2002, Simulated annealing inversion of multimode Rayleigh wave dispersion curves for geological structure. Geophysical Journal International, **151**, no. 2,622-631.

Becker, T. W., B. Kustowski, and G. Ekström. 2008, Radial seismic anisotropy as a constraint for upper mantle rheology. Earth and Planetary Science Letters, **267**, no. 1-2,213-227.

Castaing, C., A. Genter, B. Bourgine, J. P. Chilès, J. Wendling, and P. Siegel. 2002, Taking into account the complexity of natural fracture systems in reservoir single-phase flow modelling. Journal of hydrology, **266**, no. 1-2,83-98.

Casto, D. W., C. Calderón-Macías, B. Luke, and R. Kaufmann. 2010, Improving MASW results for a site with shallow bedrock through the use of higher-mode data, GeoFlorida 2010: Advances in Analysis, Modeling & Design. 1360-1368.

Casto, D. W., B. Luke, C. Calderón-Macías, and R. Kaufmann. 2009, Interpreting surface-wave data for a site with shallow bedrock. Journal of Environmental & Engineering Geophysics, **14**, no. 3,115-127.

Christensen, N. I., and S. M. Lundquist. 1982, Pyroxene orientation within the upper mantle. Geological Society of America Bulletin, **93**, no. 4,279-288.

Crampin, S., R. McGonigle, and D. Bamford. 1980, Estimating crack parameters from observations of P-wave velocity anisotropy. Geophysics, **45**, no. 3,345-360.

Dal Moro, G., and F. Ferigo. 2011, Joint analysis of Rayleigh-and Love-wave dispersion: Issues, criteria and improvements. Journal of Applied Geophysics, **75**, no. 3,573-589.

Dande, S., R. R. Stewart, and N. Dyaur. 2018, The effect of fluids and their viscosity on the elastic-wave velocity and anisotropy of 3D-printed VTI rock models, SEG Technical Program Expanded Abstracts 2018: Society of Exploration Geophysicists. 347-350.

Daniels, D. J. 2004, Ground penetrating radar. Vol. 1: Iet.

Day-Lewis, F. D., J. W. Lane, and S. M. Gorelick. 2006, Combined interpretation of radar, hydraulic, and tracer data from a fractured-rock aquifer near Mirror Lake, New Hampshire, USA. Hydrogeology Journal, **14**, no. 1-2,1-14.

DeVault, B., T. L. Davis, I. Tsvankin, R. Verm, and F. Hilterman. 2002, Multicomponent AVO analysis, vacuum field, New Mexico. Geophysics, **67**, no. 3,701-710.

Dokht Dolatabadi Esfahani, R., R. Askari, and A. Gholami. 2018, Sparsity promoting method to estimate the dispersion curve of surface wave group velocity. GEOPHYSICS,1-40. doi: 10.1190/geo2018-0138.1.

Dolatabadi, R., A. Gholami, and R. Askari. 2017, Using sparse S transform and sparse-slant stacking for the estimation of the group velocity of surface waves, SEG

Technical Program Expanded Abstracts 2017: Society of Exploration Geophysicists. 2732-2736.

Dorn, C., N. Linde, J. Doetsch, T. Le Borgne, and O. Bour. 2012, Fracture imaging within a granitic rock aquifer using multiple-offset single-hole and cross-hole GPR reflection data. Journal of applied geophysics, **78**,123-132.

Dziewonski, A. M., and D. L. Anderson. 1981, Preliminary reference Earth model. Physics of the earth and planetary interiors, **25**, no. 4,297-356.

Ekström, G., and A. M. Dziewonski. 1998, The unique anisotropy of the Pacific upper mantle. Nature, **394**, no. 6689,168.

Ellefsen, K. J., P. A. Hsieh, and A. M. Shapiro. 2002, Crosswell seismic investigation of hydraulically conductive, fractured bedrock near Mirror Lake, New Hampshire. Journal of Applied Geophysics, **50**, no. 3,299-317.

Elmo, D., and D. Stead. 2010, An integrated numerical modelling–discrete fracture network approach applied to the characterisation of rock mass strength of naturally fractured pillars. Rock Mechanics and Rock Engineering, **43**, no. 1,3-19.

Faybishenko, B., C. Doughty, M. Steiger, J. C. S. Long, T. R. Wood, J. S. Jacobsen, J. Lore, and P. T. Zawislanski. 2000, Conceptual model of the geometry and physics of water flow in a fractured basalt vadose zone. Water resources research, **36**, no. 12,3499-3520.

Gale, J. F. W., R. M. Reed, and J. Holder. 2007, Natural fractures in the Barnett Shale and their importance for hydraulic fracture treatments. AAPG bulletin, **91**, no. 4,603-622.

Ganerød, G. V., J. S. Rønning, E. Dalsegg, H. Elvebakk, K. Holmøy, B. Nilsen, and A. Braathen. 2006, Comparison of geophysical methods for sub-surface mapping of faults and fracture zones in a section of the Viggja road tunnel, Norway. Bulletin of Engineering Geology and the Environment, **65**, no. 3,231.

Gao, L., Y. Pan, J. Xia, T. Bohlen, and G. Tian. 2017, Feasibility of Detecting Groundwater Flow via Analyzing Radial Anisotropy Estimated by Surface Waves, 2017.

Gao, L., J. Xia, Y. Pan, and Y. Xu. 2016, Reason and condition for mode kissing in MASW method. Pure and Applied Geophysics, **173**, no. 5,1627-1638.

Gei, D., L. Eisner, and P. Suhadolc. 2011, Feasibility of estimating vertical transverse isotropy from microseismic data recorded by surface monitoring arrays. Geophysics, **76**, no. 6,WC117-WC126.

Godfrey, N. J., N. I. Christensen, and D. A. Okaya. 2000, Anisotropy of schists: Contribution of crustal anisotropy to active source seismic experiments and shear wave splitting observations. Journal of Geophysical Research: Solid Earth, **105**, no. B12,27991-28007.

Goldberg, D. E., J. C. F. Telles, and L. C. Wrobel. 1989, Genetic Algorithms in Search, Optimization, and Machine Learning, Addison–Veslay Publishing Company. Inc., New York.

Gupta, M., K. Spikes, and B. Hardage. 2016, Characterization of naturally fractured Arbuckle Group in the Wellington Field, Kansas, using S-wave amplitude variation with offset. Interpretation, **5**, no. 1,T49-T63.

Hall, S. A., and J. M. Kendall. 2003, Fracture characterization at Valhall: Application of P-wave amplitude variation with offset and azimuth (AVOA) analysis to a 3D ocean-bottom data setFracture Characterization Using P-Wave AVOA. Geophysics, **68**, no. 4,1150-1160.

Haneberg, W. C., P. S. Mozley, J. C. Moore, and L. B. Goodwin. 1999, Faults and subsurface fluid flow in the shallow crust. Washington DC American Geophysical Union Geophysical Monograph Series, **113**.

Heath, R. C. 1983, Basic ground-water hydrology. Vol. 2220: US Geological Survey.

Herrmann, R. B. 1973, Some aspects of band-pass filtering of surface waves. Bulletin of the Seismological Society of America, **63**, no. 2,663-671.

Holschneider, M., M. S. Diallo, M. Kulesh, M. Ohrnberger, E. Lück, and F. Scherbaum. 2005, Characterization of dispersive surface waves using continuous wavelet transforms. Geophysical Journal International, **163**, no. 2,463-478.

Hornby, B. E., J. M. Howie, and D. W. Ince. 2003, Anisotropy correction for deviated-well sonic logs: Application to seismic well tie. Geophysics, **68**, no. 2,464-471.

Jaxybulatov, K., N. M. Shapiro, I. Koulakov, A. Mordret, M. Landès, and C. Sens-Schönfelder. 2014, A large magmatic sill complex beneath the Toba caldera. science, **346**, no. 6209,617-619.

Johnson, C. D., and A. H. Dunstan. 1998, Lithology and fracture characterization from drilling investigations in the Mirror Lake area, Grafton County, New Hampshire. US Dept. of the Interior, US Geological Survey; Branch of Information Services [distributor].

Khaheshi Banab, K., and D. Motazedian. 2010, On the efficiency of the multi-channel analysis of surface wave method for shallow and semi-deep loose soil layers. International Journal of Geophysics, **2010**.

Kulesh, M., M. Holschneider, M. S. Diallo, Q. Xie, and F. Scherbaum. 2005, Modeling of wave dispersion using continuous wavelet transforms. Pure and Applied Geophysics, **162**, no. 5,843-855.

Laubach, S., R. Marrett, and J. Olson. 2000, New directions in fracture characterization. The Leading Edge, **19**, no. 7,704-711.

Li, X.-Y. 1997, Fractured reservoir delineation using multicomponent seismic data. Geophysical Prospecting, **45**, no. 1,39-64. doi: 10.1046/j.1365-2478.1997.3200262.x.

Lomax, A., and R. Snieder. 1994, Finding sets of acceptable solutions with a genetic algorithm with application to surface wave group dispersion in Europe. Geophysical Research Letters, **21**, no. 24,2617-2620.

Luo, Y., J. Xia, J. Liu, Q. Liu, and S. Xu. 2007, Joint inversion of high-frequency surface waves with fundamental and higher modes. Journal of Applied Geophysics, **62**, no. 4,375-384.

Luo, Y., J. Xia, R. D. Miller, Y. Xu, J. Liu, and Q. Liu. 2008, Rayleigh-wave dispersive energy imaging using a high-resolution linear Radon transform. Pure and Applied Geophysics, **165**, no. 5,903-922.

Lynn, H. B., R. Bates, M. Layman, and M. Jones. 1995, Natural fracture characterization using P-wave reflection seismic data, VSP, borehole imaging logs, and the in-situ stress field determination, 1995.

Lynn, H. B., and L. A. Thomsen. 1990, Reflection shear-wave data collected near the principal axes of azimuthal anisotropy. Geophysics, **55**, no. 2,147-156.

Lyons, J. B., S. Tufts-Moore, E. D. Koozmin, T. Falk, and D. P. Mathieux. 1997, Bedrock geologic map of New Hampshire: The Survey.

Marfurt, K. J., R. V. Schneider, and M. C. Mueller. 1996, Pitfalls of using conventional and discrete Radon transforms on poorly sampled data. Geophysics, **61**, no. 5,1467-1482.

Martin, M. A., and T. L. Davis. 1987, Shear-wave birefringence: A new tool for evaluating fractured reservoirs. The Leading Edge, **6**, no. 10,22-28.

McEvilly, T. V. 1964, Central US crust—upper mantle structure from Love and Rayleigh wave phase velocity inversion. Bulletin of the Seismological Society of America, **54**, no. 6A,1997-2015.

McHone, J. G. 1984, Mesozoic igneous rocks of northern New England and adjacent Quebec: Geological Society of America.

McMechan, G. A., and M. J. Yedlin. 1981, Analysis of dispersive waves by wave field transformation. Geophysics, **46**, no. 6,869-874.

Merrien-Soukatchoff, V., T. Korini, and A. Thoraval. 2012, Use of an integrated discrete fracture network code for stochastic stability analyses of fractured rock masses. Rock Mechanics and Rock Engineering, **45**, no. 2,159-181.

Michalski, A., and R. Britton. 1997, The role of bedding fractures in the hydrogeology of sedimentary bedrock—evidence from the Newark Basin, New Jersey. Groundwater, **35**, no. 2,318-327.

Miller, R. D., S. E. Pullan, D. W. Steeples, and J. A. Hunter. 1994, Field comparison of shallow P-wave seismic sources near Houston, Texas. Geophysics, **59**, no. 11,1713-1728.

Miller, R. D., S. E. Pullan, J. S. Waldner, and F. P. Haeni. 1986, Field comparison of shallow seismic sources. Geophysics, **51**, no. 11,2067-2092.

Montagner, J.-P. 2007, Deep Earth structure—upper mantle structure: global isotropic and anisotropic elastic tomography. Treatise on geophysics, **1**,559-589.

Montagner, J.-P., and D. L. Anderson. 1989, Petrological constraints on seismic anisotropy. Physics of the earth and planetary interiors, **54**, no. 1-2,82-105.

Mueller, M. C. 1991, Prediction of lateral variability in fracture intensity using multicomponent shear-wave surface seismic as a precursor to horizontal drilling in the Austin Chalk. Geophysical Journal International, **107**, no. 3,409-415.

Nagai, K., A. O'Neill, Y. Sanada, and Y. Ashida. 2005, Genetic algorithm inversion of Rayleigh wave dispersion from CMPCC gathers over a shallow fault model. Journal of Environmental & Engineering Geophysics, **10**, no. 3,275-286.

Nakanishi, I., and D. L. Anderson. 1983, Measurement of mantle wave velocities and inversion for lateral heterogeneity and anisotropy: 1. Analysis of Great Circle Phase Velocities. Journal of Geophysical Research: Solid Earth, **88**, no. B12,10267-10283.

Nolet, G. 1981, Linearized inversion of (teleseismic) data, The solution of the inverse problem in geophysical interpretation: Springer. 9-37.

O'Neill, A., and T. Matsuoka. 2005, Dominant higher surface-wave modes and possible inversion pitfalls. Journal of Environmental & Engineering Geophysics, **10**, no. 2,185-201.

Olson, J. C. 1942, Mica-bearing pegmatites of New Hampshire: US Government Printing Office.

Olsson, O., L. Falk, O. Forslund, L. Lundmark, and E. Sandberg. 1992, Borehole radar applied to the characterization of hydraulically conductive fracture zones in crystalline rock 1. Geophysical prospecting, **40**, no. 2,109-142.

Park, C. B., R. D. Miller, and J. Xia. 1998, Imaging dispersion curves of surface waves on multi-channel record, SEG Technical Program Expanded Abstracts 1998: Society of Exploration Geophysicists. 1377-1380.

Park, C. B., R. D. Miller, J. Xia, and J. Ivanov. 2007, Multichannel analysis of surface waves (MASW)—active and passive methods. The Leading Edge, **26**, no. 1,60-64.

Paterson, N. R., and V. Ronka. 1971, Five years of surveying with the very low frequency electromagnetic method. Geoexploration, **9**, no. 1,7-26.

Reynolds, J. M. 2011, An introduction to applied and environmental geophysics: John Wiley & Sons.

Ryden, N., and C. B. Park. 2006, Fast simulated annealing inversion of surface waves on pavement using phase-velocity spectra. Geophysics, **71**, no. 4,R49-R58.

Safani, J., A. O'Neill, T. Matsuoka, and Y. Sanada. 2005, Applications of Love wave dispersion for improved shear-wave velocity imaging. Environmental and Engineering Geophysics, **10**, no. 2,135-150.

Sambridge, M. 1999, Geophysical inversion with a neighbourhood algorithm—I. Searching a parameter space. Geophysical Journal International, **138**, no. 2,479-494. doi: 10.1046/j.1365-246X.1999.00876.x.

Sato, Y. 1955, Analysis of dispersed surface waves by means of Fourier transform I. Bull. Earthq. Res. Inst., Univ. Tokyo, **33**,33-48.

Schlue, J. W., and L. Knopoff. 1977, Shear-wave polarization anisotropy in the Pacific Basin. Geophysical Journal of the Royal Astronomical Society, **49**, no. 1,145-165.

Schonewille, M. A., and A. J. W. Duijndam. 2001, Parabolic Radon transform, sampling and efficiency. Geophysics, **66**, no. 2,667-678.

Sen, M. K., and P. L. Stoffa. 1991, Nonlinear one-dimensional seismic waveform inversion using simulated annealing. Geophysics, **56**, no. 10,1624-1638.

Singhal, B. B. S., and R. P. Gupta. 2010, Applied hydrogeology of fractured rocks: Springer Science & Business Media.

Socco, V. L., D. Boiero, M. Maraschini, M. Vanneste, C. Madshus, H. Westerdahl, K. Duffaut, and E. Skomedal. 2011, On the use of the Norwegian Geotechnical

Institute's prototype seabed-coupled shear wave vibrator for shallow soil characterization-II. Joint inversion of multimodal Love and Scholte surface waves. Geophysical Journal International, **185**, no. 1,237-252.

Swanson, S. K. 2007, Lithostratigraphic controls on bedding-plane fractures and the potential for discrete groundwater flow through a siliciclastic sandstone aquifer, southern Wisconsin. Sedimentary Geology, **197**, no. 1-2,65-78.

Swanson, S. K., J. M. Bahr, K. R. Bradbury, and K. M. Anderson. 2006, Evidence for preferential flow through sandstone aquifers in Southern Wisconsin. Sedimentary Geology, **184**, no. 3-4,331-342.

Tarantola, A. 1987, Inverse problem theory: Method for data fitting and model parameter estimation. Elsevier, **613**.

Thomsen, L. 1986, Weak elastic anisotropy. Geophysics, **51**, no. 10,1954-1966.

Tomar, G., N. M. Shapiro, A. Mordret, S. C. Singh, and J.-P. Montagner. 2017, Radial anisotropy in Valhall: ambient noise-based studies of Scholte and Love waves. Geophysical Journal International, **208**, no. 3,1524-1539.

Trad, D., T. Ulrych, and M. Sacchi. 2003, Latest views of the sparse Radon transform. Geophysics, **68**, no. 1,386-399.

Trad, D. O., T. J. Ulrych, and M. D. Sacchi. 2002, Accurate interpolation with high-resolution time-variant Radon transforms. Geophysics, **67**, no. 2,644-656.

Tsvankin, I., and V. Grechka. 2006, Developments in seismic anisotropy: Treating realistic subsurface models in imaging and fracture detection. CSEG Recorder, **31**, no. special edition,43-46.

Valcke, S. L. A., M. Casey, G. E. Lloyd, J. M. Kendall, and Q. J. Fisher. 2006, Lattice preferred orientation and seismic anisotropy in sedimentary rocks. Geophysical Journal International, **166**, no. 2,652-666.

Vanlier, K. E. 1963, Ground-water in Menominee County. Vol. 2.

Vecsey, L., J. Plomerová, and V. Babuška. 2008, Shear-wave splitting measurements—Problems and solutions. Tectonophysics, **462**, no. 1-4,178-196.

Wathelet, M. 2008, An improved neighborhood algorithm: parameter conditions and dynamic scaling. Geophysical Research Letters, **35**, no. 9.

Wathelet, M., D. Jongmans, and M. Ohrnberger. 2004, Surface-wave inversion using a direct search algorithm and its application to ambient vibration measurements. Near surface geophysics, **2**, no. 4,211-221.

Wei, J.-X., J.-G. Zhao, D. Shuai, B.-R. Di, and S.-Y. Qin. 2018, Estimations of P-and S-wave velocities and anisotropy from measurements on artificial fractured samples. Geophysics, **83**, no. 3,MR107-MR121.

Wood, T. R., and G. T. Norrell. 1996, Integrated large-scale aquifer pumping and infiltration tests: groundwater pathways, OU 7-06: Summary Report: Idaho National Engineering Laboratory, Environmental Restoration Department, Lockheed Martin Idaho Technologies Company.

Xia, J., R. D. Miller, and C. B. Park. 1999, Estimation of near-surface shear-wave velocity by inversion of Rayleigh waves. Geophysics, **64**, no. 3,691-700.

Xia, J., R. D. Miller, C. B. Park, and G. Tian. 2003, Inversion of high frequency surface waves with fundamental and higher modes. Journal of Applied Geophysics, **52**, no. 1,45-57.

Xia, J., Y. Xu, Y. Luo, R. D. Miller, R. Cakir, and C. Zeng. 2012, Advantages of using multichannel analysis of Love waves (MALW) to estimate near-surface shear-wave velocity. Surveys in Geophysics, **33**, no. 5,841-860.

Xie, H., and L. Liu. 2015, Near-surface anisotropic structure characterization by Love wave inversion for assessing ground conditions in urban areas. Journal of Earth Science, **26**, no. 6,807-812.

Xie, J., M. H. Ritzwoller, W. Shen, Y. Yang, Y. Zheng, and L. Zhou. 2013, Crustal radial anisotropy across eastern Tibet and the western Yangtze craton. Journal of Geophysical Research: Solid Earth, **118**, no. 8,4226-4252.

Yilmaz, O. 1987, Seismic data processing, volume 2 of Investigations in Geophysics. Society of Exploration Geophysicists.

Yilmaz, O., and M. T. Taner. 1994, Discrete plane-wave decomposition by least-mean-square-error method. Geophysics, **59**, no. 6,973-982.

A Data processing detail view in each line

In section 6 the detail of the data processing of Line 1 was presented; the detail data processing step for Lines 2 - 6 is listed here.

A.1 Data Processing for Line 2

As mentioned earlier, data processing for Line 2 followed the flow chart in Table 2 for our data processing. In the Rayleigh wave data, windowing was applied to better identify different modes and for the Love wave data, final few traces were excluded to have better distinguishable modes.

A.1.1 Rayleigh Wave

For the Rayleigh wave data, the same processing workflow was followed including stacking (Figure A.1), normalizing the traces (Figure A.2a), muting (Figure A.2b), low pass filter (Figure A.3), and f-k filter (Figure A.4). After these, windowing was applied In Line 2 Rayleigh wave data, the fundamental mode of the Rayleigh wave data is observable from the 1st to 9th geophones. The first higher mode was observable from 7th to 18th geophone and the second higher mode from the 1st to 24th geophones (Figure 15).

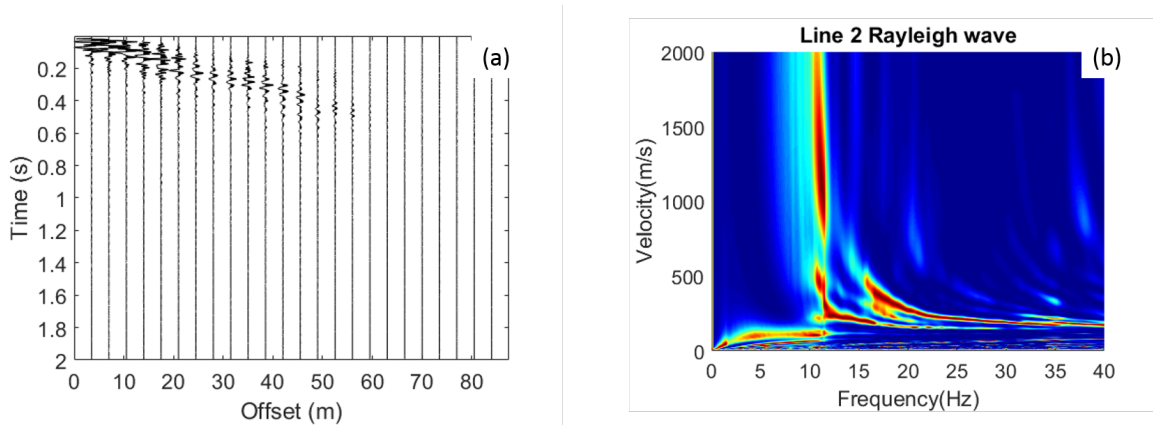

Figure A.1. Line 2 Rayleigh wave analysis from Mirror Lake. (a) Seismic record of the gather after stacking vertical components from five shots. (b) Phase velocity image before additional processing; in this figure it is difficult to identify any continuous trend of the dispersion curves

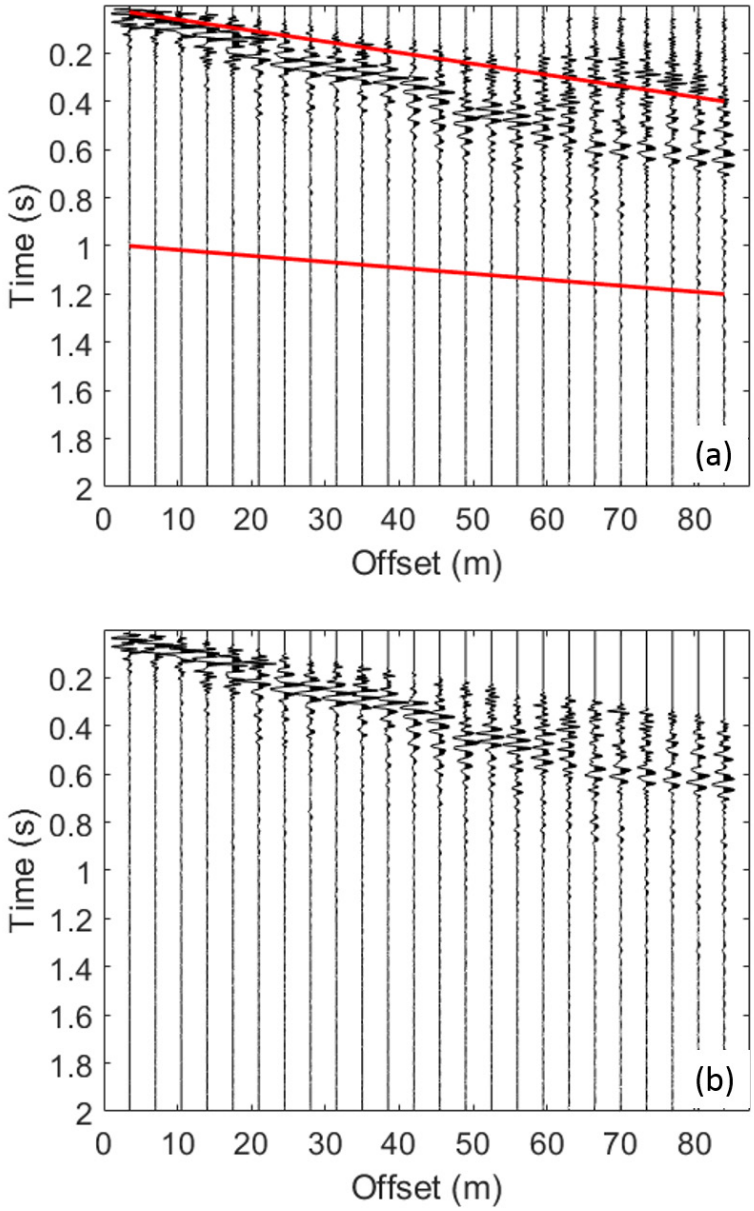

Figure A.2. (a) Line 2 Rayleigh wave normalized seismic trace with top and down muting to preserve the surface wave only. The seismic data was preserved within two red lines. The body waves were muted from the top and the noise from the bottom is also muted. (b) Line 2 Rayleigh wave data after applied muting.

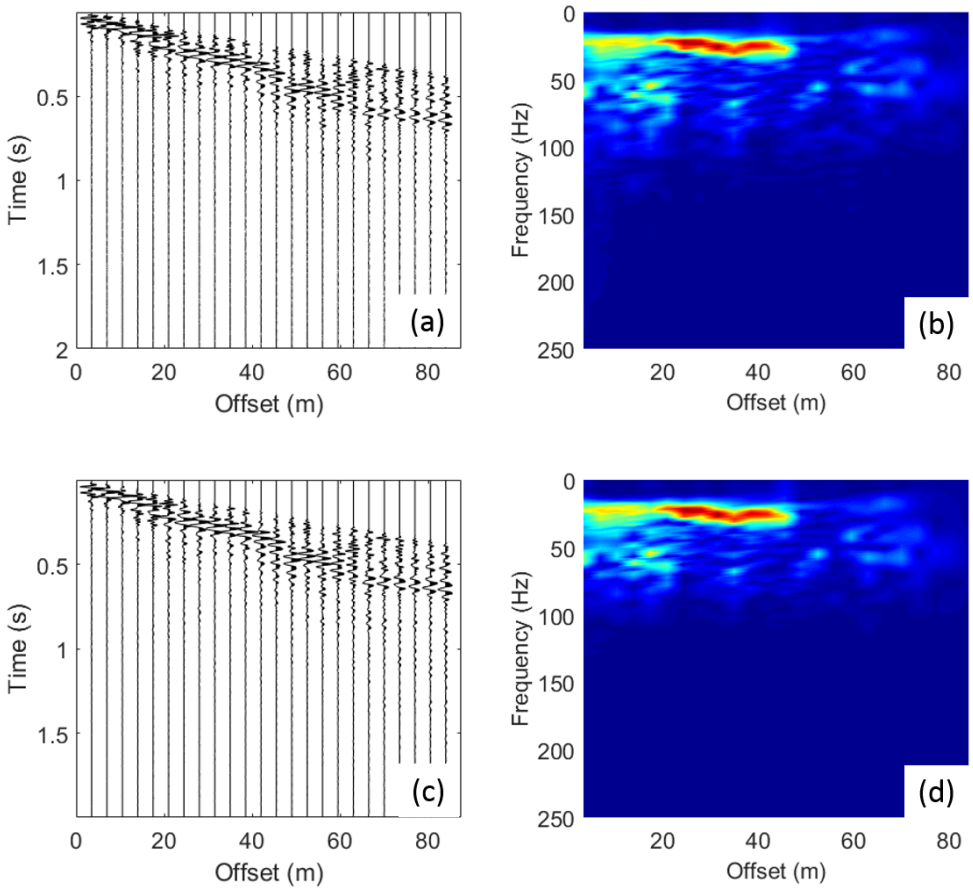

Figure A.3. Line 2 Rayleigh wave data comparison before (a) and after (c) applying a low pass filter (0 - 80 Hz). The f-x spectrum before (b) and after (d) applying filter.

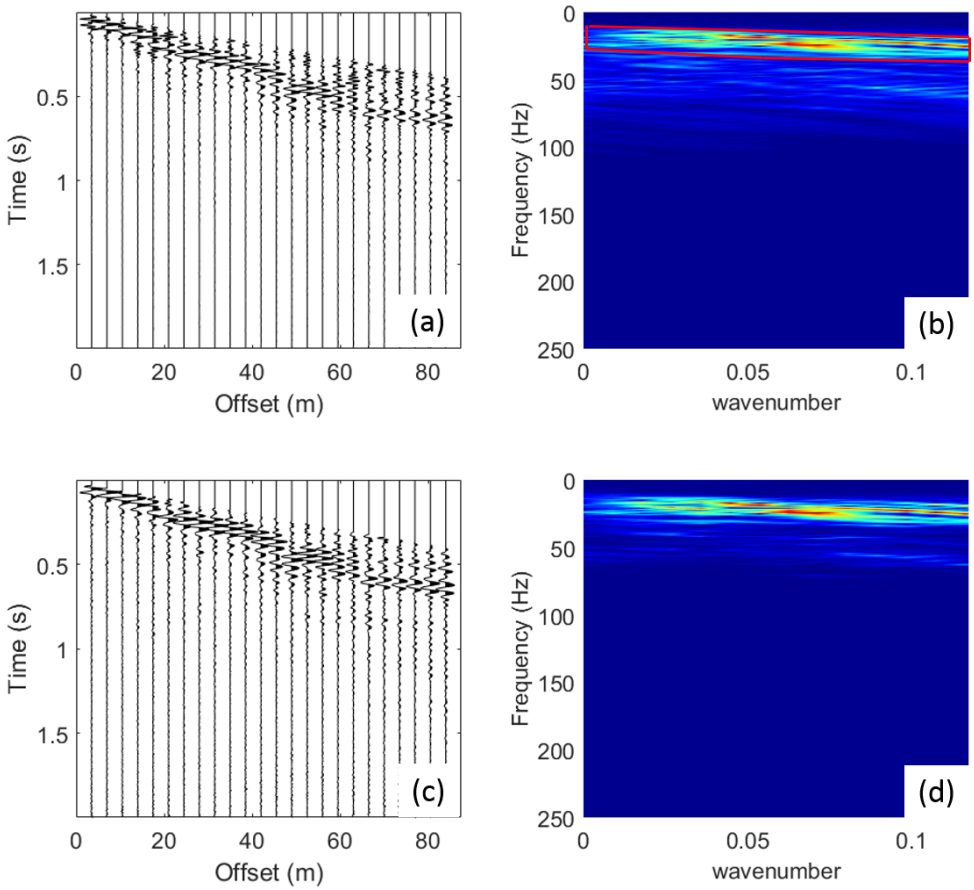

Figure A.4. Line 2 Rayleigh wave data comparison before (a) and after (c) applying an f-k filter. The f-k spectrum before (b) and after (d) applying filter. The red polygon in (b) highlights the surface waves within the f-k domain which the f-k filter is designed to preserve.

A.1.2 Love wave

For the Love wave data, the same processing workflow was followed including stacking (Figure A.5), normalizing the traces (Figure A.6a), muting (Figure A.6b), low pass filter (Figure A.7), and f-k filter (Figure A.8).

For the Love wave data, windowing was not necessary, but also final few traces were excluded. Fundamental mode, first higher mode and second higher mode was obtained from 1st to 15th geophones (Figure 16).

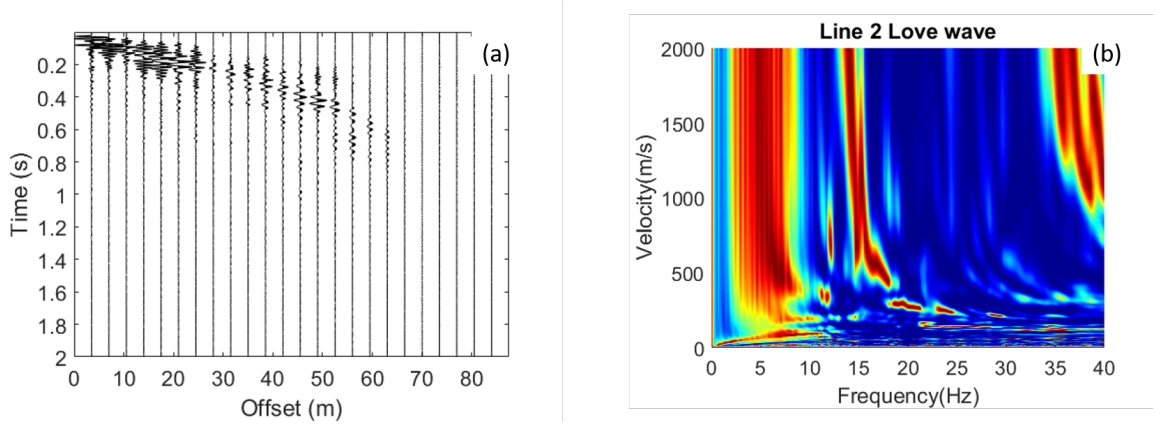

Figure A.5. Line 2 Love wave analysis from Mirror Lake. (a) Seismic record of the gather after stacking transverse components from five shots. (b) Phase velocity image before additional processing; in this figure, it is difficult to identify any continuous trend of the dispersion curves.

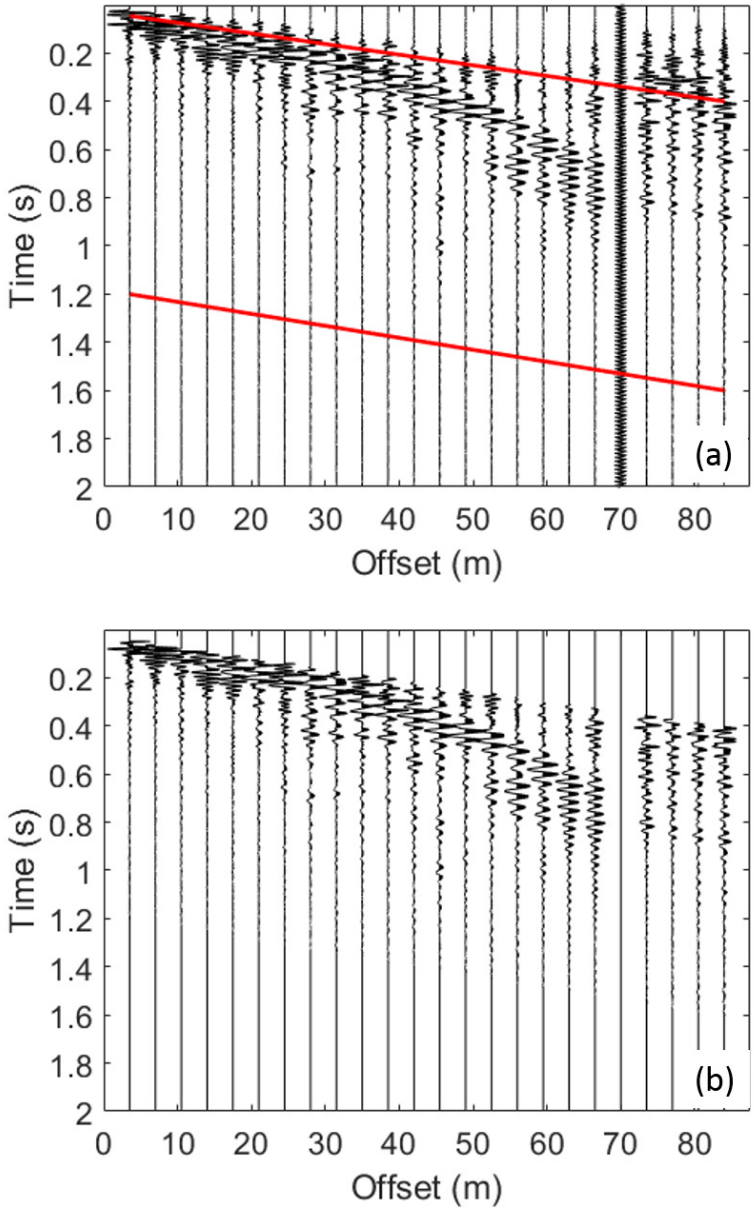

Figure A.6. Line 2 Love wave normalized seismic trace with top and down muting to preserve the surface wave only. The seismic data was preserved within two red lines. The body waves were muted from the top and the noise from the bottom is also muted. One noisy trace is also removed. (b) Line 2 Love wave data after applied muting.

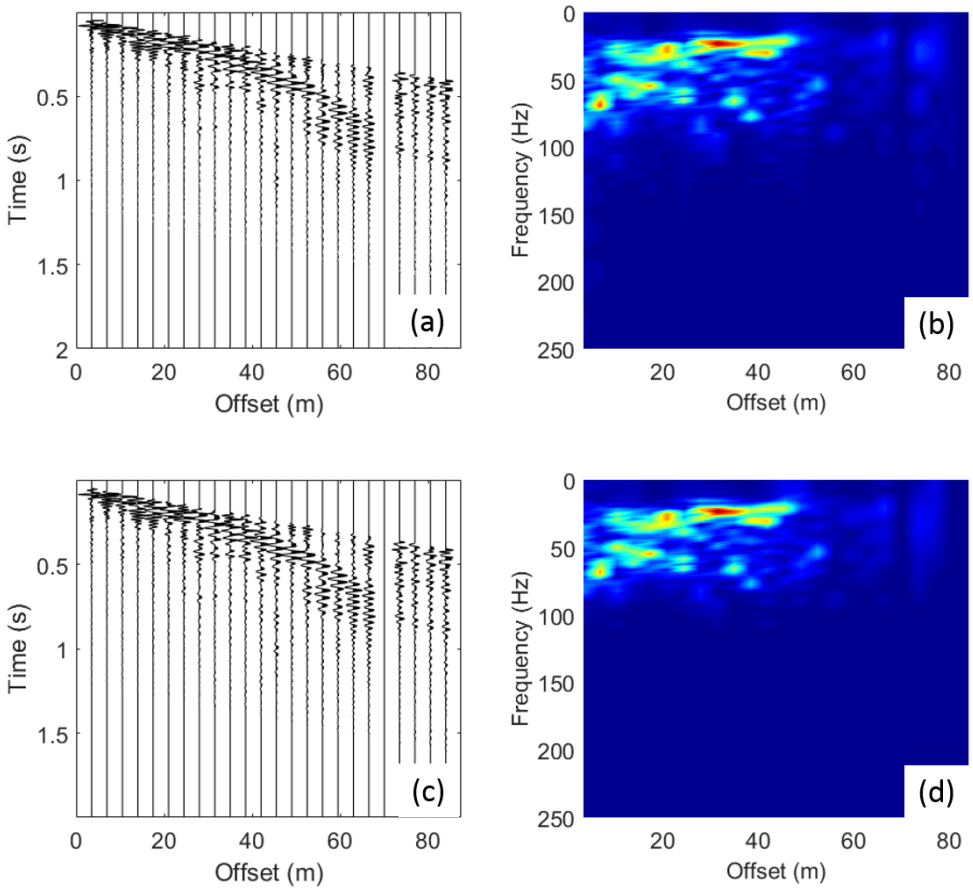

Figure A.7. Line 2 Love wave data comparison before (a) and after (c) applying a low pass filter (0 - 80 Hz). The f-x spectrum before (b) and after (d) applying filter.

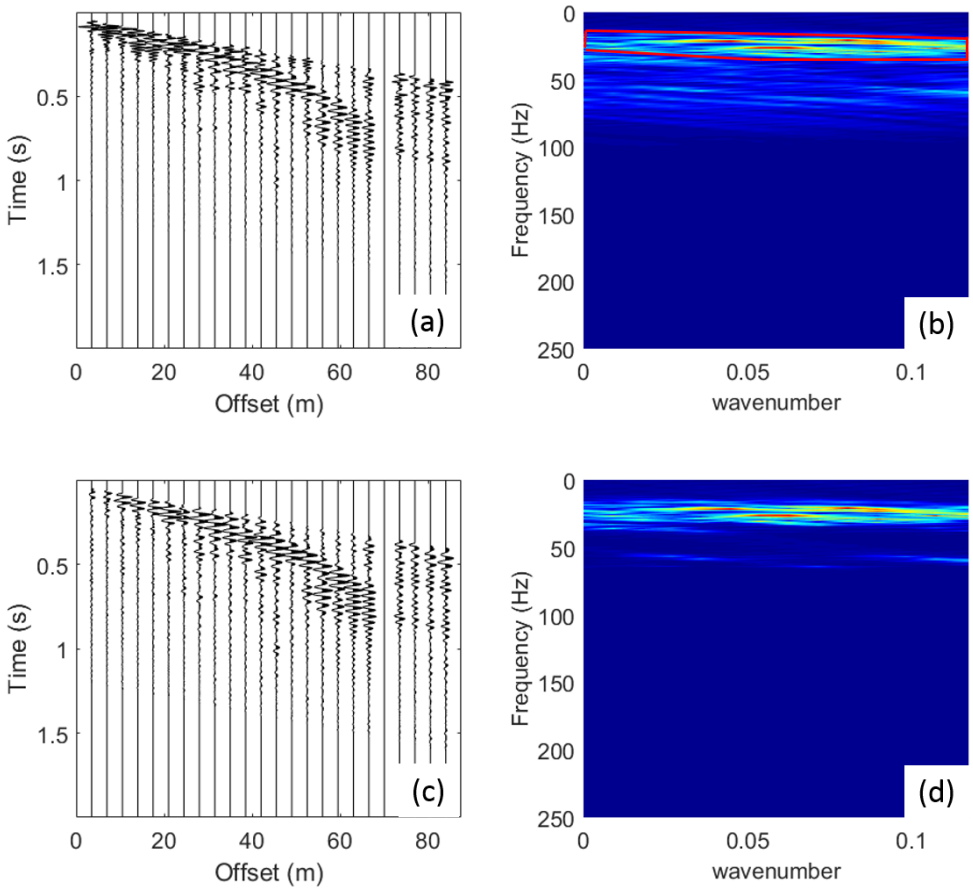

Figure A.8. Line 2 Love wave data comparison before (a) and after (c) applying an f-k filter. The f-k spectrum before (b) and after (d) applying filter. The red polygon in (b) highlights the surface waves within the f-k domain which the f-k filter is designed to preserve.

A.2 Data Processing for Line 3

Data processing of Line 3 follow the same flowchart in Table 2, however, in this dataset windowing is not needed to obtain different modes.

A.2.1 Rayleigh Wave

For the Rayleigh wave data, the same processing workflow was followed including stacking (Figure A.9), normalizing the traces (Figure A.10a), muting (Figure A.10b), low pass filter (Figure A.11), and f-k filter (Figure A.12). After these, fundamental and first higher modes of the Rayleigh waves were obtained (Figure 17).

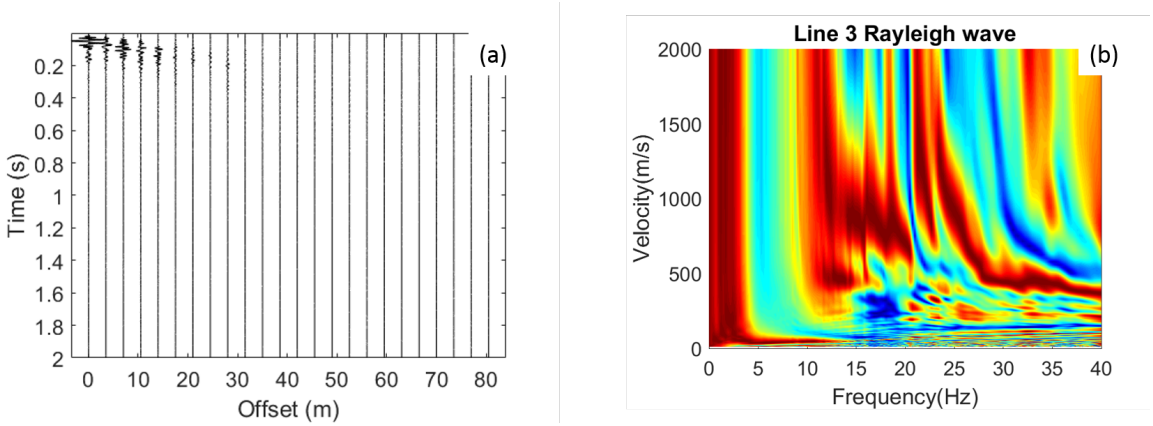

Figure A.9. (a) Line 3 Rayleigh wave seismic record and (b) the phase velocity before any processing.

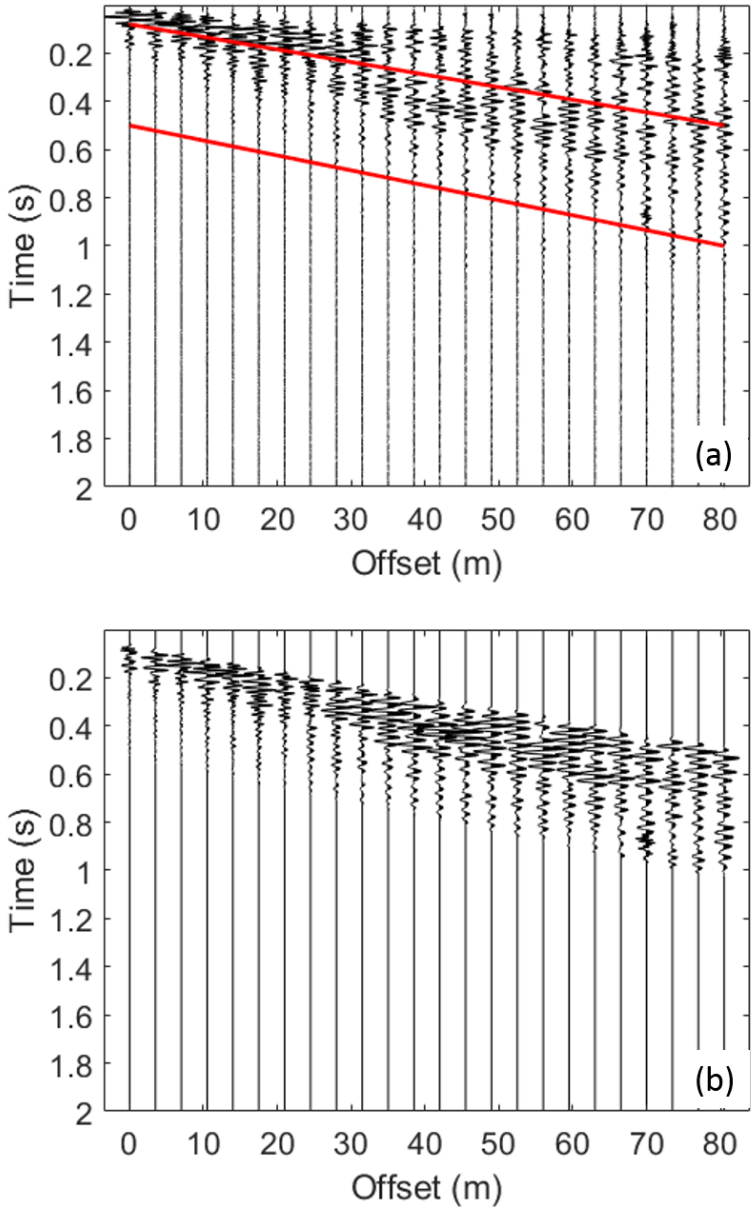

Figure A.10. (a) Line 3 Rayleigh wave normalized seismic trace with top and down muting to preserve the surface wave only. The seismic data was preserved within two red lines. The body waves were muted from the top and the noise from the bottom is also muted. (b) Line 3 Rayleigh wave data after applied muting.

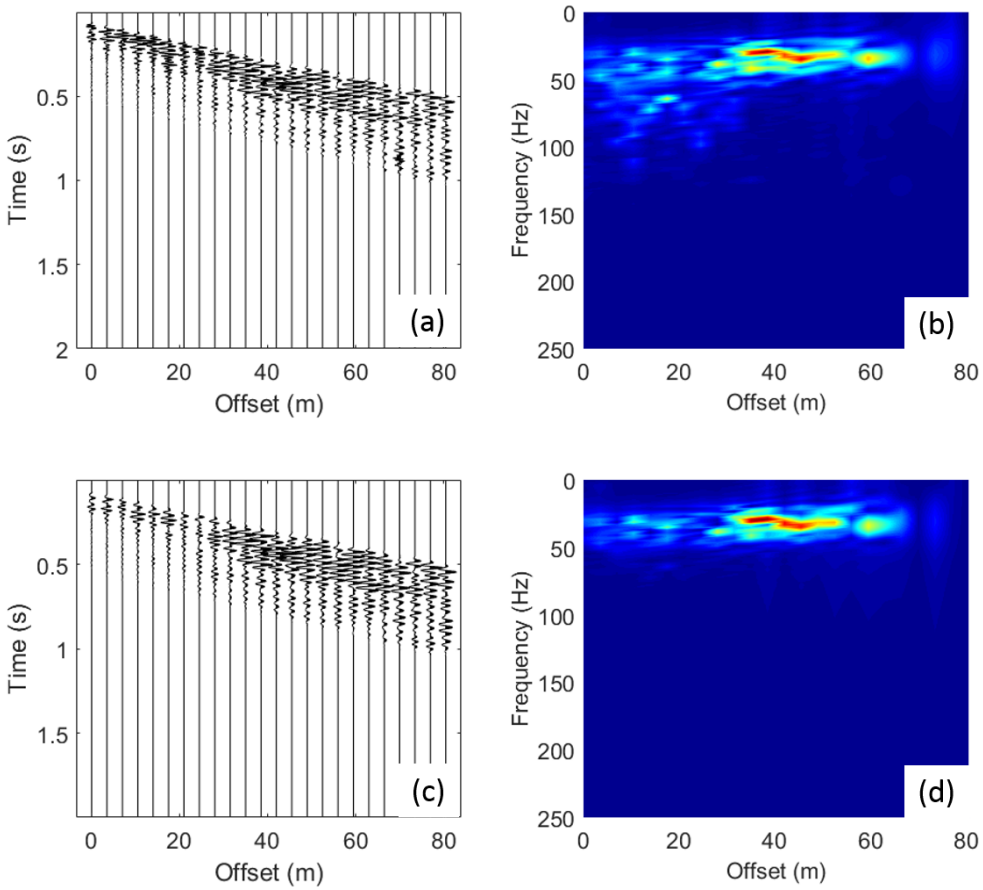

Figure A.11. Line 3 Rayleigh wave data comparison before (a) and after (c) applying a low pass filter (0 - 80 Hz). The f-x spectrum before (b) and after (d) applying filter.

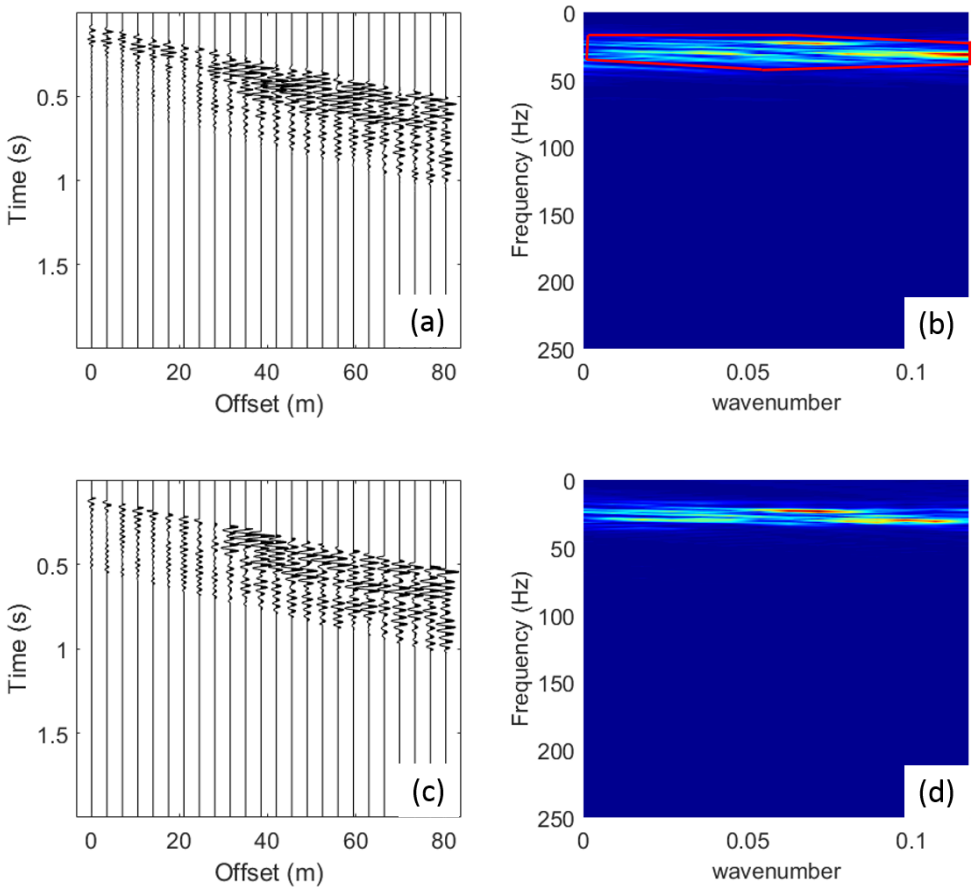

Figure A.12. Line 3 Rayleigh wave data comparison before (a) and after (c) applying an f-k filter. The f-k spectrum before (b) and after (d) applying filter. The red polygon in (b) highlights the surface waves within the f-k domain which the f-k filter is designed to preserve.

A.2.2 Love wave

For the Love wave data, same processing workflow was followed including stacking (Figure A.13), normalizing the traces (Figure A.14a), muting (Figure A.14b), low pass

filter (Figure A.15), and f-k filter (Figure A.16). For the Love wave dataset, fundamental and first higher modes were obtained (Figure 18).

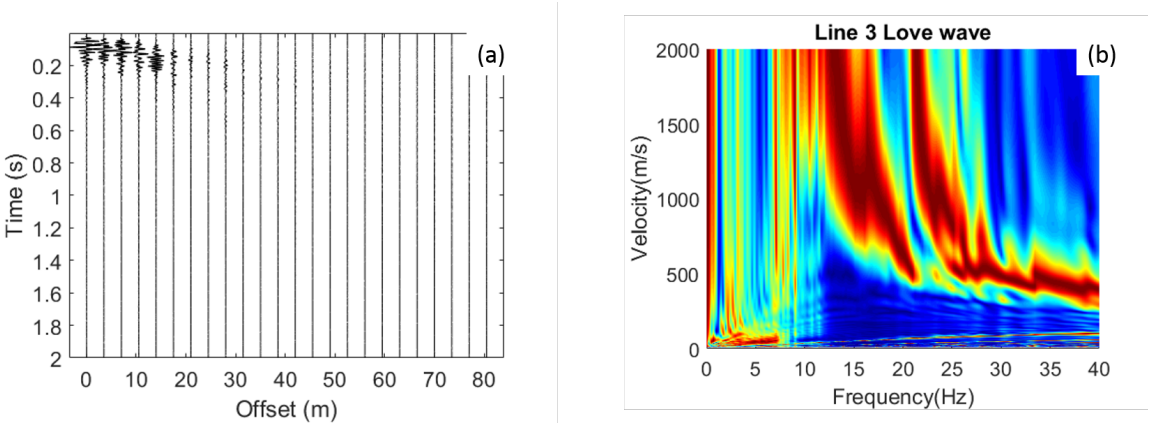

Figure A.13. (a) Line 3 Love wave seismic record and (b) the phase velocity before any processing.

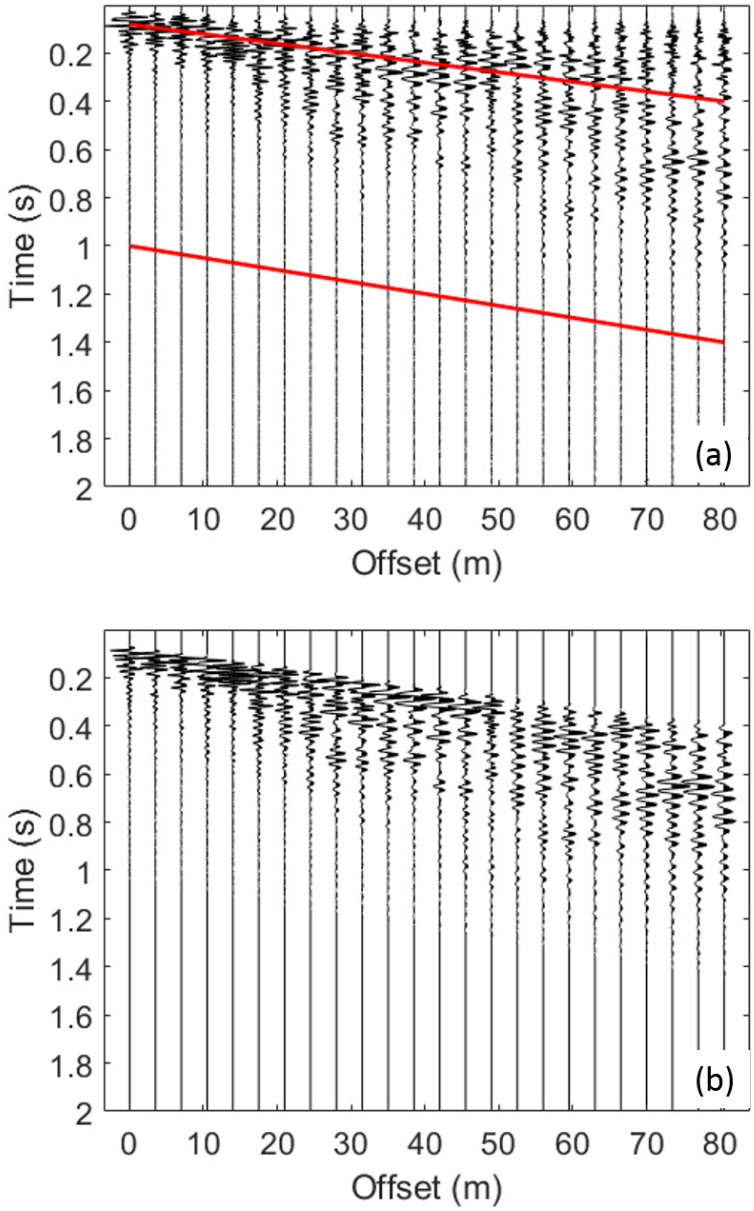

Figure A.14. (a) Line 3 Love wave normalized seismic trace with top and down muting to preserve the surface wave only. The seismic data was preserved within two red lines. The body waves were muted from the top and the noise from the bottom is also muted. (b) Line 3 Love wave data after applied muting.

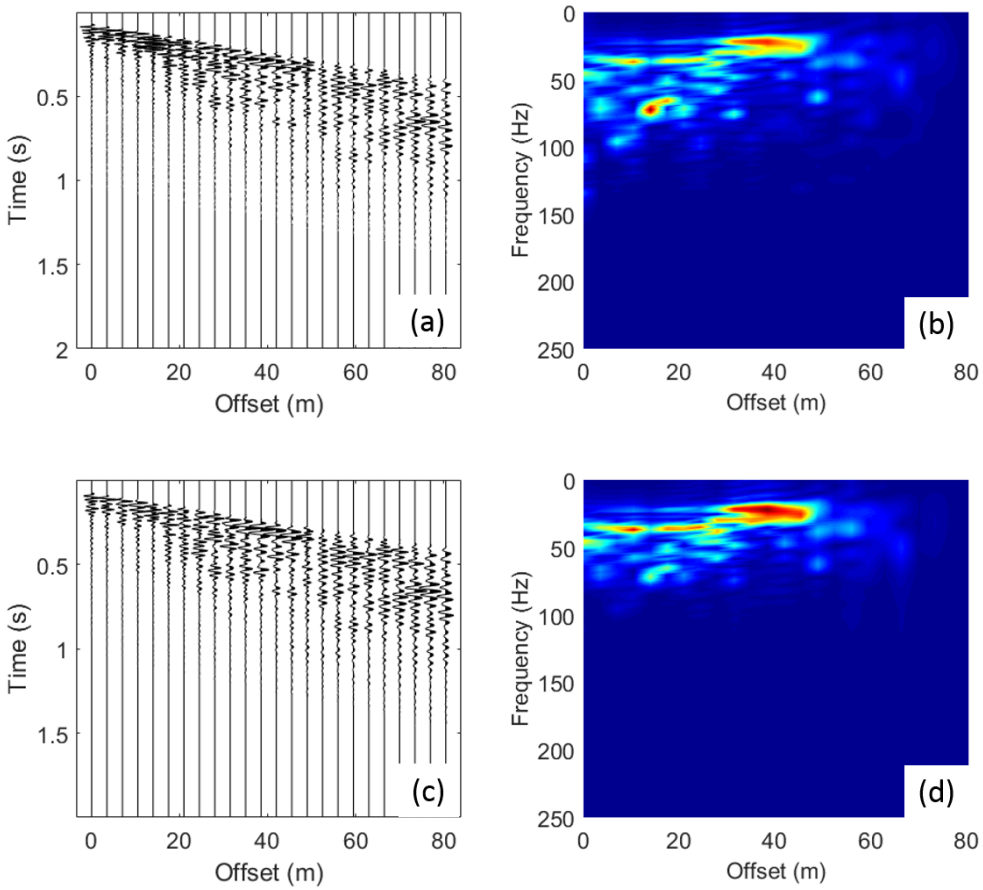

Figure A.15. Line 3 Love wave comparison before (a) and after (c) applying a low pass filter (0 - 80 Hz). The f-x spectrum before (b) and after (d) applying filter.

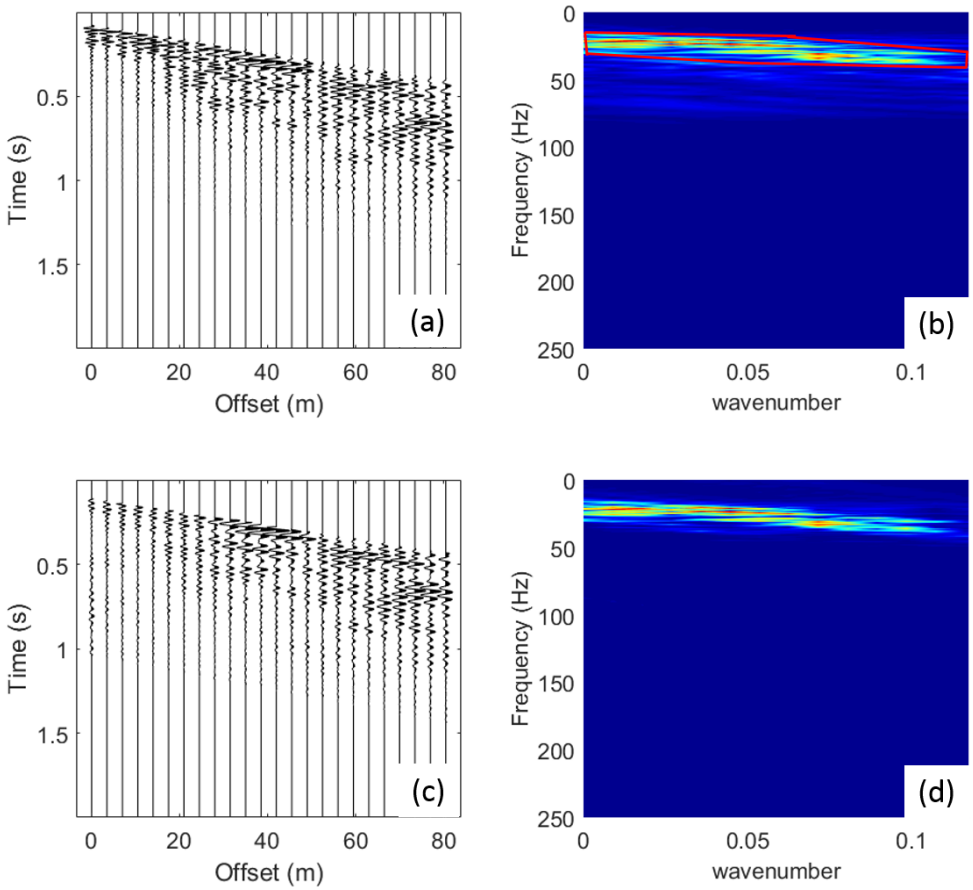

Figure A.16. Line 3 Love wave data comparison before (a) and after (c) applying an f-k filter. The f-k spectrum before (b) and after (d) applying filter. The red polygon in (b) highlights the surface waves within the f-k domain which the f-k filter is designed to preserve.

A.3 Data Processing for Line 4

Data processing of Line 4 follows the same flowchart in Table 2. In this dataset, three bad traces were removed in the shot record. In this dataset, windowing is not needed to obtain different modes.

A.3.1 Rayleigh Wave

For the Rayleigh wave data, the same processing workflow was followed including stacking (Figure A.17), normalizing the traces (Figure A.18a), muting (Figure A.18b), low pass filter (Figure A.19), and f-k filter (Figure A.20). In this dataset, fundamental mode and first higher mode was obtained (Figure 19).

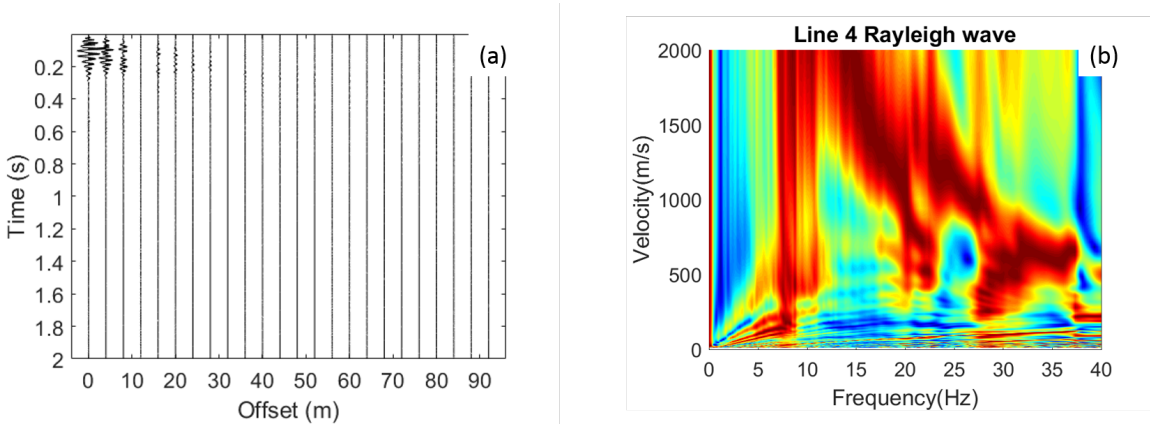

Figure A.17. (a) Line 4 Rayleigh wave seismic record. (b) The phase velocity before any processing.

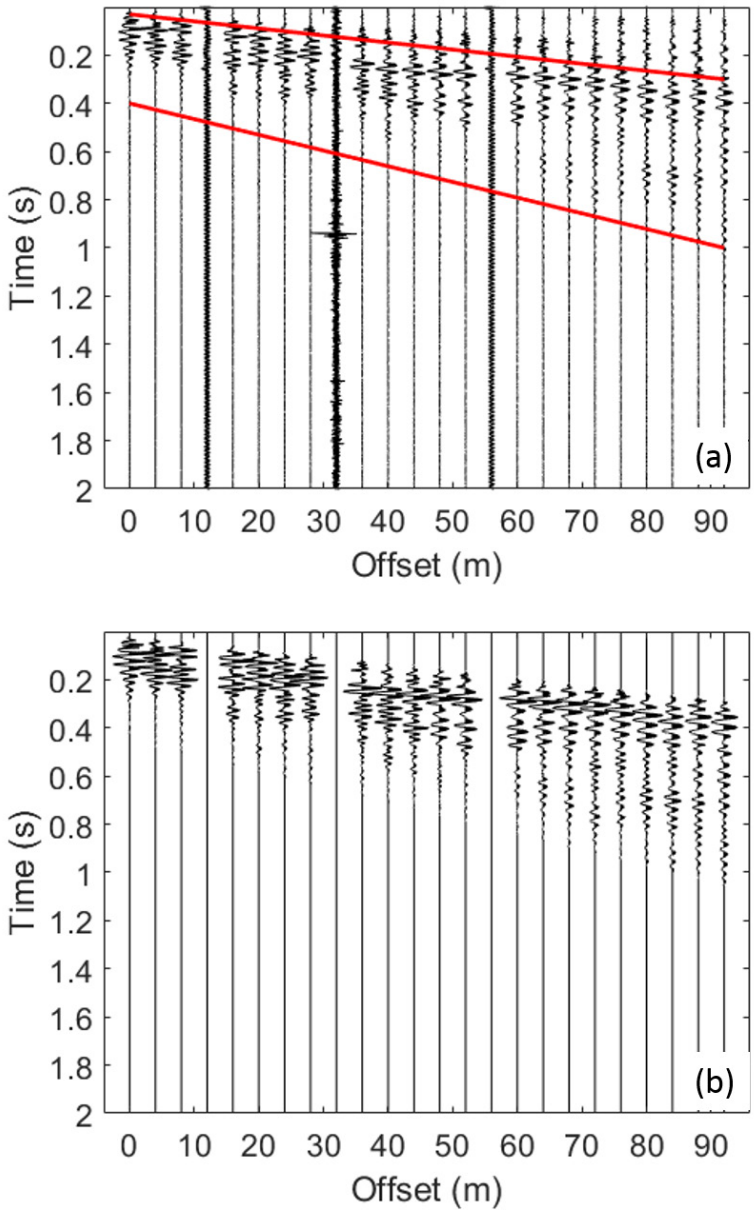

Figure A.18. (a) Line 4 Rayleigh wave normalized seismic trace with top and down muting to preserve the surface wave only. The seismic data was preserved within two red lines. The body waves were muted from the top and the noise from the bottom is also muted. Three noisy traces were removed from this dataset. (b) Line 4 Rayleigh wave data after applied muting.

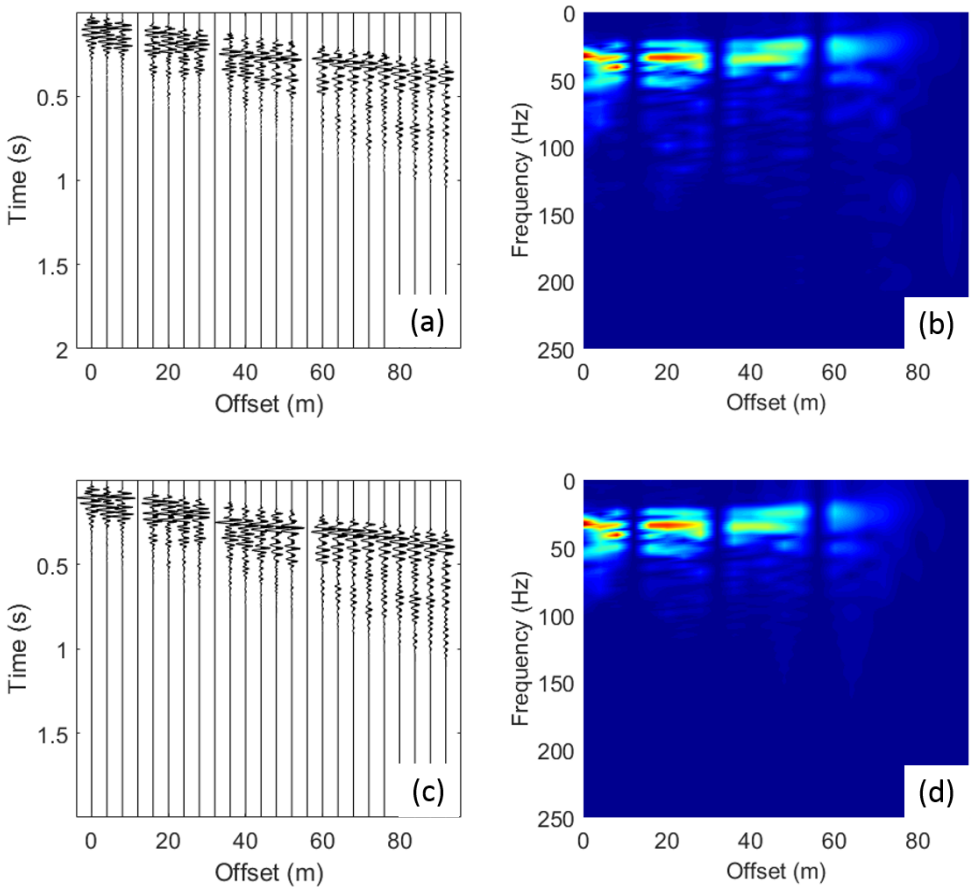

Figure A.19. Line 4 Rayleigh wave data comparison before (a) and after (c) applying a low pass filter (0 - 80 Hz). The f-x spectrum before (b) and after (d) applying filter.

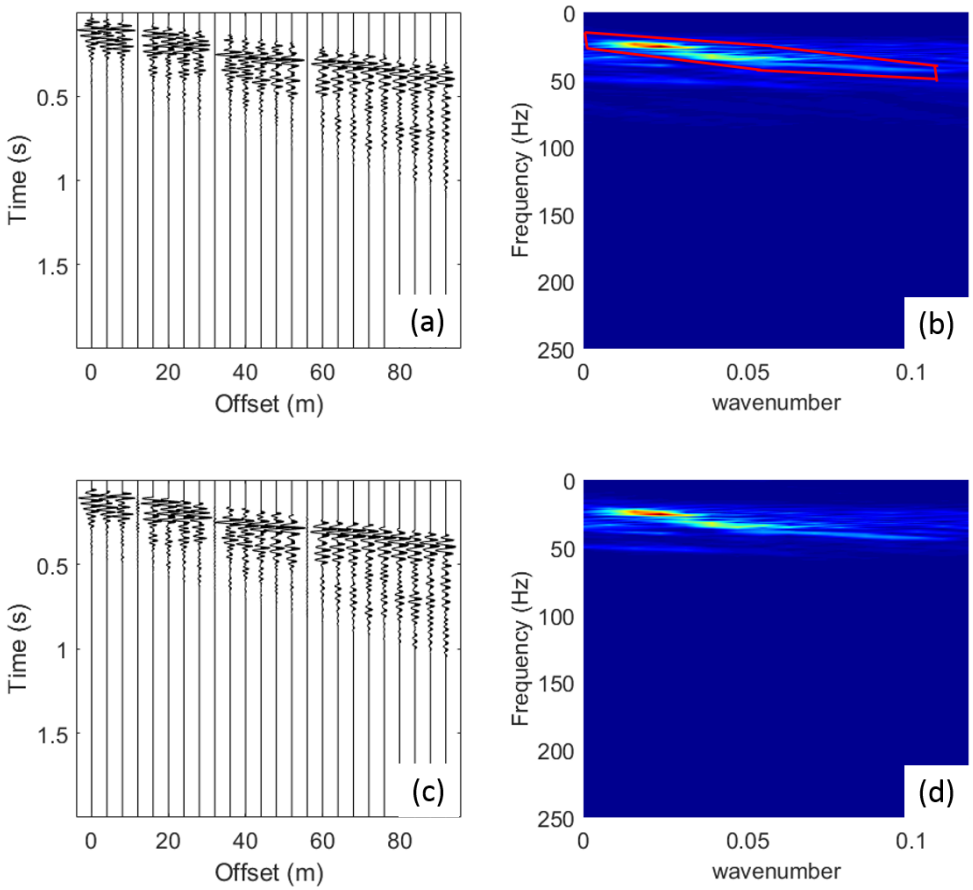

Figure A.20. Line 4 Rayleigh wave data comparison before (a) and after (c) applying an f-k filter. The f-k spectrum before (b) and after (d) applying filter. The red polygon in (b) highlights the surface waves within the f-k domain which the f-k filter is designed to preserve.

A.3.2 Love wave

For the Love wave data, same processing workflow was followed including stacking (Figure A.21), normalizing the traces (Figure A.22a), muting (Figure A.22b), and low

pass (Figure A.23) and f-k filters (Figure A.24). Fundamental and first higher modes of the Love waves was obtained in this dataset (Figure 20).

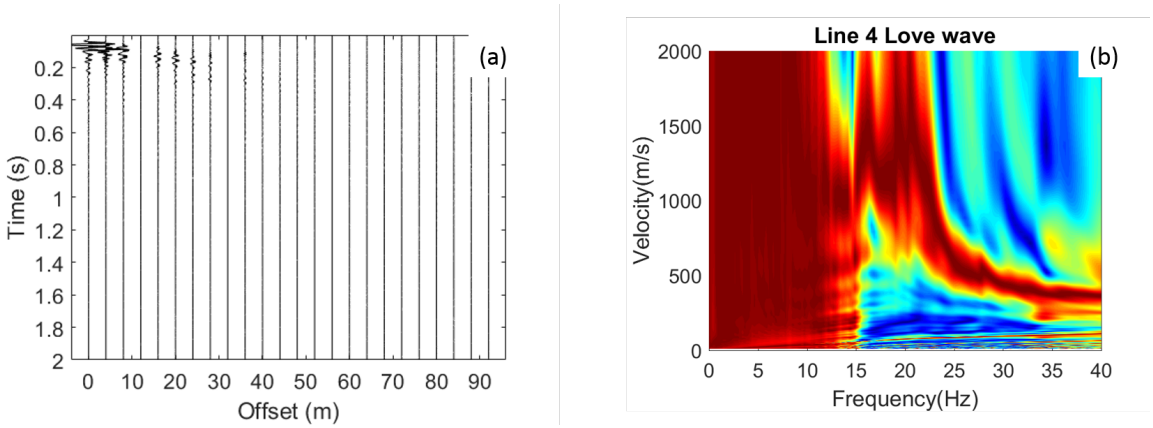

Figure A.21. (a) Line 4 Love wave seismic record and (b) the phase velocity before any processing.

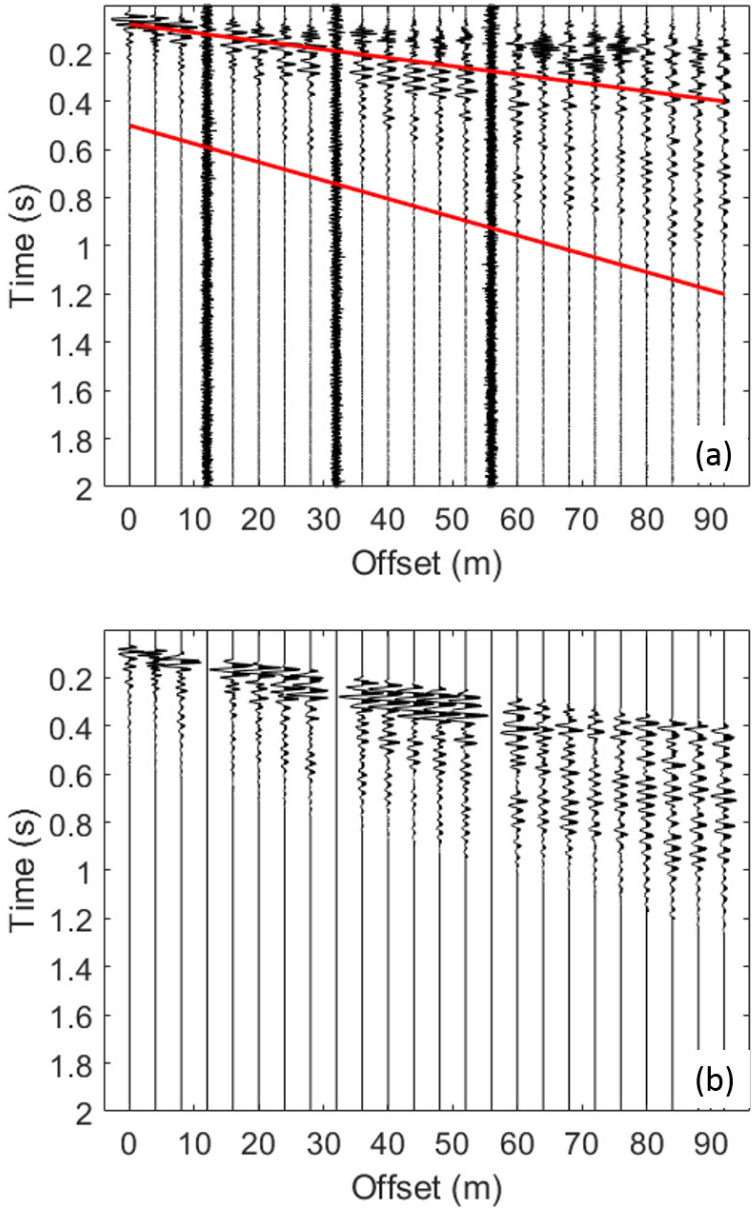

Figure A.22. (a) Line 4 Love wave normalized seismic trace with top and down muting to preserve the surface wave only. The seismic data was preserved within two red lines. The body waves were muted from the top and the noise from the bottom is also muted. Three noisy traces were removed from this dataset. (b) Line 4 Love wave data after applied muting.

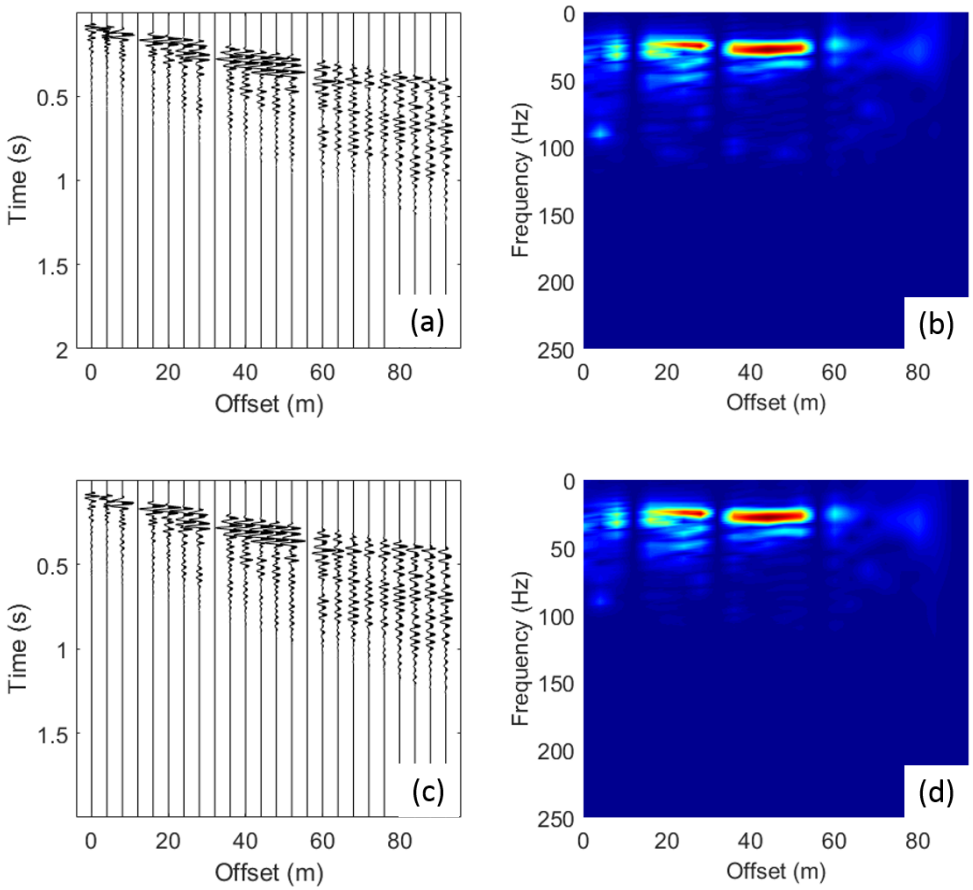

Figure A.23. Line 4 Love wave data comparison before (a) and after (c) applying a low pass filter (0 - 80 Hz). The f-x spectrum before (b) and after (d) applying filter.

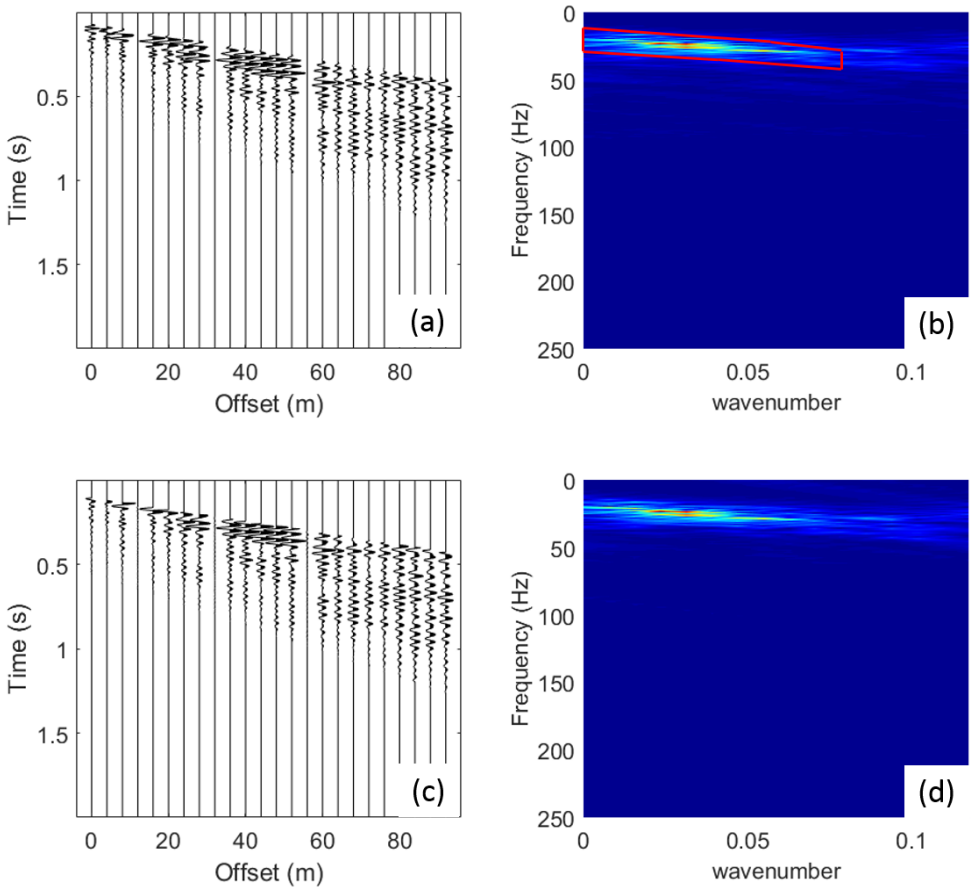

Figure A.24. Line 4 Love wave data comparison before (a) and after (c) applying an f-k filter. The f-k spectrum before (b) and after (d) applying filter. The red polygon in (b) highlights the surface waves within the f-k domain which the f-k filter is designed to preserve.

A.4 Data Processing for Line 5

Data processing of Line 5 follows the same flowchart in Table 2. In this dataset, two bad traces were removed in the shot record.

A.4.1 Rayleigh Wave

For the Rayleigh wave data, the same processing workflow was followed including stacking (Figure A.25), normalizing the traces (Figure A.25a), muting (Figure A.25b), low pass filter (Figure A.26), and f-k filters (Figure A.27). However, before normalizing the data some data from the bottom was removed since during the data acquisition there were some distributions. In Line 5 Rayleigh wave data, fundamental mode, first and second higher modes were obtained (Figure 21).

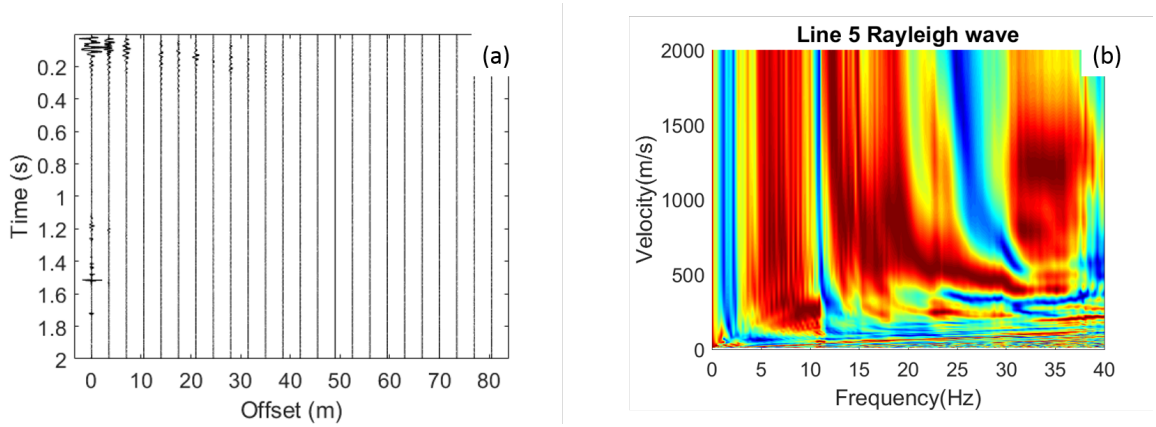

Figure A.25. (a) Line 5 Rayleigh wave seismic record and (b) the phase velocity before any processing.

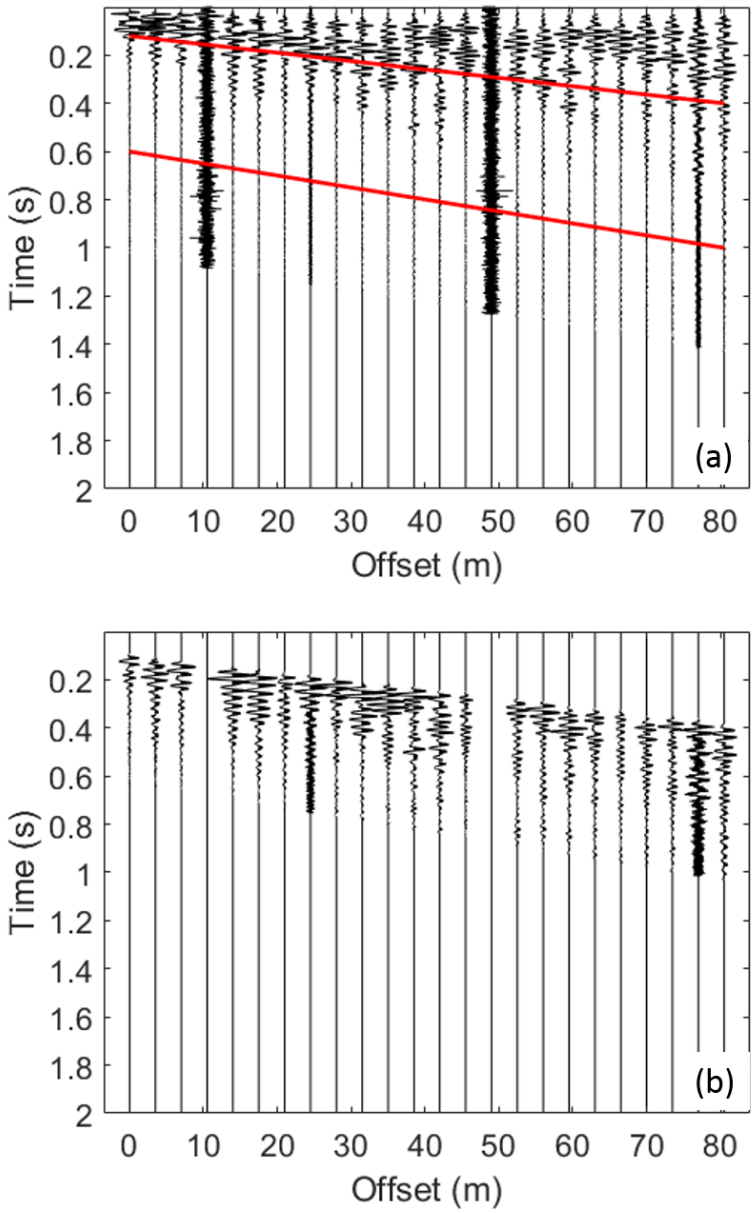

Figure A.26. (a) Line 5 Rayleigh wave normalized seismic trace with top and down muting to preserve the surface wave only. The seismic data was preserved within two red lines. The body waves were muted from the top and the noise from the bottom is also muted. Two noisy traces were removed from this dataset. (b) Line 5 Rayleigh wave data after applied muting.

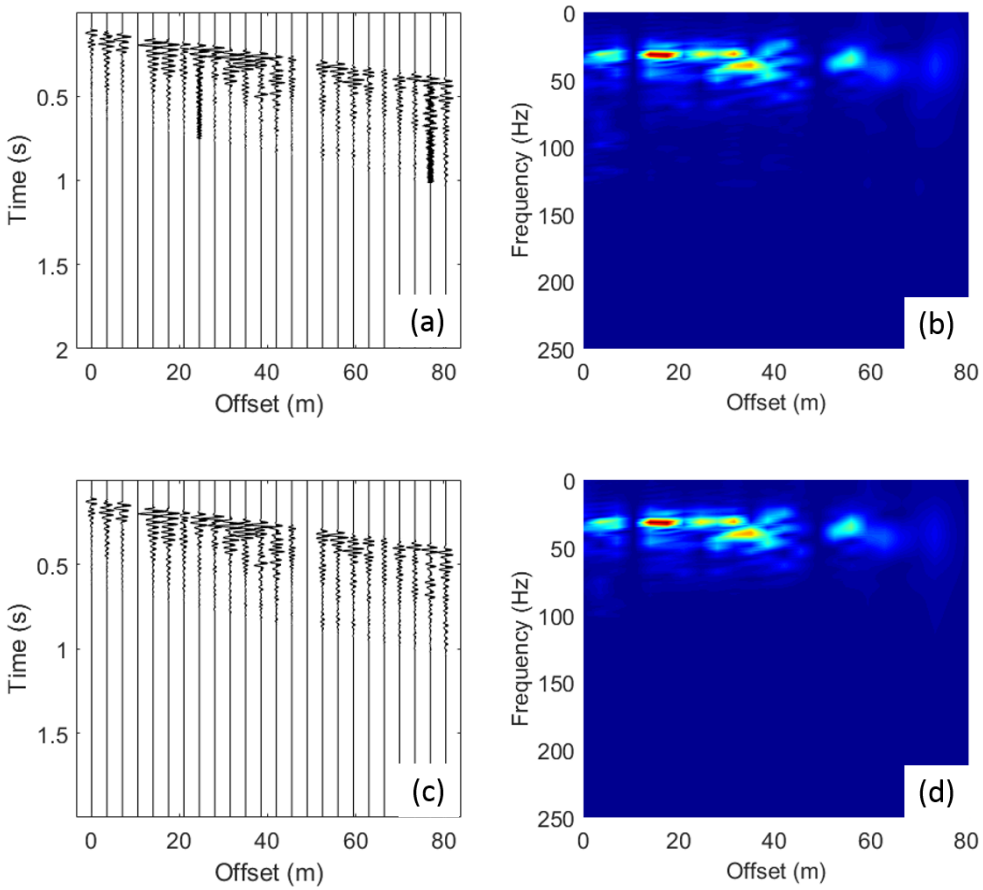

Figure A.27. Line 5 Rayleigh wave comparison before (a) and after (c) applying a low pass filter (0 - 80 Hz). The f-x spectrum before (b) and after (d) applying filter.

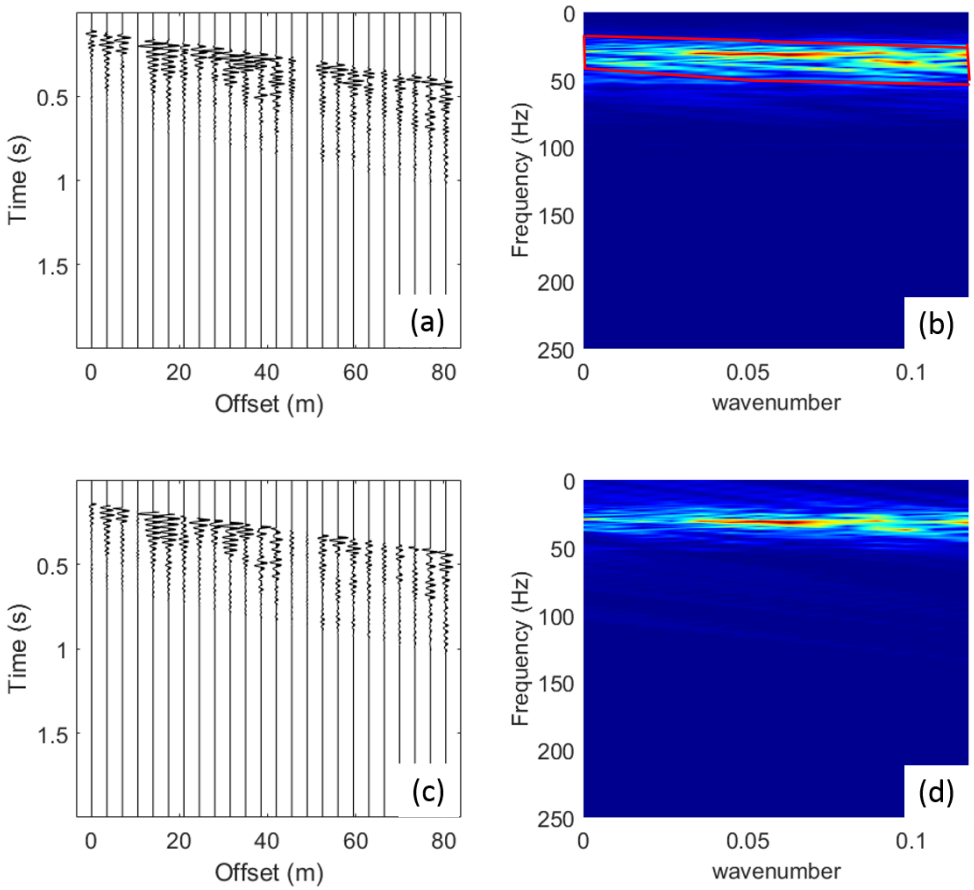

Figure A.28. Line 5 Rayleigh wave data comparison before (a) and after (c) applying an f-k filter. The f-k spectrum before (b) and after (d) applying filter. The red polygon in (b) highlights the surface waves within the f-k domain which the f-k filter is designed to preserve.

A.4.2 Love wave

For the Love wave data, the same processing workflow was followed including stacking (Figure A.29), normalizing the traces (Figure A.30a), muting (Figure A.30b), low pass

filter, and (Figure A.31) and f-k filter (Figure A.32). Different windowing wasn't applied in this dataset and obtained fundament, first higher and second higher modes (Figure 22).

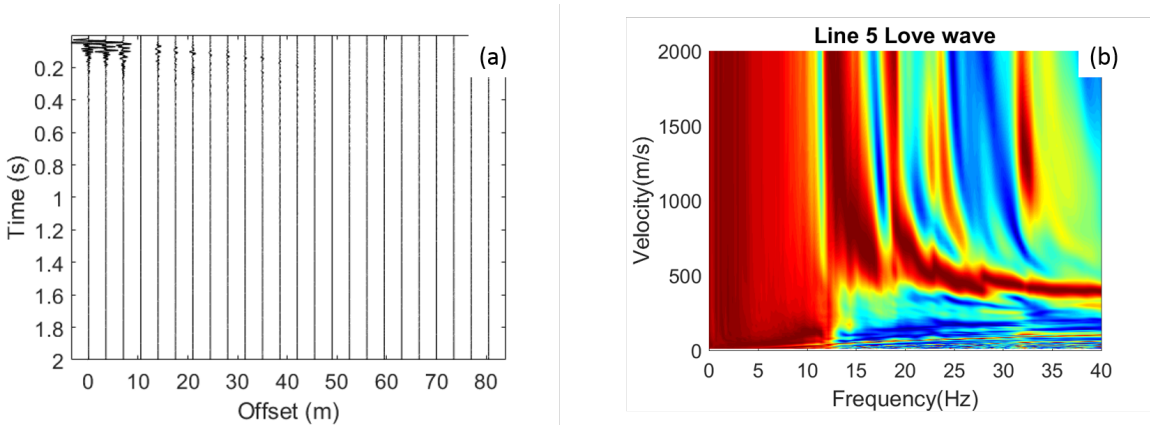

Figure A.29. (a) Line 5 Love wave seismic record and (b) the phase velocity before any processing.

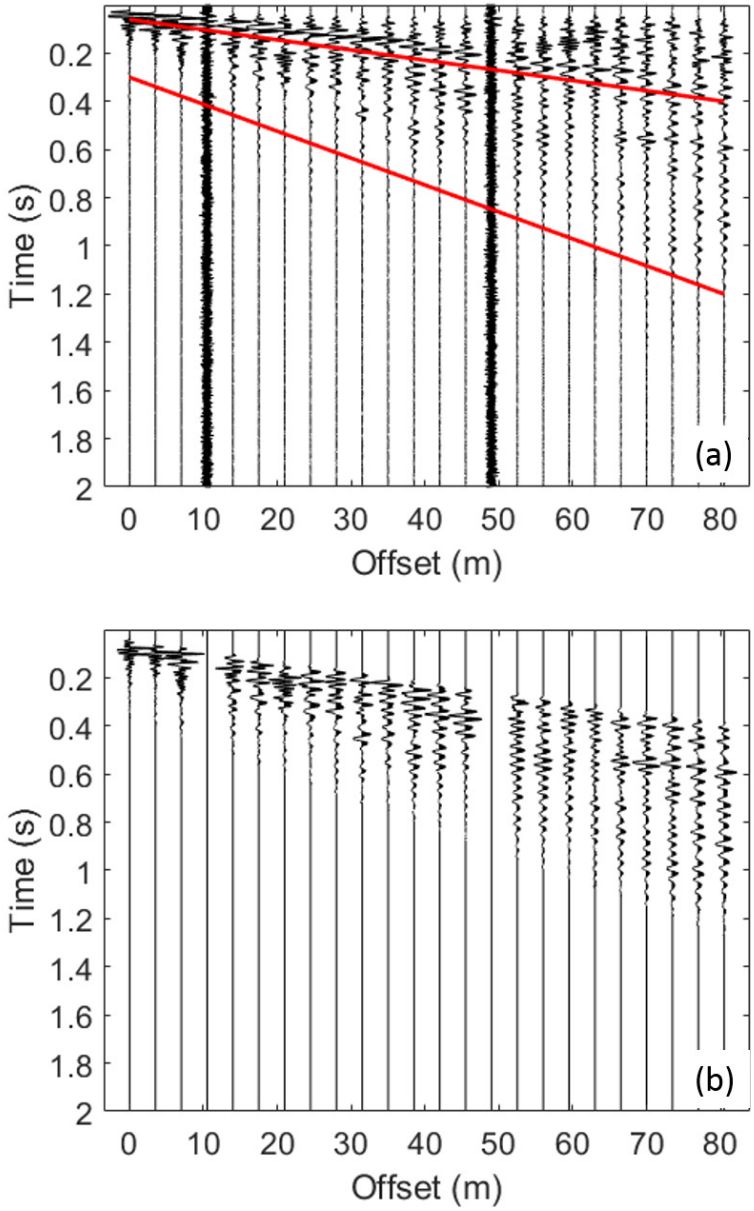

Figure A.30. (a) Line 5 Love wave normalized seismic trace with top and down muting to preserve the surface wave only. The seismic data was preserved within two red lines. The body waves were muted from the top and the noise from the bottom is also muted. Two noisy traces were removed from this dataset. (b) Line 5 Love wave data after applied muting.

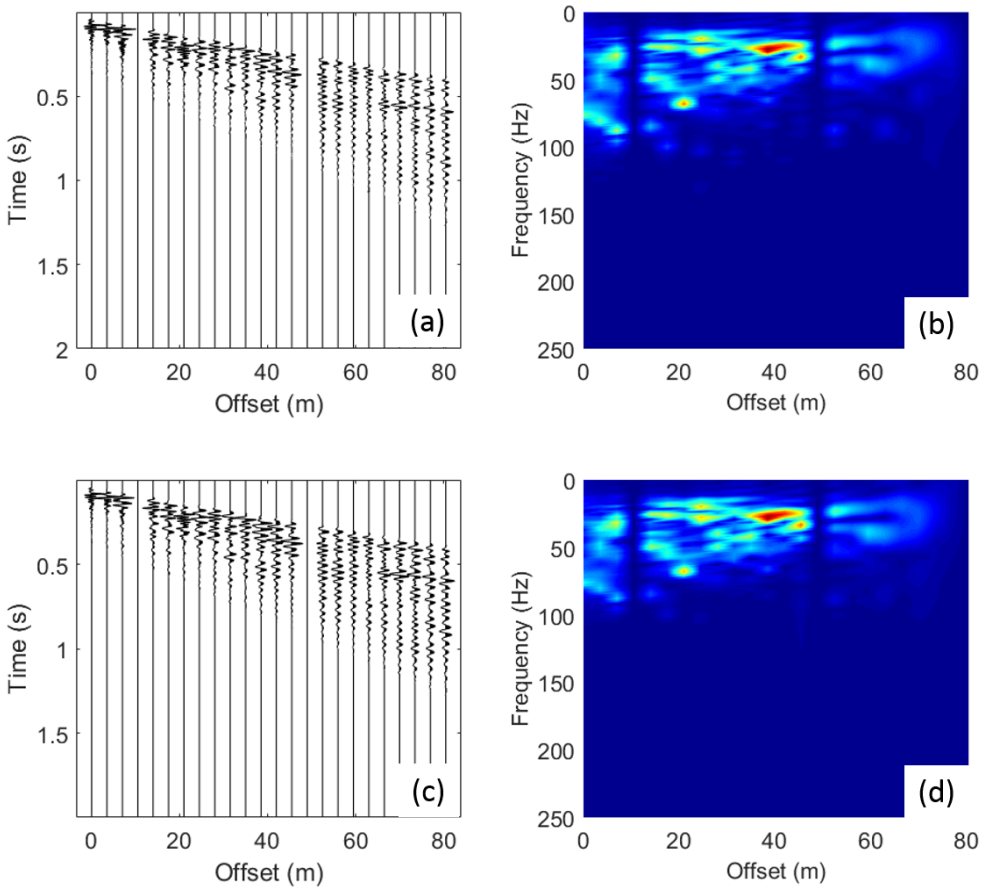

Figure A.31. Line 5 Love wave data comparison before (a) and after (c) applying a low pass filter (0 - 80 Hz). The f-x spectrum before (b) and after (d) applying filter.

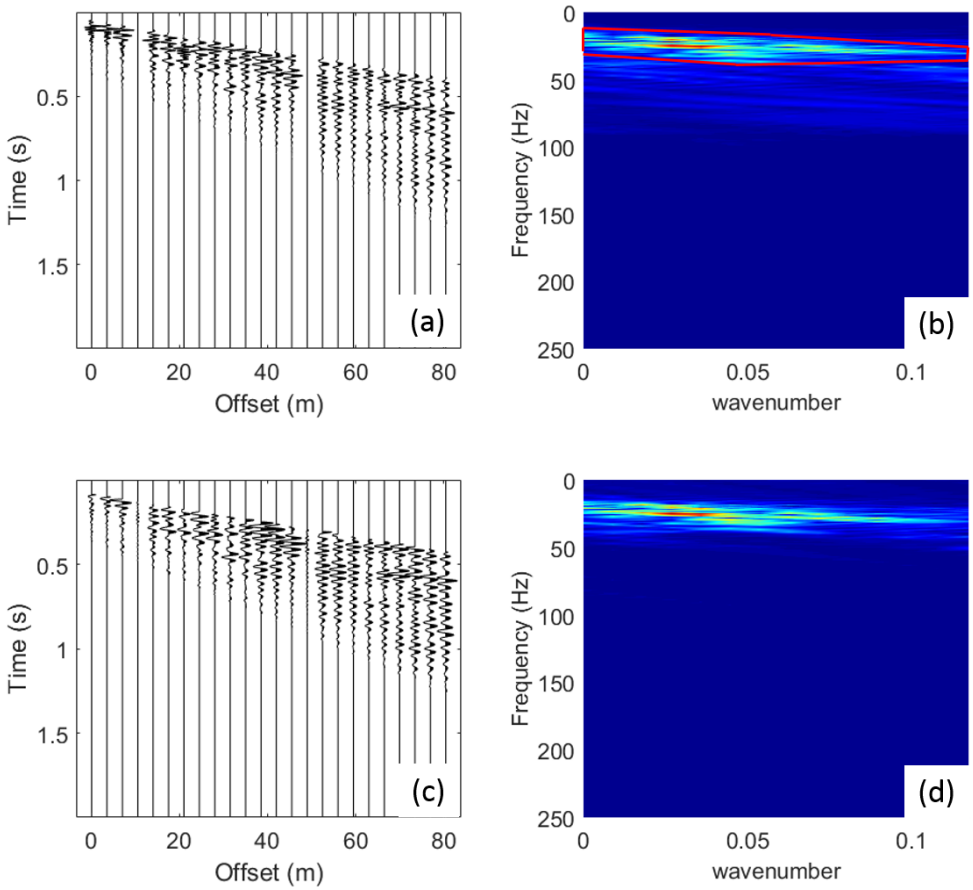

Figure A.32. Line 5 Love wave data comparison before (a) and after (c) applying an f-k filter. The f-k spectrum before (b) and after (d) applying filter. The red polygon in (b) highlights the surface waves within the f-k domain which the f-k filter is designed to preserve.

A.5 Data Processing for Line 6

Data processing for Line 6 followed the flow chart in Table 2 for data processing. In the Rayleigh wave data, windowing was not. For Love wave data, windowing was applied to better identify different modes.

A.5.1 Rayleigh Wave

For the Rayleigh wave data, same processing workflow was followed including stacking (Figure A.33), normalizing the traces (Figure A.34a), muting (Figure A.34b), and low pass and (Figure A.35) and f-k filter (Figure A.36). In Line 6 Rayleigh wave data, fundamental mode, first and second higher mode was obtained (Figure 23).

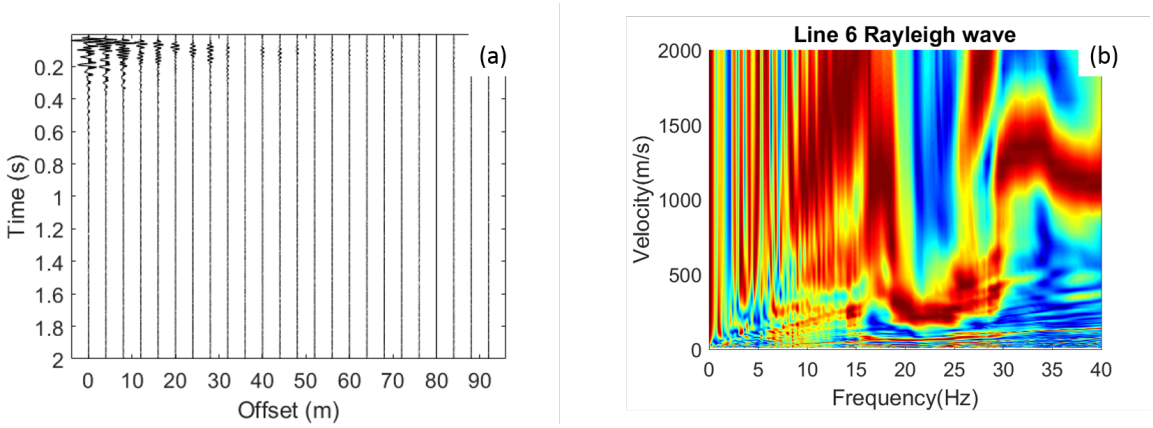

Figure A.33. (a) Line 6 Rayleigh wave seismic record. (b) The phase velocity before any processing.

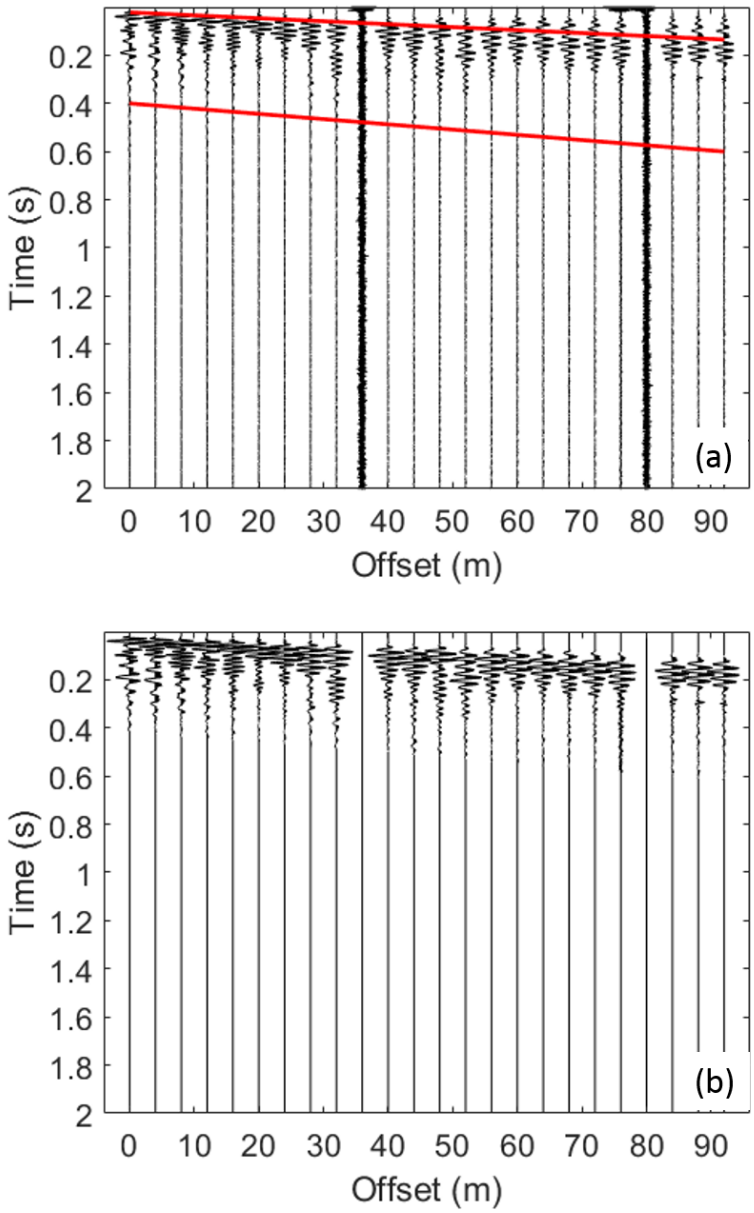

Figure A.34. (a) Line 6 Rayleigh wave normalized seismic trace with top and down muting to preserve the surface wave only. The seismic data was preserved within two red lines. The body waves were muted from the top and the noise from the bottom is also muted. Two noisy traces were removed from this dataset. (b) Line 6 Rayleigh wave data after applied muting.

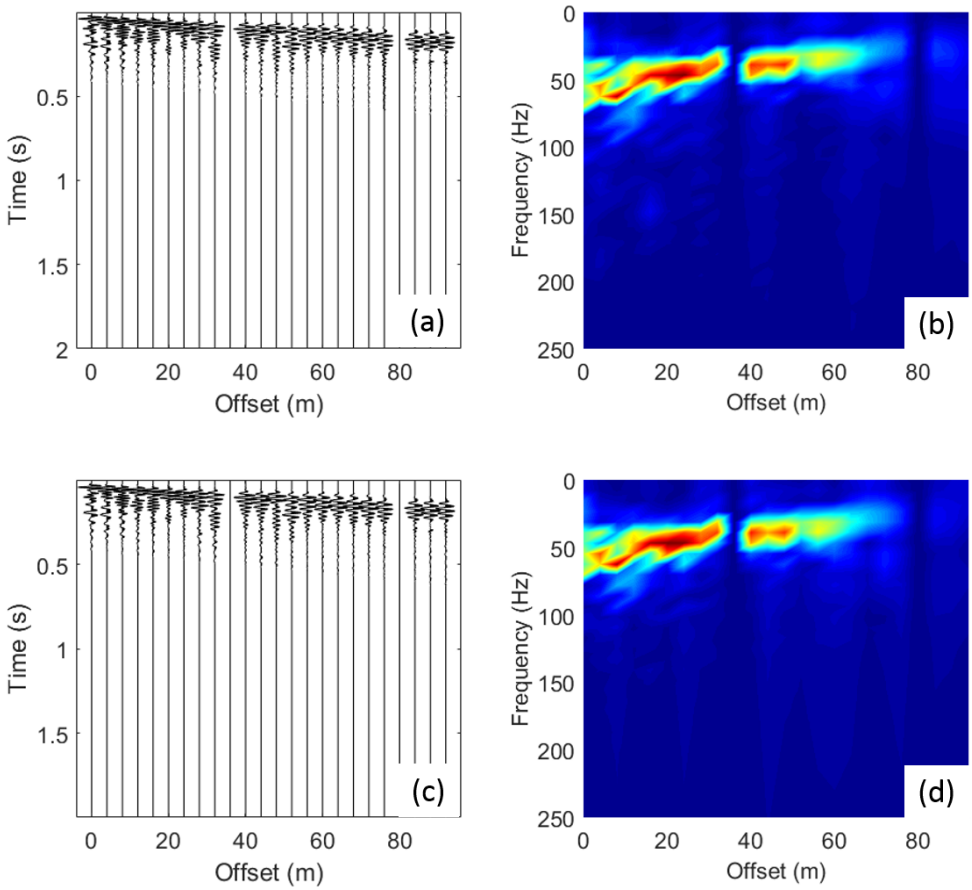

Figure A.35. Comparison before (a) and after (c) applying a low pass filter (0 - 80 Hz). The f-x spectrum before (b) and after (d) applying filter.

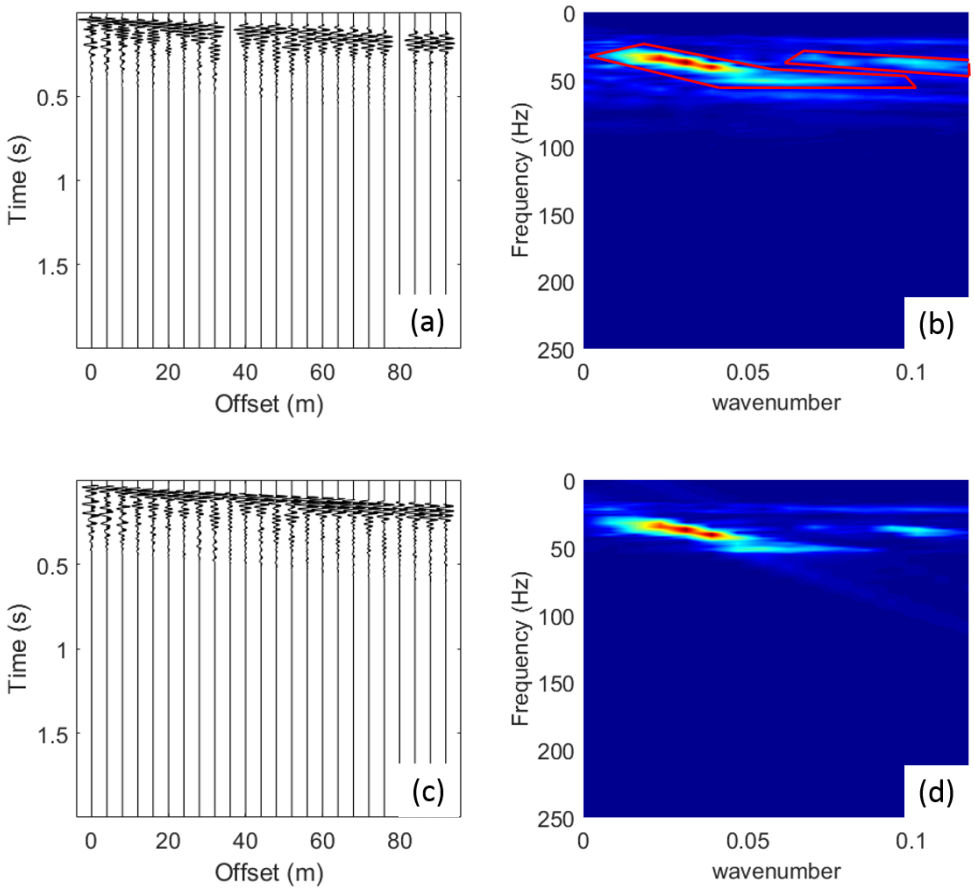

Figure A.36. Line 6 Rayleigh wave data comparison before (a) and after (c) applying an f-k filter. The f-k spectrum before (b) and after (d) applying filter. The red polygon in (b) highlights the surface waves within the f-k domain which the f-k filter is designed to preserve.

A.5.2 Love wave

For the Love wave data, same processing workflow was followed including stacking (Figure A.37), normalizing the traces (Figure A.38a), muting (Figure A.38b), and low pass and (Figure A.39) and f-k filters (Figure A.40). After all the processing step, the

modes are still not distinguishable, different windowing was applied to obtain fundamental mode and first higher mode (Figure 24).

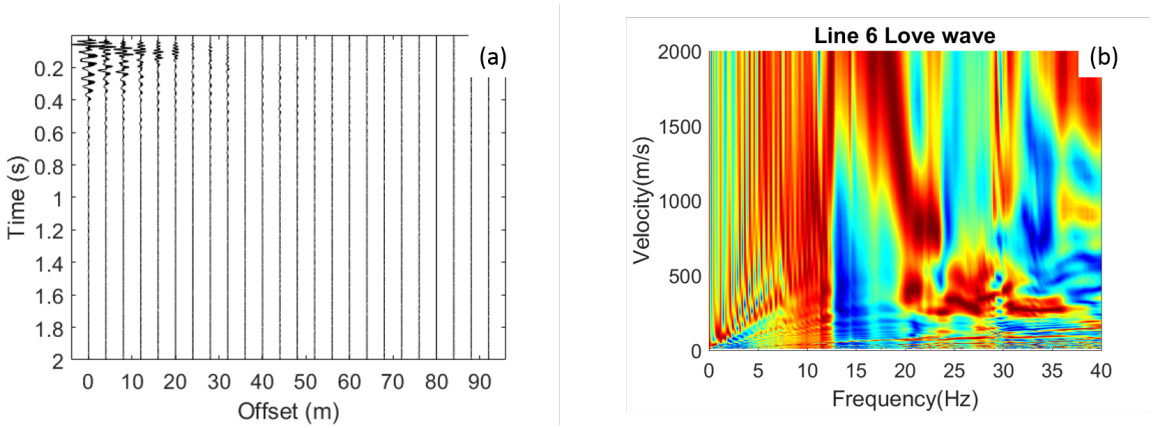

Figure A.37. (a) Line 6 Love wave seismic record and (b) the phase velocity before any processing.

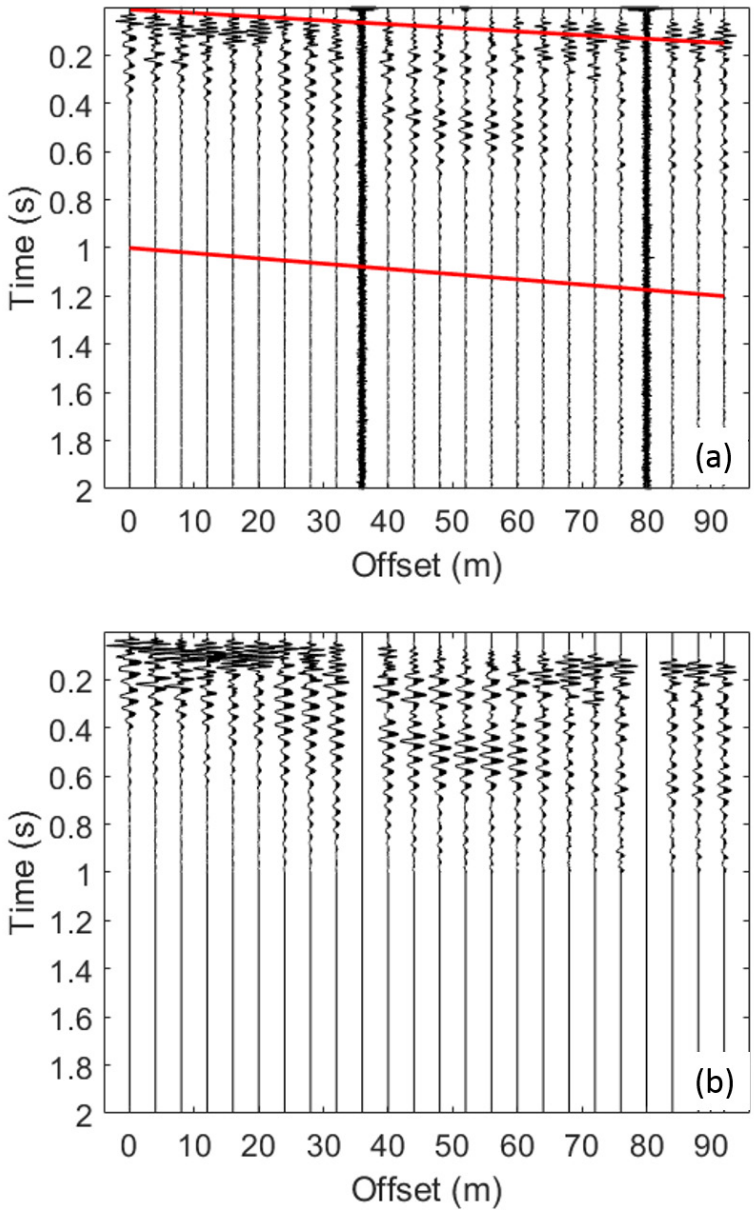

Figure A.38. (a) Line 6 Love wave normalized seismic trace with top and down muting to preserve the surface wave only. The seismic data was preserved within two red lines. The body waves were muted from the top and the noise from the bottom is also muted. Two noisy traces were removed from this dataset. (b) Line 6 Love wave data after applied muting.

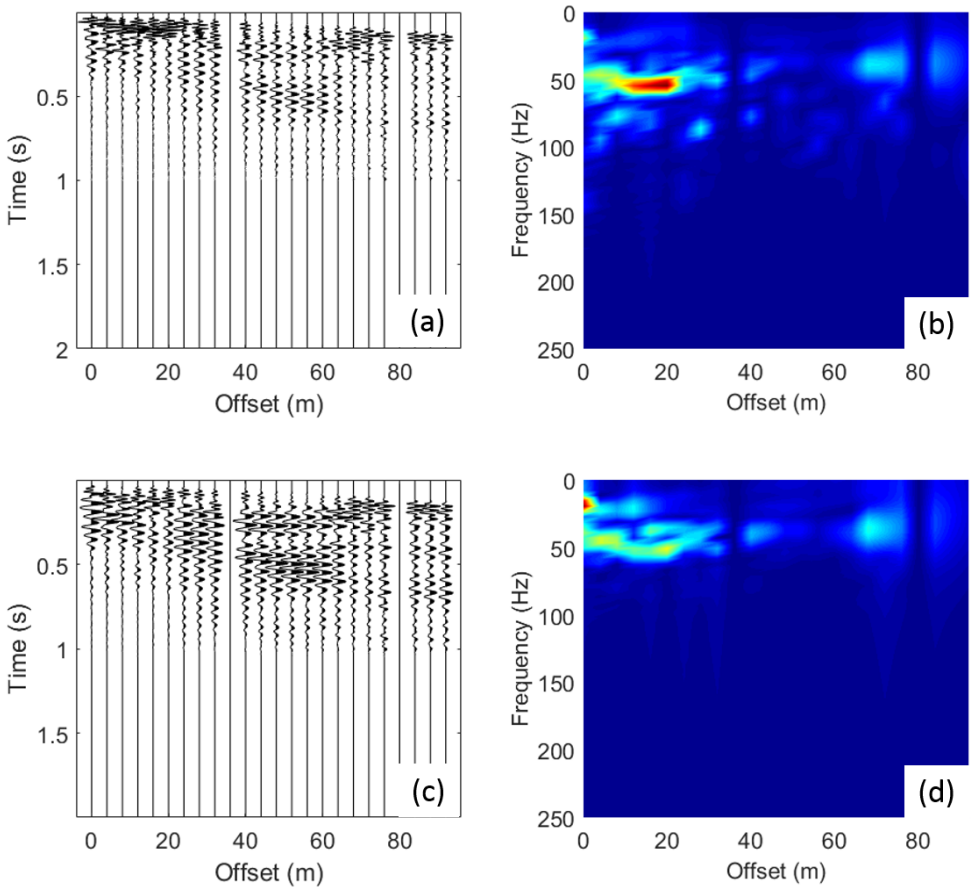

Figure A.39. Line 6 Love wave data comparison before (a) and after (c) applying a low pass filter (0 - 80 Hz). The f-x spectrum before (b) and after (d) applying filter.

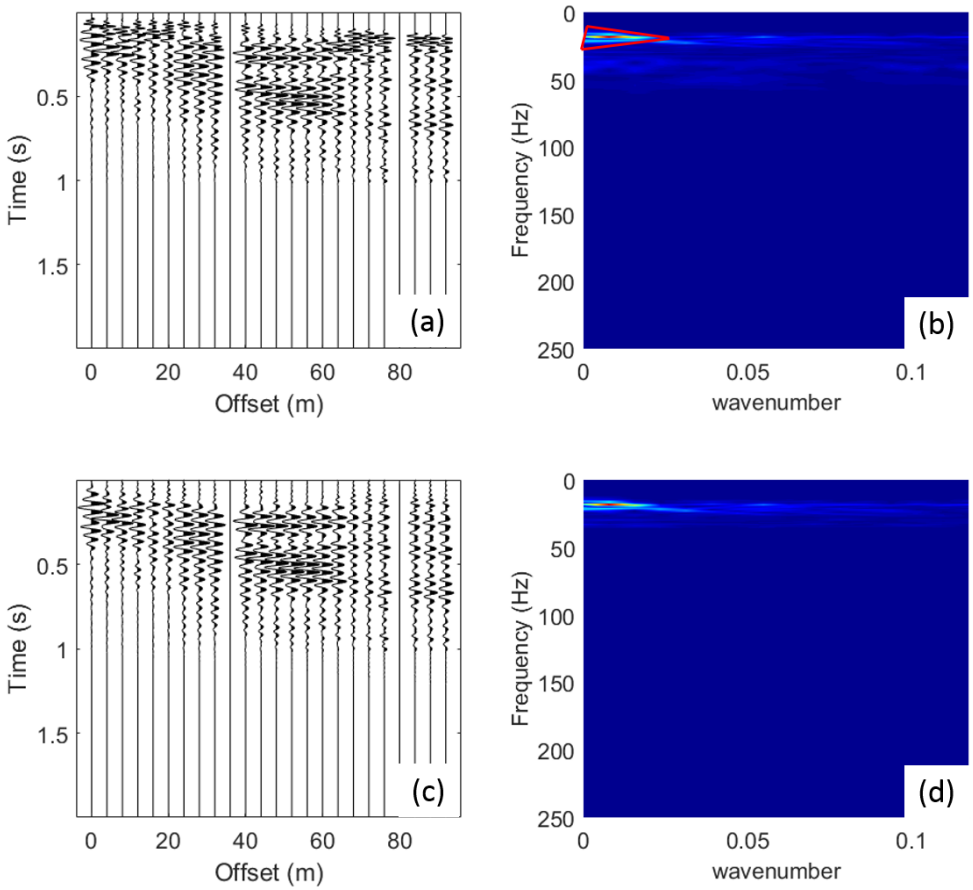

Figure A.40. Line 6 Love wave data comparison before (a) and after (c) applying an f-k filter. The f-k spectrum before (b) and after (d) applying filter. The red polygon in (b) highlights the surface waves within the f-k domain which the f-k filter is designed to preserve.